Computational Fluid-Structure Interaction Study of the Aeroelastic Behavior of a Wire in Transonic and Supersonic Flows

Computationele fluïdum-structuur-interactiestudie van het aero-elastisch gedrag van een draad in transsone en supersone stroming

Akil Osman

Promotoren: prof. dr. ir. J. Vierendeels, prof. dr. ir. J. Degroote
Proefschrift ingediend tot het behalen van de graad van
Doctor in de ingenieurswetenschappen: werktuigkunde-elektrotechniek

UNIVERSITEIT
GENT

Vakgroep Mechanica van Stroming, Warmte en Verbranding
Voorzitter: prof. dr. ir. J. Vierendeels
Faculteit Ingenieurswetenschappen en Architectuur
Academiejaar 2017 - 2018

ISBN 978-94-6355-037-6
NUR 950, 978
Wettelijk depot: D/2017/10.500/72

Supervisors:

Prof. dr. ir. Jan Vierendeels
Prof. dr. ir. Joris Degroote

Research lab:

Department of Flow, Heat and Combustion Mechanics (FloHeaCom)
Ghent University
Sint-Pietersnieuwstraat 41
B-9000 Gent
Belgium

Members of the exam committee:

Chairman:

Prof. dr. ir. Luc Taerwe	Ghent University

Reading committee:

Prof. dr. ir. Gérard Degrez	Université libre de Bruxelles
Prof. dr. ir. Lieva Van Langenhove	Ghent University
dr. Benny Malengier	Ghent University
ir. Jozef Peeters	Picanol N.V.

Other members:

Prof. dr. ir. Jan Vierendeels	Ghent University
Prof. dr. ir. Joris Degroote	Ghent University

Preface

First of all, I would like to thank my supervisors Prof. Jan Vierendeels and Prof. Joris Degroote for giving me the opportunity to do my PhD with them. I am extremely grateful to them for their supports, guidance and valuable discussions from which I have learnt a lot. I would also like to thank the Ghent University for supporting me during my PhD.

I am greatly indebted to my supervisor at the Aleppo University of Syria Prof. Ahmad Almajid who helped and supported me during my PhD. I would like to thank him for everything he has done for me. I want also to thank the Aleppo University from which I had the scholarship to do my PhD and thank them for supporting me financially during my studies in Belgium.

Also thanks to all the colleagues in the fluid mechanics research group. I was fortunate to share the office with Prof. Dieter Fauconnier and Nicholas Agon. They were both ready to help and assist me. Later, I shared the office with Lucas Delcour and Laurent De Moerloose with whom I enjoyed coffee breaks and I would like to thank them for translating the summary of my thesis to Dutch. I want also to thank Alireza Rasekh who I consider a friend. I want to acknowledge his support and friendship and tell him how much they have meant to me. I would also like to thank Iva Papes, Gilberto Santo, Jolan Wauters and Jeroen De Ridder for the nice times during coffee breaks, team activities and conference trips. I want also to thank my colleagues in the other research groups, especially Tarek Beji, Georgios Maragkos, Hugo Monteyne, Alihan Kaya and Marija Lazova. I want also to thank my friends with whom I spent a good time in Belgium.

I would like to acknowledge the help and the support of Yves Maenhout who was always available to solve any software and cluster problems. I would also like to thank the administrative team: Elise Meerburg, Annie Harri and Griet Blondé.

Finally, I would like to express my sincere gratitude and thanks to my parents for everything they have done for me, to my sisters and to my brothers.

Akil Osman
Ghent, September, 2017

Summary

The fluid-structure interaction of a yarn in air flow is studied in this thesis. Fluid-structure interaction is the phenomenon which arises when a fluid flow interacts with a structural motion. The flow generates dynamic forces which deform the structure and in turn the structural deformations influence the flow. Air flow is employed in many textile processes to transport or to excite yarns to move in specific directions. In this thesis, the yarn is represented as a cylinder whose properties are equal to the properties of the yarn. However, the geometrical details of the yarn are neglected. Therefore, the fluid-structure interaction of a cylinder in air flow is studied because the aim of this research is to gain insight into the physics and the numerical simulations of this particular fluid-structure interaction.

Two applications have been studied in this thesis: yarn splicing and weaving. Pneumatic yarn splicing is a technical process for joining two yarn ends together. The process involves injecting compressed air into a splicing chamber. Due to the complexity of the process, fluid-structure interaction simulations of the yarn in this air flow cannot be performed. Therefore, this process is studied and analyzed based on air flow simulations. The goal is to find links between air flow patterns and experimental results. For the second application which belongs to the yarn weaving process, a single yarn is transported by means of air flow. The motion of the weft yarn starts by the main nozzle which sucks the weft yarn from the prewinder and launches it into the reed where the weft yarn speed is kept constant by means of jet flows generated by relay nozzles. The motion of the weft yarn in the main nozzle is modeled and analyzed in this thesis. This motion can be divided into two stages. In the first stage, the weft yarn is clamped and flow is built up in the main nozzle. In the second stage, the yarn is released and accelerated.

To gain insight into numerical simulations of turbulent jet flow, the flow field of a highly underexpanded jet is first considered. The goal is to investigate the ability of the numerical methods to predict correctly this type of flow. Reynolds-Averaged Navier-Stokes (RANS) simulations and large-eddy simulations (LES) have been carried out. The near-field zone of the studied jet flow has been captured by LES and by RANS. The accuracy is deduced by comparing the numerically obtained dimensions of the Mach disk with empirically calculated values. The far-field zone has been evaluated by comparing the obtained total pressure with experimentally measured values. It has been found that if compressibility effects are not taken into account in the turbulence model, the results of the simulations will not be accurate. Although the Smagorinsky-Lilly subgrid-scale model with dynamic constant (the

dynamic model) takes the compressiblity effects into account, the results of LES with either fixed or dynamic model constant have not given accurate results of the total pressure in comparison to the experimental data. Some RANS turbulence models, for example the shear stress transport k-ω model (k-ω SST), are built to take the compressibility effects into account by correction functions. By employing a compressibility correction function in the k-ω SST model with a recommended value of the initial turbulent Mach number, the results of the simulations have improved significantly and good agreement has been found between the simulations and the experiments.

The geometry of the main nozzle in a weaving machine is designed to accelerate the weft yarn axially by means of air flow. The productivity of the weaving machine can be increased by increasing the weft yarn speed. This can be done by optimizing the geometry of the main nozzle to give the highest axial aerodynamic force. An optimization procedure for the geometry of the main nozzle has been proposed. The structure of the main nozzle is described with a set of parameters. Based on the values of these parameters, several point coordinates are calculated and lines or arcs are drawn in between them. The yarn is represented as a smooth cylinder on the axis of the main nozzle moving at fixed and predefined axial speed. Therefore, two-dimensional axisymmetric numerical simulations of the air flow inside the nozzle can be performed. By means of a gradient-based optimization solver, the optimization is carried out targeting the geometry of the nozzle that gives the highest viscous force. Four optimum geometries, related to different constraints, have been obtained and the axial forces of those geometries have improved in comparison to reference values.

The axial flow (with a high velocity) along a flexible cylinder has been proven to generate instabilities. The analytical equations of motion for a cylinder in an axial flow have been derived. By using those equations, the instability of a yarn represented as a cylinder inside the main nozzle has been studied. The effects of different air flow and yarn structure parameters on the instability have been analyzed.

Many effects, for example the effects of shocks, are not included in the analytical equations of motion. Therefore, the fluid-structure interaction simulation of a yarn in air flow is the alternative way to analyze the motion of yarns. Numerical models have been developed and employed to simulate the motion of the weft yarn during the second stage of an insertion on an air jet loom in which the yarn is sucked from the prewinder and launched into the reed. A three-dimensional model of the flexible weft yarn, consisting of a chain of line segments, and a two-dimensional axisymmetric model of the supersonic flow have been developed and coupled to perform these simulations. One-way and two-way fluid-structure interaction simulations of a yarn in air flow inside two different main nozzles of an air jet loom have been carried out. The fluid grid has been fixed in both types of these simulations. In the two-way fluid-structure interaction simulation, the effects of yarn motion on the air flow have been added by a source term. This means that the arbitrary Lagrangian-Eulerian (ALE) technique is not employed in these simulations. The results of the simulations have been compared qualitatively and quantitatively with experimental results.

Subsequently, the motion of a yarn inside a main nozzle during the first stage of an

insertion on an air jet loom in which the weft yarn is clamped has been modeled based on two-way fluid-structure interaction simulations in which the fluid mesh is dynamic. This means that the arbitrary Lagrangian-Eulerian (ALE) technique is employed in these simulations which have been performed by coupling a fluid solver with a structural one. The results of the simulations have been analyzed and compared with videos recorded using a high-speed camera. The main difficulty with this type of simulations is the dynamic mesh. The remeshing method cannot be used because it implies using an unstructured fluid grid which increases significantly the duration of the simulations, particularly in three-dimensional simulations. The amplitudes of the deformation waves in the yarn increase by increasing the inlet pressure, but this distorts the fluid mesh. Moreover, the sharp end of the yarn, represented as a cylinder, increases the complexity of the dynamic mesh.

Samenvatting

De fluïdum-structuur interactie van een garen in een luchtstroming wordt bestudeerd in deze thesis. Fluïdum-structuur interactie (FSI) is een fenomeen dat voorkomt wanneer een vloeistofstroming interageert met een structurele beweging. De stroming veroorzaakt dynamische krachten die de structuur vervormen en deze vervorming beïnvloedt op zijn beurt de stroming. In veel textielprocessen worden luchtstromingen gebruikt om garens te transporteren of aan te zetten tot beweging in een bepaalde richting. Het doel van dit onderzoek is om inzicht te verwerven in de fysica en de numerieke simulatie van deze specifieke fluïdum-structuur interactie. De geometrische details van het garen zijn hierbij van minder belang en worden daarom verwaarloosd. Het garen wordt dus voorgesteld als een cilinder met dezelfde fysische eigenschappen als de draad.

Twee toepassingen werden bestudeerd in deze thesis: wervellassen van garens en weven. Pneumatisch wervellassen is een technisch proces om twee garenuiteinden aan elkaar te hechten. Hiertoe wordt samengedrukte lucht in een wervellaskamer geïnjecteerd, maar door de complexiteit van het proces kunnen hiervoor geen FSI simulaties uitgevoerd worden. Daarom werden verbanden gezocht tussen gesimuleerde stromingspatronen en experimentele resultaten. Voor de tweede toepassing, het weven, wordt een enkel garen getransporteerd door een luchtstroming. De beweging van het garen start met de hoofdblazer die de draad van de voorafwinder zuigt en in het riet lanceert. Daar wordt de garensnelheid constant gehouden door luchtstralen afkomstig van bijblazers. De beweging van de inslagdraad in de hoofdblazer werd gemodelleerd en geanalyseerd in deze thesis. In het algemeen kan dit proces opgedeeld worden in twee stadia. Als eerste wordt de inslagdraad vastgeklemd terwijl de stroming opgebouwd wordt in de hoofdblazer. Daarna, in het tweede stadium, wordt het garen losgelaten en daarop versneld door de stroming.

Om inzicht te verwerven in numerieke simulaties van een turbulente straal werd het stromingsveld van een sterk ondergeëxpandeerde straalpijp bestudeert. Het opzet hiervan is om na te gaan in hoeverre bepaalde numerieke methodes deze stroming correct kunnen voorspellen. Zowel Reynolds gemiddelde Navier-Stokes (Engels: Reynolds-Averaged Navier-Stokes (RANS)) simulaties als Grote-Wervel Simulaties (Engels: Large-Eddy Simulations of LES) werden uitgevoerd. Het stromingsveld dicht bij de straalpijp werd door beide methodes vastgelegd. De nauwkeurigheid hiervan wordt nagegaan door de gesimuleerde Mach-disk afmetingen te vergelijken met analytische berekeningen. Voor de zones ver van de straalpijp werd dit bestudeerd door de berekende totale druk te vergelijken met experimenteel opgemeten

waarden. Er werd vastgesteld dat wanneer de samendrukbaarheid van de lucht niet in rekening werd gebracht, de resultaten weinig nauwkeurig waren. Alhoewel het Smagorinsky-Lilly subgrid-scale model met dynamische coëfficiënten wel rekening houdt met de samendrukbaarheid van lucht, werden er geen nauwkeurige waarden voor de totale druk bekomen met LES (zowel dynamisch als statisch) in vergelijking met experimenten. Sommige RANS turbulentiemodellen, bijvoorbeeld het shear stress transport k-ω model (k-ω SST), zijn ontworpen om samendrukbaarheidseffecten in rekening te brengen door middel van correctie-functies. Door een dergelijke correctie-functie te gebruiken in het k-ω SST model, met een aanbevolen waarde voor het initiële turbulente Mach getal, verbeterden de resultaten significant en werd een goede overeenkomst met de experimenten bekomen.

De geometrie van de hoofdblazer in een weefgetouw is zodanig ontworpen dat de luchtstroom de inslag axiaal versnelt. Door de snelheid van de inslag te verhogen, stijgt de productiviteit van het weefgetouw. Dit wordt bereikt door de vorm van de hoofdblazer te optimaliseren zodat de hoogst mogelijke axiale aerodynamische kracht bereikt wordt. In deze thesis wordt een optimalisatieprocedure voorgesteld. De structuur van de hoofdblazer werd beschreven door een aantal parameters, op basis waarvan punten worden gedefinieerd die nadien verbonden worden met bogen of rechte lijnen. Het garen wordt gemodelleerd als een gladde cilinder gelegen op de as van de hoofdblazer en bewegend aan een vooraf vastgelegde en constante axiale snelheid. In deze tweedimensionale en axisymmetrische geometrie kan de interne luchtstroom gesimuleerd worden. Door gebruik te maken van een gradiëntgebaseerd optimalisatie-algoritme werd de geometrie bekomen die de grootste viskeuze kracht oplevert. Vier optimale parametersets – elk met andere randvoorwaarden – werden voorgesteld. De axiale kracht op het garen in elk van deze geometrieën was hoger dan in de referentievorm.

De axiale luchtstroom rond een cilinder veroorzaakt instabiliteiten. De analytische bewegingsvergelijkingen van de cilinder werden ontwikkeld. Aan de hand van deze vergelijkingen werd de instabiliteit van een garen bestudeerd. De invloed van verschillende parameters, die zowel de luchtstroom als de structuur karakteriseren, werd onderzocht.

Verschillende effecten, bijvoorbeeld het ontstaan van schokken, werden niet opgenomen in de analytische bewegingsvergelijkingen. Om de invloed van schokken op de beweging van het garen te modelleren werd een FSI simulatie gebruikt. Numerieke modellen werden ontwikkeld en aangewend om de beweging van de inslag te simuleren tijdens het tweede deel van de draadinsertie op een weefgetouw waarin het garen van de voorafwinder gewikkeld wordt en in het riet gelanceerd wordt. De FSI berekening omvatten de koppeling van een driedimensionaal model van de flexibele inslagdraad, die voorgesteld werd als een ketting van lijnsegmenten, en een tweedimensionaal, axisymmetrisch model voor de supersone stroming rond de draad. Eénrichting en tweerichting FSI simulaties van het garen werden uitgevoerd in twee verschillende hoofdblazergeometrieën. Het rekenrooster aan vloeistofzijde was in beide gevallen statisch. Het effect van de beweging van de draad op de luchtstroming werd daarentegen gemodelleerd door de invoering van een nieuwe bronterm. Met andere woorden, de arbitraire Lagrangiaans-Euleriaanse (ALE) techniek werd niet toegepast. De resultaten van de simulaties werden nadien op kwalitatieve en

kwantitatieve wijze vergeleken met experimentele data.

Vervolgens werd de beweging van het garen in de hoofdblazer tijdens het eerste deel van de insertie in een weefgetouw gemodelleerd aan de hand van een tweerichting FSI simulatie. Het garen werd gemodelleerd als een cilinder met één ingeklemd uiteinde en één vrij uiteinde. Een dynamisch rekenrooster aan de vloeistofzijde werd gedefinieerd aan de hand van de ALE techniek. De resultaten van de simulaties werden geanalyseerd en vergeleken met beeldmateriaal opgenomen met een hogesnelheidscamera. Het moeilijkste aspect van dergelijke simulaties is de bepaling van het dynamisch rekenrooster. Hiervoor zijn er verschillende redenen. Ten eerste leidt het hermaken van het rekenrooster in iedere tijdstap tot de definitie van ongestructureerde roosters die de simulatietijd significant verhogen, in het bijzonder in driedimensionale simulaties. Ten tweede verwringt het rekenrooster door de golfbeweging van de draad. De amplitude van deze golfbeweging neemt bovendien toe met stijgende inlaatdruk. Ten derde bemoeilijkt het scherpe uiteinde van het garen het gebruik van een dynamisch rekenrooster.

Contents

List of changes

List of Publications

Journal papers

- A. Osman, S. De Meulemeester, B. Malengier, J. Degroote, and J. Vierendeels. Numerical prediction and experimental analysis of ends-together yarn splicing. *Textile Research Journal*. Epub ahead of print 24 June 2016. DOI: 10.1177/0040517516654109
- A. Osman, B. Malengier, S. De Meulemeester, J. Peeters, J. Vierendeels, and J. Degroote. Simulation of air flow-yarn interaction inside the main nozzle of an air jet loom. *Textile Research Journal*. Epub ahead of print 8 March 2017. DOI: 10.1177/0040517517697646

Conference Abstract

- A. Osman, J. Degroote, and J. Vierendeels. Numerical optimisation of the supersonic flow acting on a cylinder in a nozzle. Abstract. *7th European Congress on Computational Methods in Applied Sciences and Engineering (ECCOMAS 2016), Crete Island, Greece*, 2016.

Nomenclature

Abbreviations

ALE	Arbitrary Lagrangian-Eulerian formulation
CFD	Computational Fluid Dynamics
DNS	Direct Numerical Simulation
FSI	Fluid-Structure Interaction
IQN-ILS	Interface Quasi-Newton with an approximation of the Inverse of the Jacobian with a Least-Squares Method
LES	Large-Eddy Simulation
RANS	Reynolds-Averaged Navier-Stokes
RMS	Root Mean Squares
RSS	Retained Splice Strength
SSD	Scale-Selective Discretization

Roman symbols

a	Constant	-
a	Speed of sound	m/s
A	Cross-sectional area	m^2
B	Constant	-
B	Boundary condition equation	-
c	Constant	-
c	Wave speed	m/s
c_v	Specific heat a constant volume	$J/kg.K$
C_b	Base drag coefficient	-
C_s	Smagorinsky constant	-
C_f	Friction coefficient	-
C_{fB}	Forebody drag coefficient	-
$C_{N,T}$	Normal, Tangential force coefficient	-
C_D	Zero-flow normal coefficient	m/s
C_{Dp}	Form drag coefficient	-
dt	Time step	s
D	Diameter	m

D_{MD}	Mach disk diameter	m
D_t	Tube diameter	m
D_h	Hydraulic diameter	m
e	Internal energy	J/kg
E	Total specific energy	J/kg
E	Young's modulus of elasticity	Pa
E	Green-Lagrange strain tensor	-
f	Objective function	-
f	Body forces per unit volume	N/m^3
f	Cylinder free end shape parameter	-
f	Frequency	Hz
F	Force	N
F	Equation of motion	-
$F(M_t)$	Compressibility correction function	-
g	Gravitational acceleration	m/s^2
i	Angle	rad
I	Second area moment	m^4
$Im\,(\omega)$	Imaginary part of eigenvalue	-
K	Thermal conductivity	$W/m.K$
k	Turbulence kinetic energy	m^2/s^2
l	Length	m
L	Length	m
L	Lateral inviscid force per unit length	N/m
L_{MD}	Mach disk location	m
m	Mass	kg
M	Mach number	-
M_t	Turbulent Mach number	-
M	Added mass per unit length	kg/m
n	Normal	-
P	Pressure	Pa
q	Heat flux	W/m^2
q	Generalized coordinate function	-
R	Specific gas constant	$J/kg.K$
R	Arc radius	m
Re	Reynolds number	-
$Re\,(\omega)$	Real part of eigenvalue	-
S	Surface	m^2
S	Source term	N/m^3
S	Strain rate tensor	s^{-1}
S	Sutherland's temperature	K
t	Time	s
T	Temperature	K
u	Velocity	m/s
u	Dimensionless velocity	-
U	Uniform axial velocity	m/s
v	Velocity	m/s
v	Structural deformation	m

V	Volume	m^3
V	Relative velocity	m/s
x_e	Area-weighted averaged length	m
$\overline{x}_e$	Diameter-weighted averaged length	m
x, y, z	x-, y-, z-direction	-
y	Lateral displacement	mm

Greek symbols

α	Angle	rad
β	Mass ratio	-
χ	Confinement factor	-
Δ	Difference	-
δ	Kronecker delta	-
ϵ	Slenderness=L/D	-
ϵ	Dissipation rate	m^2/s^3
γ	Heat capacity ratio	-
μ	Dynamic viscosity	$kg/(ms)$
ν	Poisson ratio	-
λ	Eigenvalue	-
λ	Wave length	m
ρ	Density	kg/m^3
σ	Stress tensor	Pa
τ	Stress tensor	Pa
ϕ	Mode shape function	-
ϕ	Diameter	m
ω	Dimensionless frequency	-

Symbols

d	Derivative
∇	Gradient
∂	Partial derivative
$\|\|\quad\|\|$	Norm
$\|\quad\|$	Absolute value
$\sum$	Summation
$\oiint$	Closed surface integral
$\iiint$	Volume integral

Super- and subscripts

c	Convective

d	Dilatational
D	Diameter
e	Nozzle exit
$exit$	Nozzle exit
f	Fluid
f	Friction
grad	Gradient
i, j, k	In x-, y- and z-direction
k	Coupling iteration
L	In the longitudinal direction
L	Length
N	In the normal direction
p	Pressure
ref	Reference
s	Solid
s	Solenoidal
t	Turbulent
t	Tube
t	Time
´	Fluctuation
o	Initial value
∞	Far away
$\rightarrow$	Vector
x, y and z	In x, y and z direction

Chapter 1

Introduction

1.1 Background

Fluid-structure interaction (FSI) is a multiphysics phenomenon. This phenomenon occurs when a fluid flow interacts with a deformable or movable structure. The flow exerts dynamic forces on the structure. The forces deform or move the structure which in turn influences the flow behavior. The fluid-structure interaction phenomenon may be stable or oscillatory. More precisely, the response of the structure to the fluid flow excitation may be steady (static) or oscillatory (dynamic).

Studying and analyzing a fluid-structure interaction phenomenon is interdisciplinary research in which fluid dynamics and structure dynamics are involved. The first application in which this phenomenon was studied might be a wing of a flight vehicle. In 1899 Orville and Wilbur Wright tested a wing-twist method for roll control [4]. The phenomenon has been called aeroelasticity which has been given great attention in designing a wing of a flight vehicle. Later, this phenomenon has been noticed in many other applications e.g. bridges, rotational machines. Since then, research in the fluid-structure interaction field has started.

Performing a fluid-structure interaction simulation for an application can be done analytically or numerically. The analytical solution involves deriving the equations of motion for the studied case. Hamilton's principle, the Lagrange equation or Newton's second law is employed to obtain the equations of motion which are differential and most likely nonlinear. The disadvantages of the analytical solutions are unfortunately many. The analytical equations are different for each case. The complexity of flow fields and the phenomena associated (e.g. shock waves, compressibility) make deriving the equations of motion very complex, especially in estimating the aerodynamic forces. However, after deriving the equations of motion for a case, obtaining the analytical solution does not need lengthy simulations or strong computing resources.

The numerical solution does not involve deriving new equations. It is rather obtained by coupling the general flow and structure equations in one or different systems of

equations. The advantages of employing the numerical solution to study a fluid-structure interaction case are many. The most important is that the flow field and the resulting aerodynamic force are calculated correctly, to some extent. The main disadvantage of the numerical solution is that it needs high computing resources and time consuming simulations.

The principal objective of this PhD is to study a fluid-structure interaction phenomenon, more precisely aeroelasticity, and to perform analytical and numerical simulations for the interaction of a yarn in air flow. This yarn is a wire which is made of cotton, polyester or nylon and which is used in the textile production field to make, for example, clothes. By definition, aeroelasticity is the phenomenon which occurs when inertial, elastic and aerodynamic forces interact and this is the case for a yarn in air flow. It is possible to perform and to test different types of FSI simulations (one-way, two-way, with static mesh, with moving mesh) with the studied case. Finally, it is possible for the studied case to have experimental data which can be compared with simulation results, which is an important point for any research.

1.2 Interaction between a yarn and the surrounding air flow

Interaction between a yarn and the surrounding air flow is used in the textile industry in many processes, e.g. spinning, splicing or weaving. Air has many advantages which make it convenient in textile production processes. It is clean or it can be easily filtered and its energy can be transformed from one form to another, e.g. compressed air to kinetic energy of an air jet. Due to the viscosity and the pressure effects, the air generates aerodynamic forces when it flows over a yarn. Depending on the magnitude of these forces and on the position of the yarn, those forces excite the yarn to move in a specific direction. However, the main disadvantage of the air flow is that it is difficult to be controlled which leads to some deviations or unexpected behavior of the guided objects like a yarn. Therefore, the FSI simulation of a yarn in air flow is performed to predict the motion of yarns in specific geometries under specific air flow conditions, to optimize a geometry to give the best performance and to evaluate numerically the motion of a yarn in a new geometry. In this work, the interaction between a yarn and the surrounding air flow is analyzed in two applications: yarn splicing and yarn weaving.

Pneumatic yarn splicing is the process in which two yarn ends are joined together. During the operation of production in the textile industries, for example a carpet, this process is used in case of, for example, yarn breaks or the end of the supply package. The process of splicing is done by placing the yarn ends inside a chamber which is called the splicing chamber. The cover of the chamber is then closed and the chamber is supplied with compressed air which generates flow and aerodynamic forces. The generated forces are supposed to splice the yarn ends. Figure 1.1 shows a splicing chamber with yarn ends inside it and the orifice from which the chamber is supplied with compressed air. Two criteria have to be tested to decide if the process of yarn splicing succeeded or not. The first is to check if the two yarn ends are joined together. The second is the strength of the resultant join. Yarn splicing happens

frequently during the creation of textile products. This means that the process of yarn splicing affects the production process because it affects the consecutive steps. A failed yarn splicing process results in stopping the production line. A poor resultant join results in products with flaws.

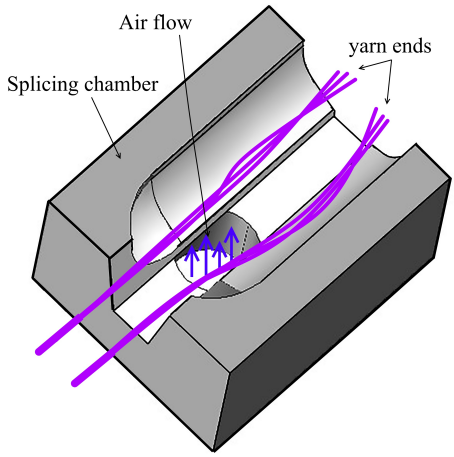

Figure 1.1: A yarn splicing chamber with yarn ends inside it. (ends-together)

There are three factors which affect the yarn splicing: the type and materials of the yarn (monofilament or multifilament yarn, twist, cotton, polyester, ...), the splicing chamber geometry and the air flow inlet condition (inlet pressure value). The complexity of the yarn shape and of the process itself make carrying out FSI simulations of yarn ends in the air flow too difficult. Furthermore, if performing FSI simulations were possible, it would involve deriving a yarn-yarn contact model which is not a goal in this work. Therefore, yarn splicing is studied based on air flow simulation results.

The second application which is studied in this work belongs to the yarn weaving process. The process of yarn weaving is a textile production process in which one or many yarns are interlaced to form a fabric or cloth. Figure 1.2 shows a schematic overview of an air jet weaving machine. Two main devices guide the weft yarn in the weaving machine, namely the main nozzle and the relay nozzles. The motion of the weft yarn starts by the main nozzle. It is supplied with compressed air which expands to high velocity inside it. This air flow generates aerodynamic forces on the weft yarn. The aerodynamic forces suck the weft yarn from the yarn package and launch it into the reed. In the reed, the weft yarn speed is kept constant by means of air jet flows generated by the relay nozzles. When the weft yarn arrives at the end of the reed it is cut by a cutter and it is woven in.

The main nozzle is mainly designed to generate axial aerodynamic forces on the weft yarn. The axial forces accelerate the weft yarn. However, due to the flow field and gravity, the weft yarn moves in the radial direction and it deviates from the axis of the main nozzle. The speed of the weft yarn is important for the speed of the weaving production. The speed of the weft yarn can be increased by increasing the inlet

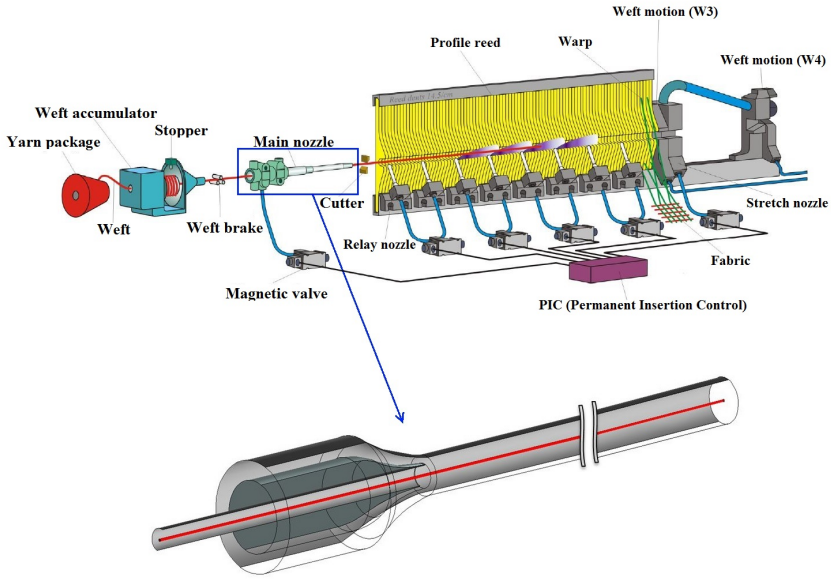

Figure 1.2: A schematic overview of an air jet weaving machine [5] and a close view of the main nozzle.

pressure of the main nozzle, but this increases the energy consumption. Increasing the weft yarn speed can also be done by optimizing the geometry of the main nozzle with specific inlet conditions. However, designing and producing a new main nozzle costs time and money. This cost can be reduced by developing numerical models which are able to predict the motion and the speed of yarns inside main nozzles. The motion of the weft yarn inside the main nozzle can be studied only by performing FSI simulation of a yarn in air flow. Only one yarn is transported by a main nozzle. This means that, with some simplifications of the weft yarn, FSI simulations can be carried out for this case. The motion of the weft yarn inside the main nozzle is a fluid-structure interaction phenomenon and it is the main studied case in this work.

1.3 Research goals

The goal for yarn splicing is to find better splicing chambers and parameters. The effects of the geometry of the splicing chamber and the inlet pressure need to be investigated. The aim is to find links between the results of the air flow simulations and experimental results.

For the second studied application, yarn weaving, the first goal is to optimize the geometry of the main nozzle. The objective is to obtain the highest axial aerodynamic force for a fixed flow rate and pressure. The motion of the yarn needs to be taken into account during the optimization. The second goal is to understand the motion of the weft yarn by performing FSI simulations. There is a need to study the

motion of a yarn during the insertion which is the process of transporting the yarn from the yarn package to the reed. In addition, the deformations of a clamped-free yarn at the beginning of the insertion needs to be understood.

In addition, Païdoussis [6] and [7] derived the equations of motion for a cylindrical object inside a tube. Those equations can be used for a yarn inside a main nozzle by considering the weft yarn as a smooth cylinder. Thus, the analytical solution also has to be calculated.

The motion of the yarn in the reed part is not studied in this work but the air jet flow which discharges from a relay nozzle is studied. There are different shapes of the relay nozzle, with one or multiple exit holes. For a convergent shape of relay nozzle with one exit hole, the associated air jet flow has to be analyzed. The goal is to investigate the ability of the turbulence models to calculate correctly the highly underexpanded air jet flow.

1.4 Outline

Additionally to this introductory chapter, this thesis consists of the following chapters.

The second chapter introduces briefly the governing equations of fluid and structure dynamics, the turbulent flow and the fluid-structure interaction coupling techniques.

The third chapter presents the studied jet flow. This chapter starts with a literature overview of the highly underexpanded jet flow. This is followed by presenting the studied nozzle, numerical simulation setup and the employed turbulence models. The results of the simulations are then presented and compared with experimental data. The compressibility effects on the turbulence model are discussed and the results with and without compressibility corrections are presented.

In the fourth chapter, the yarn splicing process is studied and analyzed based on large-eddy simulation of the air flow which has been performed in four chambers. The effects of the inlet pressure and the geometry of the chambers are investigated. The results of the simulations are linked to experimental results and the flow field characteristics which improve the splicing process are discussed. This chapter is based on [8].

In the fifth chapter, the optimization procedure and setup of the main nozzle geometry are presented and explained followed by the results of four obtained optimal geometries. Two of them are related to the diameter of the yarn and the other two are related to a property of the geometry of the main nozzle which is called the threading property. This property is required when a weaving machine is not working to insert the weft yarn in the main nozzle.

In the sixth chapter, the instability of a yarn, represented as a cylinder, is analyzed based on the analytical equations of motion and the effects of different parameters on the instability are also investigated and presented.

The seventh chapter presents the fluid-structure interaction simulations of a yarn in air flow with fixed mesh. In this type of FSI simulations, the motion of a yarn which is moving axially and radially is modeled. Therefore, the motion of the weft yarn during one insertion is analyzed. An overview of the previous works is first presented. Then, the fluid and the structure models are presented. In the fluid solver, the aerodynamic forces are calculated and given to the structure solver which calculates the other forces to which the weft yarn is subjected and, eventually, the new positions of the weft yarn are obtained and given back to the fluid model. The fluid grid is fixed and the effects of the weft yarn motion on the flow is taken into account by a source term. The results of one-way and two-way FSI simulations are then presented and compared with experimental data and high-speed videos of experiments. This chapter is based on [9].

In the eighth chapter, two-way fluid-structure interaction simulations of a yarn in air flow with dynamic mesh are presented. These simulations model the deformations of a clamped-free yarn inside a main nozzle. Before starting each insertion of the weft yarn, the pressure inside the main nozzle is built up and the weft yarn is clamped. In this type of FSI simulations, the fluid-structure interface in the fluid domain is displaced according to the new position of the structure. This chapter starts with introducing the studied case followed by the experimental conditions and setup. Then, the results of the simulations are presented and compared to experiments.

In the last chapter, the overall conclusion and some recommendations for future work are presented.

Chapter 2

Theoretical introduction

2.1 Flow equations

The flow of a compressible fluid is governed by three equations which are the continuity equation (2.1), the momentum or Navier-Stokes equations (2.2) and the energy equation (2.3). Deriving these equations is based on the law of conservation of mass and energy and Newton's second law.

$$\frac{\partial \rho_f}{\partial t} + \frac{\partial \rho_f u_j}{\partial x_j} = 0, \tag{2.1}$$

$$\frac{\partial \rho_f u_i}{\partial t} + \frac{\partial \rho_f u_i u_j}{\partial x_j} = -\frac{\partial p}{\partial x_i} + \frac{\partial \sigma_{f,ij}}{\partial x_j}, \tag{2.2}$$

$$\frac{\partial \rho_f E}{\partial t} + \frac{\partial \left(\rho_f E + p\right) u_j}{\partial x_j} + \frac{\partial q_j}{\partial x_j} = \frac{\partial \sigma_{f,ij} u_i}{\partial x_j}. \tag{2.3}$$

In the above equations t is the time and x_i spatial coordinates of a Cartesian coordinate system x. ρ_f is the density of the fluid. The three components of the velocity vector **u** are denoted u_i (i=1,2,3) and the Einstein summation convention is used. p is the pressure and σ_f the viscous stress tensor which is for a Newtonian fluid equal to

$$\sigma_{f,ij} = 2\mu_f S_{f,ij} - \frac{2}{3}\mu_f \delta_{ij} S_{f,kk}, \tag{2.4}$$

with μ_f is the dynamic viscosity of the fluid and δ_{ij} the Kronecker delta. $S_{f,ij}$ is the rate of strain tensor which is given by

$$S_{f,ij} = \frac{1}{2}\left(\frac{\partial u_i}{\partial x_j} + \frac{\partial u_j}{\partial x_i}\right). \tag{2.5}$$

E is total specific energy of the fluid which is the sum of the internal and kinetic energy $E = e + u_i u_i/2$. q is the heat flux given by $q = -K\nabla T$ with *T* the static temperature and *K* the thermal conductivity.

The continuity and energy equation are scalar equations while the momentum equation is a vector equation. For a perfect gas, the equation of state which links the pressure, the density and the temperature together is $p = \rho_f RT$ with R the specific gas constant. For a calorically perfect gas, the internal energy can be expressed as $e = c_v T$ with c_v the specific heat at constant volume.

The flow equations are nonlinear partial differential equations. Solving these equations cannot be done analytically in general. Therefore, the flow domain is divided into small volumes, finite volumes, and Equations (2.1), (2.2) and (2.3) are discretized and applied to each volume. The most common method which is used to discretize the flow equations is the finite volume method (see Versteeg and Malalasekera [10]). Computational Fluid Dynamics (CFD) is the field of applied science which studies fluid dynamics by solving numerically the governing equations.

2.2 Turbulence

The most challenging phenomenon encountered in CFD is the turbulence. Flows encountered in engineering applications or in nature are laminar, turbulent or transitional. In 1937, Taylor and von Kármán (see [1]) suggested the following definition of turbulence: "Turbulence is an irregular motion which in general makes its appearance in fluids, gaseous or liquid, when they flow past solid surfaces or even when neighboring streams of the same fluid flow past or over one another." By contrast, a laminar flow occurs when a fluid flows in smooth layers. The Reynolds number is a dimensionless number which is equal to inertial forces over the viscous forces and it is mathematically given by

$$Re = \frac{UL\rho_f}{\mu_f}, \tag{2.6}$$

where U and L are the characteristic velocity and length. The value of the Reynolds number is commonly used to predict if a flow is laminar or turbulent, but that value is different from an application to another. For example, the flow inside a pipe is laminar for *Re < 2000*, while the wake of the flow around a cylinder is turbulent for *Re > 260*.

The Reynolds decomposition is employed to model a turbulent flow. This decomposition is based on dividing flow quantities into two parts: a mean value and a fluctuating value, namely $u = U + \acute{u}$ with U the mean value and $\acute{u}$ the fluctuating one. The challenge in CFD is to calculate correctly the mean values of the flow quantities and to estimate the influence of the fluctuating ones on the mean flow.

Three simulation types are used in CFD to calculate turbulent fluid flows [11]: the direct numerical simulation (DNS), the large-eddy-simulation (LES) and the Reynolds-averaged Navier-Stokes (RANS) simulation. In DNS, the mean and the fluctuating components of the flow quantities are calculated directly without modeling. The

DNS method is not applicable especially for engineering applications due to high cost and duration of the simulations. The LES method gives less accurate results than DNS but at a lower cost. In LES, the large eddies are calculated and the small ones are modeled. The separation between the large and the small eddies is done by a spatial filter which is typically defined by the mesh. Thus, the LES depends on the mesh. Although the cost of LES is lower than that of DNS, it is still high, thus the RANS method is applicable to give relatively less accurate results in less time than LES and DNS. The idea of the RANS method is to calculate the mean values of the flow quantities while taking into account the effects of the fluctuating ones. The RANS method does not depend on the mesh like LES, it depends only on physical quantities.

After ensemble time averaging, which is used with the RANS method, or space filtering, which is used with LES method, of the flow equations, new unknown terms arise in the Navier-Stokes equations. The new terms are called the Reynolds stresses. Modeling the turbulence in CFD involves estimating the values of the Reynolds stresses or mathematically adding new equations to close the system of the flow equations. In the RANS method, the Reynolds stresses are estimated or modeled by what is called the turbulence model, for example the Spalart-Allmaras one-equation turbulence model [12] or two-equation models like the shear stress transport (SST) k-ω model [13]. In LES, the Reynolds stresses are calculated based on a subgrid-scale model, for example by Smagorinsky [14].

2.3 Structure equations

Material deformations or displacements are calculated using the law of conservation of momentum. Considering a body with mass m_s subject to a traction and body force, the momentum equation for that body can be obtained by applying Newton's second law,

$$\rho_s \frac{\partial^2 v_i}{\partial t^2} - \frac{\partial \sigma_{s,ij}}{\partial x_j} = f_{s,i}, \tag{2.7}$$

where ρ_s is the density of the structure, v the position of the structure and f_s the body forces per unit volume. For structural analysis the stress tensor is described in relation to the deformation gradient. Thus, the Cauchy stress tensor $\sigma_{s,ij}$ is related to the Green-Lagrange strain tensor $E_{s,ij}$ by the constitutive equation of the material. The Green-Lagrange strain tensor is equal to

$$E_{s,ij} = \frac{1}{2}\left[\frac{\partial v_i}{\partial x_j} + \frac{\partial v_j}{\partial x_i} + \frac{\partial v_k}{\partial x_j}\frac{\partial v_k}{\partial x_i}\right]. \tag{2.8}$$

For small deformations, the part $\frac{\partial v_k}{\partial x_j}\frac{\partial v_k}{\partial x_i}$ in Equation (2.8) is small and can be neglected.

The finite element method is commonly used to discretize structure equations. Moreover, the Lagrangian framework is employed to model structure dynamics because

the goal is to calculate the displacements or the velocity of the structure and, in this case, the spatial structure points are moving in time.

2.4 Yarn structure

The structure of a yarn depends on the properties of the fibers used in the yarn. Yarns made of many filament fibers are known as multifilament yarns, while yarns produced from one single filament fiber are monofilament yarns. Moreover, spun yarns are produced by twisting together short fibers, for example cotton yarns. Therefore, the type of a yarn determines the appearance and the mechanical properties of the yarn. Modeling the structure of a yarn is complex, but it can be simplified. For example, a yarn can be represented as a cylinder whose properties are equal to the properties of the yarn. Those properties are: diameter, Young's modulus, aerodynamic force coefficients, or other properties. The effects of the yarn hairiness can be included in the aerodynamic force coefficients. The effects of a yarn being monofilament or multifilament can be included in the Young's modulus. When the yarn is immersed in an air flow, it is subjected to different types of forces: aerodynamic forces which can be considered as external forces and which are due to pressure and viscous effects; gravity which is a body force; tensile forces which are internal forces; external contact forces e.g. contact with the surrounding surfaces and internal contact forces between filaments. Moreover, the effects of bending and twisting which are resulting motions should be taken into account. Twisting can be a result of axial forces and the anisotropic nature of the yarn e.g. being made of twisted filaments. Twisting can also be due to a twisting moment. However, the complexity of the yarn structure is not considered in this work and all properties of the studied yarns are measured experimentally and considered to be uniform along the yarn, e.g. diameter.

2.5 FSI technique and coupling conditions

Fluid-structure interaction simulation involves coupling the flow equations and the structure equations. Two approaches exist to couple the governing equations: the monolithic and the partitioned approach. In the monolithic approach, the flow and the structure equations are solved in one system. This means that the interaction between the flow and the structure is directly taken into account. By contrast, in the partitioned approach, the flow and the structure equations are solved separately. This involves that a coupling code has to be used with the partitioned approach to couple the flow and the structure equations.

The coupling equilibrium conditions on the fluid-structure interface are the kinematic condition

$$\overrightarrow{u} = \frac{d\overrightarrow{v}}{dt}, \tag{2.9}$$

and the dynamic condition

$$\overline{\sigma}_f . \overrightarrow{n}_f = -\overline{\sigma}_s . \overrightarrow{n}_s, \tag{2.10}$$

where the flow stress $\overline{\sigma}_f$ is the sum of the viscous and pressure stresses. $\overrightarrow{n}_{f,s}$ is the unit normal vector pointing outwards the fluid or structure domain. The kinematic condition implies a no-slip condition for the flow on the interface.

A coupling algorithm with Dirichlet-Neumann decomposition generally works as follows. The flow equations are first solved based on the given position of the structure. Then, the new position of the structure is calculated based on the new forces due to the flow field. These two steps are iterated in each time step until the equilibrium conditions are satisfied up to a convergence tolerance.

A partitioned code is employed in this work to perform the FSI simulation which is called Tango. Tango has been developing at the Department of Flow, Heat and combustion mechanics at Ghent University [15]. This code couples Fluent as the flow solver with Abaqus as the structure solver.

Chapter 3

Numerical simulations of a highly underexpanded jet flow

In this chapter, the flow which is issuing from a circular nozzle will be analyzed. This type of flow is commonly known as jet flow or free shear (layer) flow. The studied nozzle is used as a relay nozzle in a weaving machine. The results of the numerical simulations will be compared with experimental data.

This chapter starts with an introduction and literature overview of the jet flow. In the subsequent sections, the numerical simulation and the employed turbulence models are presented. Then, the numerical results are presented and compared to experimental data of the total pressure measured by a Pitot tube.

3.1 Literature overview on jet flow

3.1.1 Introduction

Jet flow is a well known type of flow in CFD because it is commonly used in engineering applications. Jet flow occurs when a gas discharges from an orifice to another quiescent fluid. The jet flow may occur internally in a bounded domain [16] but the name *jet flow* refers commonly to the flow which discharges into an unbounded domain and it can be classified as a free shear (layer) flow. The jet flow has a high kinetic energy which can be used to generate thrust as in a jet engine or rocket. Moreover, the jet flow can generate high aerodynamic forces if it flows over an object. The generated aerodynamic forces can be used to do a specific work, for example to accelerate a yarn in an air jet weaving machine.

According to the pressure at the exit of the nozzle two cases of jet flow exist which are the overexpanded and underexpanded case. If the exit pressure is less than the

ambient pressure, the flow is overexpanded. It adapts to the ambient conditions via a system of oblique shock and expansion waves. By contrast, if the exit pressure is higher than the ambient pressure, the flow is underexpanded. It expands to the ambient pressure via expansion and shock waves. In both cases, the flow field has a complex pattern due to the presence of shocks, expansion and compression waves which interact with each other, recirculation and mixing shear layers. Moreover, the underexpanded jet flow can be divided into two types as reported in Vuorinen et al. [17]: the moderately and the highly underexpanded jet flow. The moderately underexpanded jet flow, Figure 3.1(a), occurs when $1.1 < p_{exit}/p_{ambient} \leq 2$ and the highly underexpanded jet , Figure 3.1(b), flow occurs when $2 < p_{exit}/p_{ambient}$. At $p_{exit}/p_{ambient} = 2$, a normal shock is generated downstream of the nozzle exit, while only oblique shocks occur for lower pressure ratios. The highly underexpanded jet flow is the type of the flow studied in this chapter.

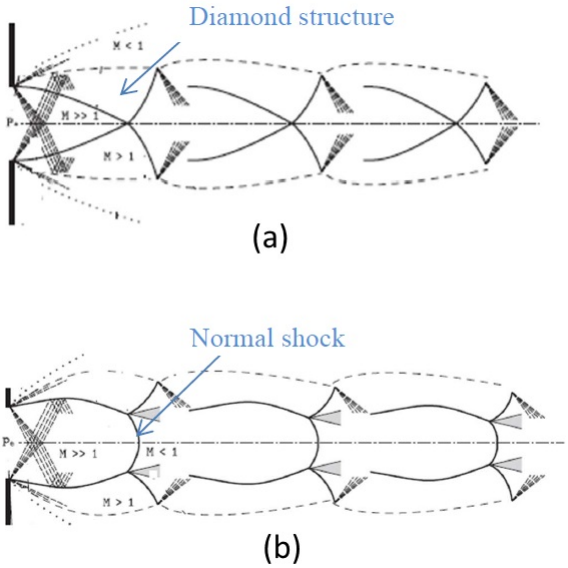

Figure 3.1: Structure of a jet, taken from [2]: (a) Moderately underexpanded jet; (b) Highly underexpanded jet.

3.1.2 Highly underexpanded jet flow

Figure 3.2 shows the schematic view of the near-field of a highly underexpanded jet flow. At the exit of the nozzle, the sonic line forms as the nozzle is choked. Then, the flow expands to a supersonic velocity. Due to the high pressure difference between the upcoming flow and the ambient one, a normal shock occurs in a Mach disk. The flow after the normal shock is subsonic forming what is called a shock cell. Afterwards, series of expansion and compression waves take place until the flow becomes fully subsonic and dissipates completely into the ambient fluid.

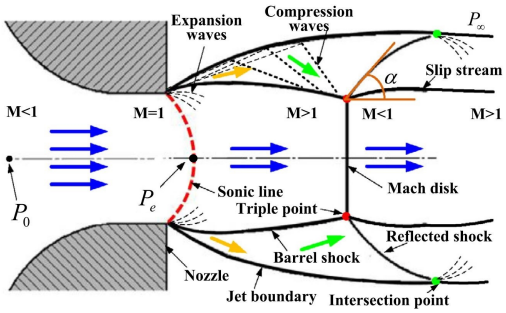

Figure 3.2: General pattern of the near-field of a highly underexpanded jet flow, taken from [18].

The jet flow has been analyzed and investigated widely numerically and experimentally. However, the highly underexpanded type has not yet been fully understood [2].

I. Experimental investigation

Eggers [19] performed an experimental study of a jet flow with Mach number equal to 2.22. He measured the total pressure from the nozzle exit to 150 nozzle radii downstream. He attempted to extract values of eddy viscosity from the experiments by using analytical formula but this did not give accurate results. Dimotakis et al. [20] studied the dynamics of turbulent jets with various Reynolds numbers. They noticed that in the far-field region of the jet flow large-scale vortical structures were dominant. Law and Herlina [21] carried out experiments to study the jet flow up to 50 nozzle diameters. They showed the mean velocity profiles along the jet centerline based on measurements and curve fitting for three different Reynolds numbers. Inman et al. [22] conducted a series of experiments to investigate the behavior of underexpanded jet flows, particularly the transition to turbulence in free jet flows. They used planar laser-induced fluorescence (PLIF) to visualize the jet flows. They found that the transition from laminar to turbulent flow was affected by the Reynolds number and by the pressure ratio. Moreover, if the Mach disk occurred, which means the jet flow was highly underexpanded, the triple point (see Figure 3.2) was a source of instabilities. Tsai et al. [23] studied the effect of the external turbulence properties on the jet flow. They found that the external turbulence affected significantly the jet shear layer.

Experimental investigations of jet flow were previously the only possibility to understand and study it. Nowadays, CFD tools have been developed to investigate jet flow but, of course, experiments are still used to validate the accuracy of the numerical tools.

II. Numerical investigation

The numerical investigation of jet flow, particularly the highly underexpanded jet flow has been an interesting topic for research and this topic continues to attract attention. Although numerous works have already been done to study jet flow numerically, research is still continuing to develop the turbulence models to predict it correctly. For example, Boersma and Lele [24] utilized large-eddy simulation to simulate jet flows. They used a velocity profile as inlet condition. They compared their LES results with previous DNS and experimental results. They found that the differences between LES and DNS increased by increasing the jet flow velocity. Dimotakis [25] studied the mixing transition in jet flows. He reported that the transition in the jet flow to fully turbulent flow occurred at $Re \geq 10^4$. Munday et al. [26] analyzed a jet flow structure of a convergent-divergent nozzle by employing large-eddy simulation. They showed the pattern of the shock cell and the Mach disk which were obtained from the simulations. Bayeh [27] calculated theoretically the air flow properties through the Mach disk of an underexpanded jet flow by the method of characteristics and he compared the results with experimental ones. However, he did not report the calculated results. Aziz et al. [28] and Heschl et al. [29] reported that the k-ϵ model could not predict accurately the turbulent kinetic energy with a jet flow. Karabasov et al. [30] and Faranosov et al. [31] found that LES did not give accurate results in comparison to experimental data which were the centerline axial velocity and the turbulence kinetic energy of a jet flow. Velikorodny and Kudriakov [32], Li et al. [33] and Hamzehloo and Aleiferis [34] analyzed the near-field of a highly underexpanded turbulent gas jet. They compared their results with experimental data. They found good agreement between their results and experiments in the near-field region but not that good agreement in the far-field region.

One important conclusion can be drawn from the previous works. For a highly underexpanded jet flow, the numerical methods and the turbulence models still have to be developed further. The near-field of the highly underexpanded jet flow can be captured correctly numerically but the far-field not always. Relatively recent work conducted by Vuorinen et al. [35] proposed a new procedure to improve the accuracy of the numerical results with large-eddy simulation. They derived a low-dissipative scheme for the convection term in Navier-Stokes equations. That scheme is called the scale-selective discretization (SSD) scheme. Their aim was to reduce the numerical dissipation associated with the existing schemes. The SSD scheme is based on decomposing the velocity into two parts, namely the smooth part $u_i - u_i'$ and the non-smooth part u_i'. They applied this assumption just for the convection term. The resultant smooth and non-smooth convection terms have to be discretized with two different schemes. Later Vuorinen et al. [17] and Yu et al. [18] tested the SSD scheme with highly underexpanded jet flows. They carried out simulations and experiments with different inlet pressures. They investigated deeply the flow pattern and the characteristics of the studied highly underexpanded jet flows. They showed good agreement between the LES results and planar laser-induced fluorescence images in the near-field region of the jet.

The difficulties with modeling the highly underexpanded jet flow are due to the associated instability in the shear layer, called the Kelvin-Helmholtz instability or

the shear layer instability. A schematic drawing of the general pattern of a highly underexpaned jet flow is shown in Figure 3.3.

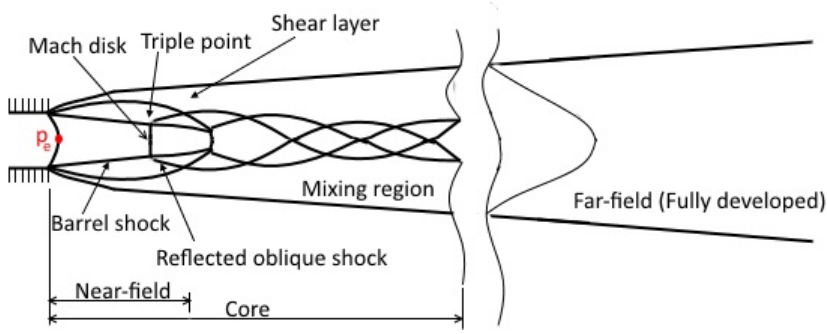

Figure 3.3: Schematic drawing of the general pattern of a highly underexpaned jet flow.

3.1.3 Free shear layer (mixing layer)

The shear layer forms between the jet flow and the quiescent ambient fluid. The shear layer starts to develop from the slip line across which the static pressure is the same but the velocity changes sharply. Due to the effects of vorticity, the shear layers roll up and vortices separate traveling downstream. The resultant vortices mix with the other scales. Eventually, the mixing region develops to a fully turbulent region and dissipates. This instability belongs to the Kelvin-Helmhotltz instability or the shear layer instability which occurs when two fluids flow parallel to each other [36, 37]. This instability is always associated with the jet flow but the roll-up and the separation of the vortices are not seen except at low Reynolds number [38, 39]. By increasing the Reynolds number, the instability occurs early at short distance from the nozzle exit and vortices form and separate fast. However, the vortices can be clearly seen if the jet flow interacts with another stream or flow which is moving [40].

Davey and Roshko [41] analyzed the effects of the density differences on the instability of the shear layer. They found that the density differences had great effects on the transition and the mixing in the shear layer. If the flow is supersonic, the effects of the compressibility are dominant as reported in Brown and Roshko [42]. Density effects and compressibility effects are similar and both are linked to changes in density, but with different causes. Density effects occur with low speed flows in which the density changes in response to temperature changes or due to a difference in fluid. By contrast, the compressibility effects occur with supersonic flows in which the pressure changes contribute to the density changes. Therefore, with highly underexpanded jet flows, compressiblity effects is the most appropriate terminology.

3.1.4 Compressibility effects

The compressibility plays a crucial role in a supersonic turbulent jet flow [43]. To evaluate this role, research was first based on experiments to understand the physics and to derive mathematical relations to include compressibility effects in numerical simulations. Bogdonoff [44] and Papamoschou and Roshko [43] introduced a non-dimensional parameter which is called the convective Mach number M_c to quantify the level of the compressibility in the shear layer. Inside the shear layer, the convective velocity is the one at which the large scales propagate downstream. For two pressure-matched parallel streams with equal specific heat ratios, the convective Mach number is given as

$$M_c = \frac{u_1 - u_2}{a_1 + a_2}, \tag{3.1}$$

where u_1 and u_2 are the velocities of the high- and low-speed free stream respectively, and a_1 and a_2 are the speeds of sound in these streams.

Papamoschou and Roshko [43] conducted experiments to study the effects of the compressibility on the shear layer formed between two turbulent flows. They reported that the growth rate of the shear layer decreased with increasing convective Mach number. The effects of the compressibility increase by increasing the flow velocity or Mach number [42].

It has been found that the compressibility has dissipative effects on the turbulence [3, 45]. Blaisdell and Zeman [3] reported that the reduction in growth rate of the turbulent kinetic energy is due to the dilatational dissipation rate and the pressure-dilatation correlation. The former term is due to the divergence of the velocity, while the latter term is due to the fluctuating transfer of energy (e.g internal to kinetic). The total dissipation rate is expressed as

$$\varepsilon = \varepsilon_s + \varepsilon_d = \varepsilon_s \left(1 + \varepsilon_d/\varepsilon_s\right), \tag{3.2}$$

where ε_s is the solenoidal dissipation rate which is the same as for an incompressible flow and ε_d is the dilatational dissipation rate. The compressibility effects are taken into account by considering the term $\varepsilon_d/\varepsilon_s$. Zeman [46] expressed the dilatational dissipation rate as

$$\varepsilon_d/\varepsilon_s = c_z F\left(M_t\right), \tag{3.3}$$

with c_z=1, and M_t is the turbulent Mach number $M_t = \sqrt{2k}/a$ where *k* is the turbulent kinetic energy and *a* the speed of sound. The compressibility function $F\left(M_t\right)$ suggested by Zeman [46] is given as

$$F\left(M_t\right)_{\text{Zeman}} = 1 - exp\left\{-\left[\left(M_t - 0.1\right)/0.6\right]^2\right\} \quad \text{if } M_t > 0.1, \tag{3.4}$$

$$F\left(M_t\right)_{\text{Zeman}} = 0 \quad \text{if } M_t \leq 0.1.$$

The turbulent Mach number used by Zeman [46] is not exactly equal to M_t. He expressed the turbulent Mach number according to the sonic conditions $M_{t,\mathrm{Zeman}} = \sqrt{(\gamma+1)/2}M_t$ but for simplicity, Equation (3.4) has been considered in this form (see [45]).

Sarkar [47] derived another formula of $F(M_t)$

$$F(M_t)_{\mathrm{Sarkar}} = M_t^2. \tag{3.5}$$

Another formula proposed by Wilcox [48] is given as

$$F(M_t)_{\mathrm{Wilcox}} = M_t^2 - 0.25^2 \quad \text{if } M_t > 0.25, \tag{3.6}$$

and

$$F(M_t)_{\mathrm{Wilcox}} = 0 \quad \text{if } M_t \leq 0.25.$$

The values of M_t at which Zeman's and Wilcox's functions are zero is called the initial turbulent Mach number M_{to}, equal to 0.1 or 0.25 according to Zeman and Wilcox, respectively.

Most of the works which were conducted to investigate the compressibility effects focused on the shear layer. As free shear layers develop with jet flow, compressibility effects have to be taken into account when modeling jet flow, especially highly underexpanded jet flow.

3.1.5 Numerical considerations of the compressibility effects with jet flows

The compressibility functions mentioned above have been included in jet flow models. For example, Zheng and Bray [49] confirmed that the compressibility effects are important to be considered with supersonic jet flows. They tested Zeman's and Sarkar's compressibility functions which both improved the results of the studied jet flow. Pao and Abdol-Hamid [50] employed the k-ϵ turbulence model to simulate jet flow fields with different inlet pressure conditions. They employed Sarkar's and Wilcox's compressibility functions with supersonic jet flows (Mach number is higher than 2). Their presented results provided solid evidence on the importance of the compressibility effects on supersonic jet flows. They compared the results of their work with experimental data. The results of their simulations with compressibility corrections agreed with the experimental data which was the jet centerline velocity, whereas without compressibility corrections the results were less than the experimental data by about 30%. Gross et al. [51] and Birkby and Page [52] reported that compressibility corrections had no effects on the shock cell decay but the corrections improved the prediction of the potential core length in such way that the simulation results of supersonic jet flows agreed with the experimental ones.

The compressibility was found to affect the large-scale structures in the mixing layers of jet flow. Thurow et al. [53] reported that by increasing the Mach number of jet flow, the large-scale structures became less organized. Sung et al. [54], Balabel

et al. [55] and Bartosiewicz et al. [56] reported that, by including the compressibility correction to model a jet flow with strong shock, the k-ω SST turbulence model gave better results than the k-ϵ model.

3.2 Numerical simulations of the studied jet flow

3.2.1 Nozzle geometry and experimental data

In a weaving machine or an air jet loom (see Figure 1.2), relay nozzles are placed close to the reed where the weft yarn speed is kept constant by means of the jet flows generated by the relay nozzles. A relay nozzle may have single or multiple exit holes. However, the idea of this work is to study the jet flow which is generated by a nozzle with a single exit hole. The consideration of the nozzle being a relay nozzle is not discussed nor the interaction between the jet flow and the weft yarn. The objective of the studied case is to investigate the ability of the numerical simulations to predict correctly the supersonic flow generated by a nozzle with a single exit hole.

The cylindrical geometry of the studied nozzle is given by Picanol[1]. Figure 3.4 shows a meridional view of the geometry of the nozzle. The domain in which the air flow passes through the nozzle consists of three consecutive narrowing cylinders. The nozzle exit is one circular hole with diameter equal to 1.28 mm.

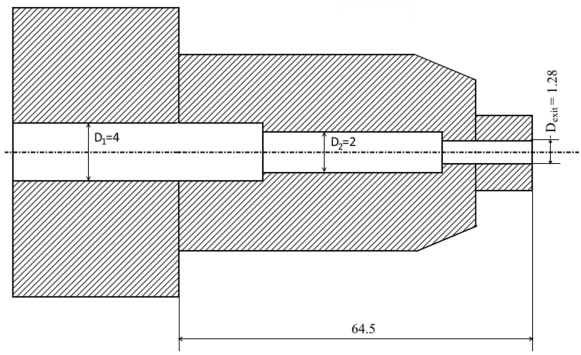

Figure 3.4: Meridional view of the geometry of the studied nozzle with dimensions in mm.

Experiments were carried out with the nozzle and the total pressure has been measured by a Pitot tube. The nozzle was supplied with compressed air with a total pressure of 5 bar relative to the atmospheric pressure. Four sections were chosen to measure the pressure, located at axial distances 44, 54, 64 and 74 mm downstream the nozzle exit. The geometry of the nozzle, as seen in Figure 3.4, is axisymmetric. It is expected that the axis of the generated jet flow coincides with the nozzle axis. This can be seen clearly in Figure 3.5. The axial distance will be considered along

1. A weaving machine producer

the x-axis. Thus, the normal distance is either along y-axis or z-axis. It can be seen in Figure 3.5 that there are no differences between the data along y or z. Therefore, the axisymmetric property of the nozzle and the generated jet flow is verified geometrically and experimentally.

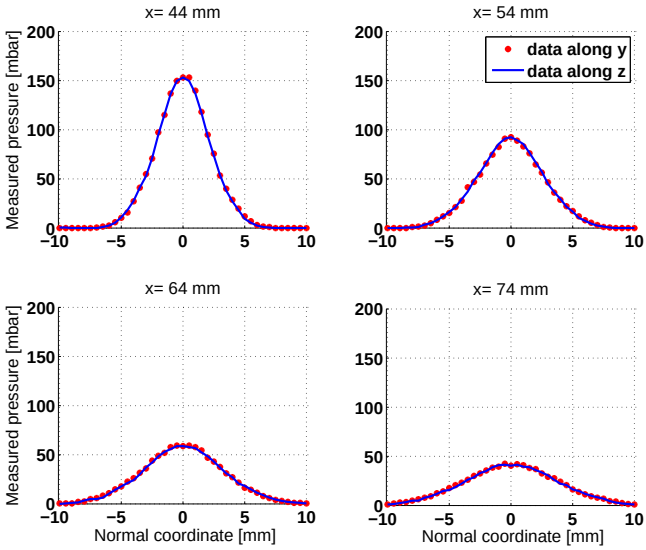

Figure 3.5: Measured pressure profiles. The coordinates are defined with the origin at the nozzle exit.

3.2.2 Numerical simulation setup

The air flow of the studied jet flow is compressible and turbulent. Thus, a turbulence model has to be used to model this flow. Two types of simulations have been carried out to simulate the studied jet flow: the RANS simulation and the LES.

RANS simulations setup: The k-ω SST model is chosen as the RANS turbulence model to carry out the simulation of the studied jet flow. This model is built to be used with bounded and free flows because it switches from k-ω to k-ϵ for free stream flow and also, according to the literature [54–56], this model gives good results with the supersonic jet flow.

Owing to the axisymmetric property of the nozzle geometry as well as the jet flow, a two-dimensional axisymmetric simulation is carried out. The fluid domain and the boundary conditions are shown in Figure 3.6.

The mesh contains rectangular (structured) and triangular (unstructured) cells. The structured mesh is constructed inside the nozzle and outside where the jet flow is expected to develop and the unstructured mesh is employed elsewhere. This combination is used to decrease the total number of cells. A part of the created mesh is shown in Figure 3.7.

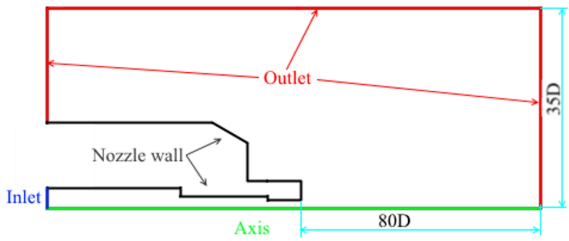

Figure 3.6: Fluid domain and the boundary conditions used with the RANS simulation.

The inlet pressure is equal to 5 bar (relative to the atmospheric pressure). The static pressure at the outlet is equal to the atmospheric pressure.

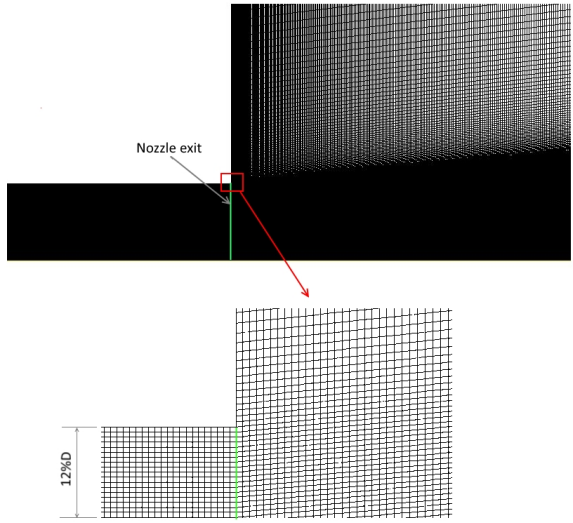

Figure 3.7: Part of the mesh used with the RANS simulation.

A mesh sensitivity has been performed to make sure that the results of the simulation are independent of the mesh. Figure 3.8 shows the Mach number plotted along the jet axis with three grids. The effects of refining the grid appear in multiple locations which are the exit of the nozzle, the region after the Mach disk (subsonic) and the expansion and compression waves. The differences between grid 1 (the coarsest grid) and grid 3 (the finest grid) are higher than the differences between grid 2 and grid 3. The differences between the three grids decrease far from the nozzle exit. The Euclidean distance, based on the Mach number values, between grid 1 and grid 2 is equal to 0.409, between grid 1 and grid 3 is equal to 0.523 and between grid 2 and grid 3 is equal to 0.312. Grid 3 is thus chosen. The step sizes and the total number of cells of the three grids are listed in Table 3.1.

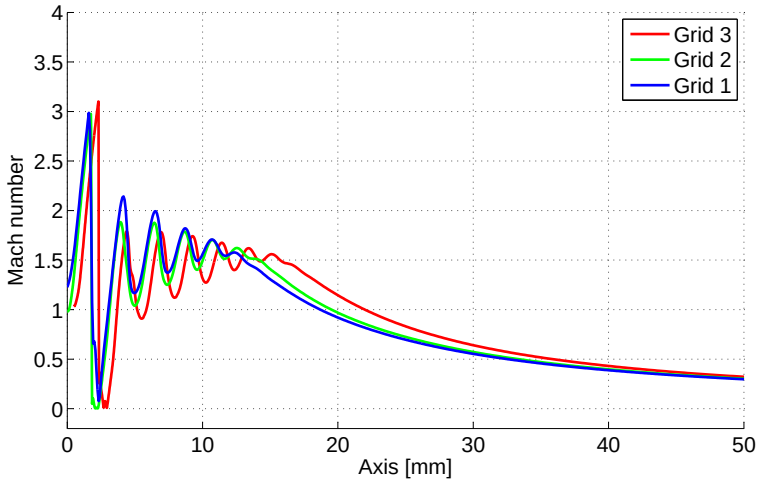

Figure 3.8: Grid sensitivity with the k-ω SST model; Grid 1 is the coarsest grid and grid 3 is the finest grid.

Table 3.1: Properties of the three grids tested with RANS.

	Step sizes ($\Delta x = \Delta y$) [m]	Total number of cells
Grid 1	1.28×10^{-5}	969 419
Grid 2	8×10^{-6}	1 201 256
Grid 3	4×10^{-6}	1 753 025

The results of grid 3 and grid 2 are not equal. However, the results of grid 3 show that inside the nozzle and at the entrance to the last cylinder, a sonic section is formed. This sonic section is due to the formation of a boundary layer as shown in Figure 3.9. The supersonic flow inside the nozzle affects the flow downstream. To test the effects of the supersonic flow inside the nozzle on the jet flow, another simulation is performed with another grid, grid 4, which is finer than grid 3 by three times. Grid 4 contains about 5×10^5 cells. Figure 3.10 shows that the values of the total pressure at the exit of the nozzle and after 15 mm downstream are affected by refining the grid. These effects are due to the expansion and compression waves which occur inside the nozzle and which are affected by the grid refinement. However, after 15 mm downstream, both grids give the same results. By consequence, the results of grid 3 are considered to be reported.

Large-eddy simulation setup: The Smagorinsky-Lilly [14, 57] model is employed as the subgrid-scale model for the LES. The model constant C_s equals 0.1 [58]. A two-dimensional axisymmetric simulation cannot be performed with LES, only a three-dimensional simulation can be. Moreover, if a three-dimensional mesh was constructed for the RANS simulation, that grid would not be good enough to be used with LES and it should be refined. Therefore, a three-dimensional fluid domain is created with the same dimensions as the domain shown in figure 3.6 with the same

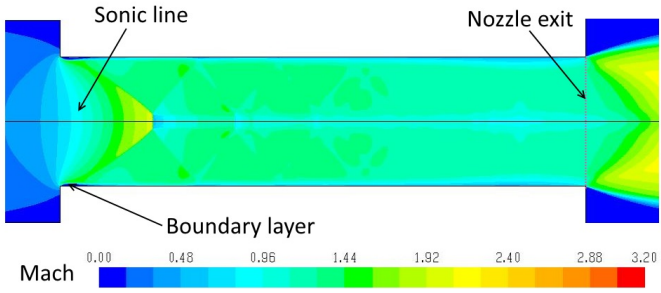

Figure 3.9: Sonic section at the entrance of the last cylinder of the nozzle.

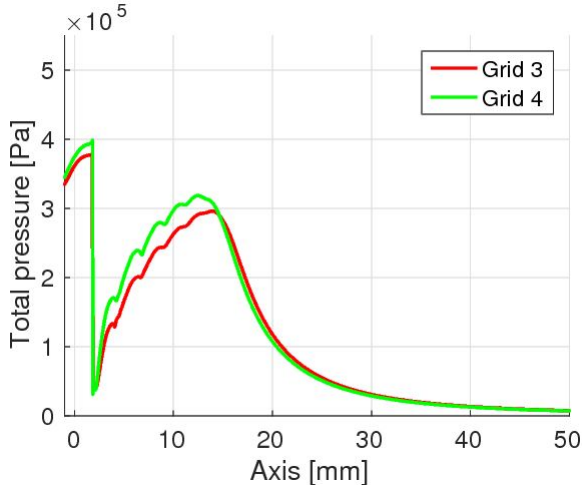

Figure 3.10: Effects of the supersonic flow inside the nozzle on the jet flow.

boundary conditions except the axis condition. The mesh sizes at the nozzle exit are $\triangle x = \triangle y = \triangle z = 3 \times 10^{-5} = D_{exit}/42$. This mesh size is chosen according to previous studies [17, 59]. The Reynolds number at the exit of the nozzle is calculated based on the flow properties and the diameter of the nozzle:

$$Re_{exit} = \frac{V_e \rho_e D_e}{\mu_e} = \frac{335 \times 3.25 \times 0.00128}{1.7894 \times 10^{-5}} = 77898. \tag{3.7}$$

With this value of Reynolds number and according to [17, 59], the above mentioned mesh sizes are sufficient to give reliable results with LES. Figure 3.11 shows a part of the mesh in the xy-plane. The resolution of the mesh, as seen, is increased in the region where the jet flow and the shear layers will develop. The grid is structured and unstructured. The total number of elements is about 13.5×10^6 cells. No mesh sensitivity has been performed with LES.

The different specifications and setup with the RANS simulation and the LES are summarized in Table 3.2. It can be observed that the mesh size for the RANS sim-

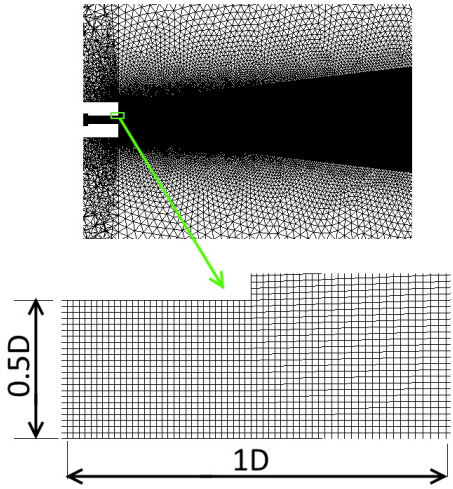

Figure 3.11: Part of the LES grid in the xy-plane.

ulation is smaller than the mesh size for the LES. The mesh size with the LES is limited due to the domain of the simulation. As the domain of the simulation with the RANS is two-dimensional axisymmetric, it is possible to refine the mesh and to perform a mesh sensitivity because the number of cells increases with a second power. However, this is not the case with the LES. The three-dimensional domain of calculation required with the LES constrains the mesh size. Moreover, the simulation with the RANS is steady state, but with the LES, it has to be unsteady. Due to these reasons, the mesh size which is used for the LES should result in an acceptable number of cells and guarantee good results. Therefore, the mesh size is adopted from previous works. Ansys Fluent 14.0 was used to perform the simulations. The pressure-based solver is employed for both RANS simulations and LES with the coupled scheme for the velocity-pressure coupling, second-order methods for spatial and temporal discretizations (upwind, implicit) except for the momentum equations in the LES for which the bounded central differencing scheme was used.

Table 3.2: Specifications of the RANS simulation on grid 3 and the LES.

	RANS	**LES**
Computational domain	2D axisymmetric	3D
Mesh size at nozzle exit	$D_{exit}/320$	$D_{exit}/42$
Total number of mesh elements	1.75×10^6	13.5×10^6
Model	k-ω SST	Smagorinsky-Lilly
Simulation type	Steady	Transient
Time step	-	$5 \times 10^{-7} s$
Total simulation time	-	0.02 s

3.3 Results

3.3.1 Results of Smagorinsky-Lilly LES and k-ω SST RANS simulation

Figure 3.12 shows the contours of the Mach number and Figure 3.13 shows the structure of the jet flow obtained from RANS. The numbers in Figure 3.13 will be explained further. Moreover, the contours of static pressure in the near-field are shown in Figure 3.14. The general highly underexpanded jet flow pattern is obtained by LES as well as by RANS simulation. At the exit of the nozzle, the pressure is higher than the atmospheric pressure (see Figure 3.14). Thus, the flow expands to high velocities via a Prandtl-Meyer expansion fan (number 1 in Figure 3.13). The expansion waves stop when their pressure becomes equal to the atmospheric one (the slip line, number 8), and they reflect as compression waves towards the axis. The interaction between the waves forms an oblique shock. The oblique shock, also called the barrel shock, is number 2 in Figure 3.13. Due to the pressure differences, the compression waves do not meet in the same point on the axis. Consequently, a Mach disk (number 5) or normal shock appears. The triple point (number 4) is the point where the Mach disk and the barrel shock intersect and cause a reflected shock. The reflected shock (number 3) goes towards the outer zone and stops when it meets with the slip line and reflects as expansion waves towards the axis. Number 6 in Figure 3.13 is the internal shear layer which separates the subsonic and the supersonic flows. Number 7 is the free shear layer or the mixing layer. It can be seen in Figure 3.12 that the free shear layer thickness increases by moving downstream.

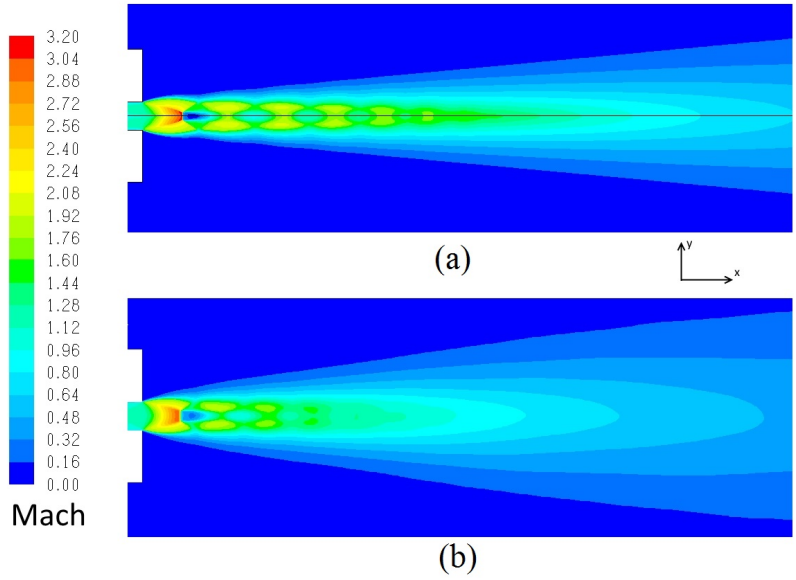

Figure 3.12: Contours of Mach number in the xy-plane: (a) RANS results; (b) mean from LES results. The length of the shown view is x/D=24.

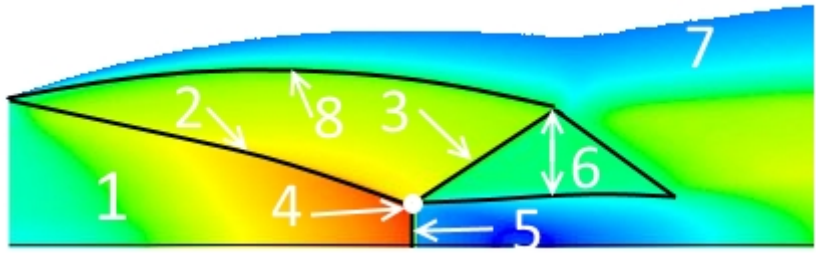

Figure 3.13: Near-field structure of the jet flow obtained from RANS simulation. The shown contours and scale are the same as in Figure 3.12. The length of the shown domain is x/D=2.75.

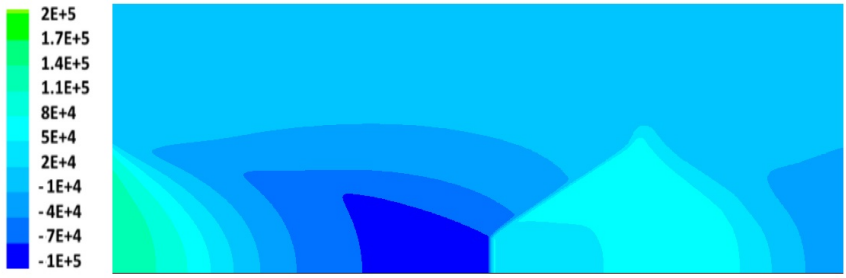

Figure 3.14: Contours of static pressure [Pa] in the xy-plane obtained from RANS simulation. The length and the location of the shown domain is the same as in Figure 3.13.

In the literature, the Mach disk location and diameter have been analyzed and empirical relations have been derived to calculate them. The Mach disk location is measured from the nozzle exit and its diameter is called its width and it is determined by the triple point. The first empirical formulas to calculate these lengths were suggested by Ashkenas and Sherman [60]. The main parameter which affects the Mach disk location and diameter is the pressure ratio which is the supplied pressure over the ambient pressure P_o/P_∞. Other parameters may also affect these lengths [2]. Franquet et al. [2] discussed these parameters in great detail based on an overview of previous studies. From their works Formulas (3.8) and (3.9) are taken and employed to calculate the location and the diameter of the Mach disk.

$$\frac{L_{MD}}{D_{exit}} = 0.645497\sqrt{\frac{P_o}{P_\infty}} = 0.645497\sqrt{\frac{601325}{101325}} = 1.57249, \tag{3.8}$$

$$\frac{D_{MD}}{D_{exit}} = 0.31\sqrt{\frac{P_o}{P_\infty} - 5} = 0.31\sqrt{\frac{601325}{101325} - 5} = 0.2996, \tag{3.9}$$

where L_{MD} and D_{MD} are the location and the diameter of the Mach disk, respectively. D_{exit} is the nozzle exit diameter (1.28mm). P_o and P_∞ are the supplied and the ambient pressure, respectively.

Figure 3.15 shows the location and the diameter of the Mach disk obtained from LES and from RANS. The numerically obtained values and the ones which are calculated based on Equation (3.8) and (3.9) are listed in Table 3.3. From Table 3.3 and Figure 3.15 it can be seen that LES and RANS underestimate the location of the Mach disk and L_{MD} is shortest with LES. By contrast, RANS underestimates the diameter of the Mach disk and LES overestimates it. However, the constants in the empirical relations (3.8) and (3.9) have been estimated based on somewhat different test cases and they are still under investigation.

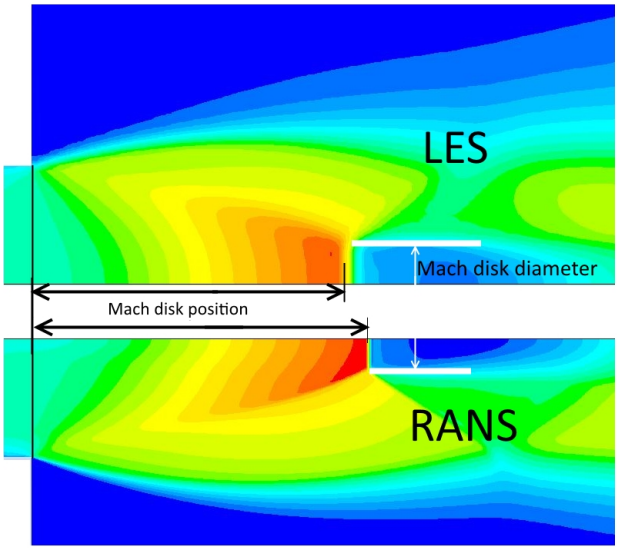

Figure 3.15: Mach disk obtained from LES (top) and from RANS (bottom).

Table 3.3: Dimensions of the Mach disk. The percentage values are the deviations from the empirical values.

	Location (L_{MD}/D_{exit})	Diameter (D_{MD}/D_{exit})
Eq (3.8) and (3.9)	1.572	0.299
RANS	1.417 (-9.8%)	0.25 (-16.3%)
LES	1.346 (-14.3%)	0.34 (+13.7%)

It can be said that the near-field zone of the obtained jet flow by RANS and LES agrees with the general pattern of the highly underexpanded jet flow. The near-field zone of the jet flow ends when the free shear layers mix with the core zone. In Figure 3.12 it can be noticed that the core zone obtained from RANS is longer than the one from LES. It may be possible that due to the high Reynolds number LES captures

a high level of turbulence in the flow and thus the kinetic energy dissipates more with LES than with RANS. The spreading of the flow or the thickness of the free shear layers is larger with LES than with RANS. Dauptain et al. [59] reported that the obtained thickness of the free shear layer of a jet flow was larger from LES than the thickness seen in experiments.

Figure 3.16 and Figure 3.17 show comparisons between the values of the total pressure obtained from experiment, RANS and LES (mean values) along the axis in Figure 3.16 and along the normal coordinate (y or z) in Figure 3.17.

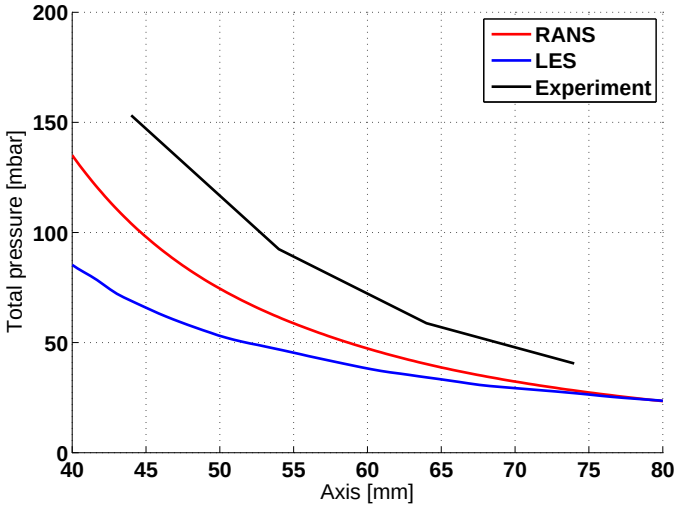

Figure 3.16: Total pressure along the axis of the jet. The origin of the axis coordinate is at the nozzle exit.

Figure 3.16 shows that there is apparent discrepancy between the experiment, RANS and LES. Moreover, the maximum difference between the experiment and the RANS results along the axis is about 30%, while the maximum difference between the experiment and the LES results along the axis is about 50% at x=44 mm, the difference decreases downstream and it is about 33% at x=74 mm. Figure 3.17 shows that there is a radial coordinate (y or z) at which the experimental, RANS and LES data intersect. After the point of intersection, LES gives higher values of the total pressure, while RANS gives close values in comparison to the experimental data. Therefore, the results of RANS and LES do not agree with the experimental data. RANS gives better results than LES but downstream at x=74mm they give almost the same results. By linking these comparisons to the flow patterns discussed above, it can be said that the longer core region predicted by RANS than by LES might lead to better results close to the exit but not far downstream where both give the same results. RANS predicts, to some extent, the same spreading of the jet flow as in the experiment.

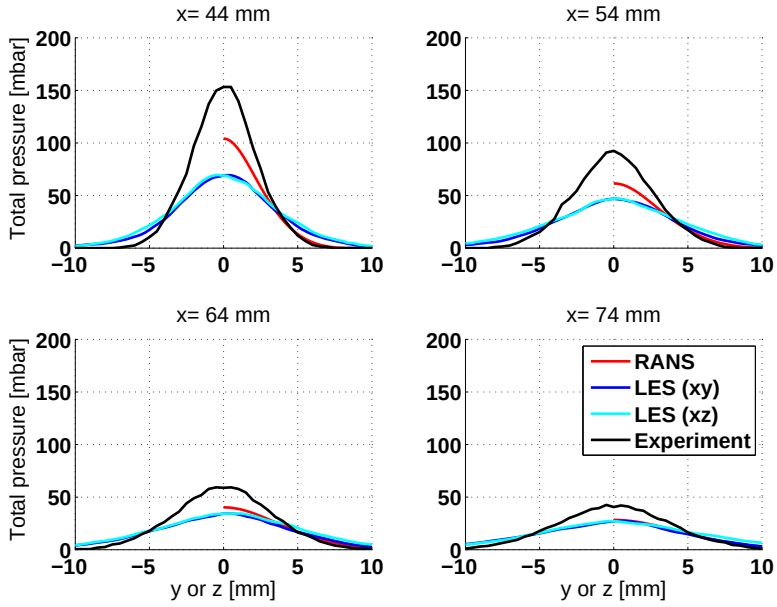

Figure 3.17: Total pressure profiles.

3.3.2 Results of other LES

With the Smagorinsky-Lilly subgrid-scale turbulence model, the model constant C_s is either a fixed value or a dynamic one. Smagorinsky derived the basic model with fixed constant. Later, Germano et al. [61] proposed to adapt the Smagorinsky model with a dynamic model parameter. The proposed procedure involves calculating the constant during the simulation at each point in time and space. Thus, the dynamic Smagorinsky-Lilly model is with the same hypothesis as the basic model but with dynamic constant. The dynamic model has been used to perform another LES for the studied jet flow.

Moreover, in the previously performed LES, the dynamic viscosity was fixed, while the dynamic viscosity of a fluid changes with temperature. The Sutherland's law, Equation (3.10), expresses the dynamic viscosity as a function of temperature.

$$\frac{\mu\left(T\right)}{\mu_{ref}\left(T_{ref}\right)} = \left(\frac{T}{T_{ref}}\right)^{3/2} \frac{T_{ref}+S}{T+S}, \tag{3.10}$$

where $\mu(T)$ is the dynamic viscosity at temperature T and μ_{ref} is the reference dynamic viscosity at the reference temperature T_{ref} (for air $\mu_{ref} = 1.716{\times}10^{-5} kg/ms$ and $T_{ref} = 273.11K$). S is the effective temperature or the Sutherland's temperature and for air $S = 110.56K$.

Figure 3.18 shows that the mean static temperature, obtained with the original LES simulation, changes significantly around the boundaries of the Mach disk. More-

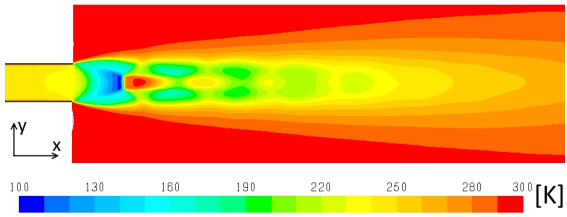

Figure 3.18: Contours of mean static temperature obtained from LES in the xy-plane where z=0.

over, as the flow field contains waves of compression and expansion, the temperature changes across these waves. The expansion of the flow decreases the temperature and the other way around with compression. Thus, according to Sutherland's law, the dynamic viscosity changes with the observed changes of the temperature. Therefore, another simulation has been performed with the basic Smagorinsky-Lilly model ($C_s = 0.1$) and with the dynamic viscosity changes according to Sutherland's law. Table 3.4 summarizes all simulations which have been performed with LES.

Table 3.4: Summary of the carried out LESs, the first simulation is the one whose results have been presented in the previous section.

Simulation	Subgrid-scale model	Model constant C_s	Dynamic viscosity $[kg/ms]$
Original	Smagorinsky-Lilly	0.1	constant (1.7894×10^{-5})
Second	Smagorinsky-Lilly	dynamic	constant (1.7894×10^{-5})
Third	Smagorinsky-Lilly	0.1	Sutherland's law

Figure 3.19 shows the mean Mach number along the axis obtained from the LESs. The near-field zone or the core zone is considered as the zone where the compression and expansion waves take place. In Figure 3.19 the number of crests or troughs will be counted to measure the core zone. In comparison to the previous results ($C_s = 0.1, \mu(constant)$) (5 crests), the dynamic model gives a longer core zone (6 crests) with higher Mach numbers, while with the dynamic viscosity changes according to Sutherland's law the core zone is shorter (4 crests) with lower Mach numbers. In the far-field zone the dynamic model and the basic model give the same mean values of the Mach number, while the mean Mach number is lower with temperature dependent viscosity. It is clear that the results of LES with viscosity changes according to Sutherland's law have significantly changed, more precisely, it is more dissipative.

The root-mean square (RMS) of the Mach number is shown is Figure 3.20. It can be seen that the values of RMS Mach number obtained from the simulation with temperature dependent viscosity are the highest and the ones from the dynamic model are the lowest. Moreover, Figure 3.21 shows that, after the nozzle exit, the high values of RMS Mach number coincide with the low values of the dynamic viscosity. It may be possible that a lower viscosity results in a higher Reynolds number and thus more turbulent flow.

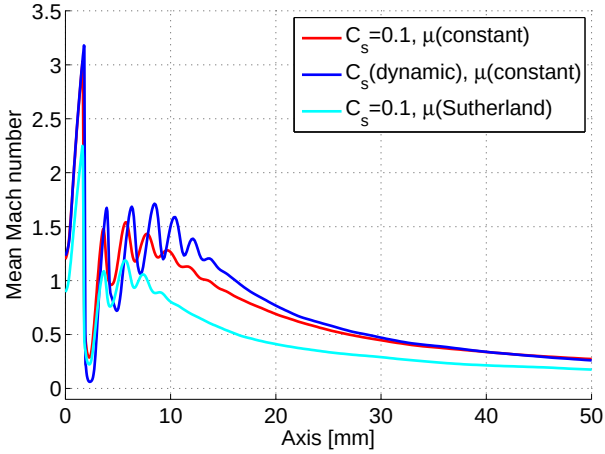

Figure 3.19: Mean Mach number along the axis obtained from LESs.

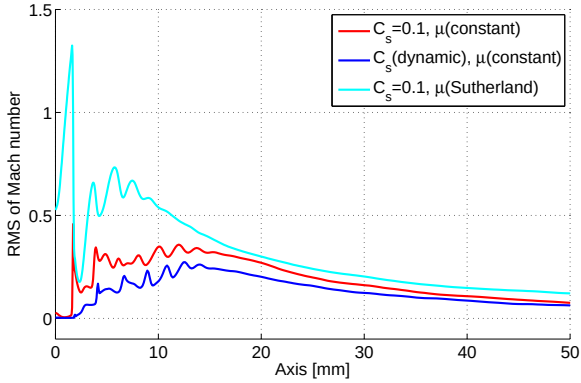

Figure 3.20: Root-mean square Mach number along the axis obtained from LESs.

Figure 3.22 shows a comparison of the total pressure obtained from the different LESs and from the experiment. It can be seen that none of the simulation results is close to the experimental data, the results of the simulation with temperature dependent dynamic viscosity are the lowest and there are no high differences between the results of the static and dynamic model constant.

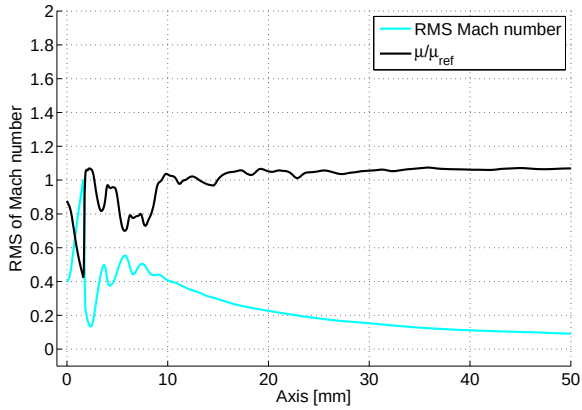

Figure 3.21: Dynamic viscosity (scaled by the reference dynamic viscosity) and RMS Mach number along the axis.

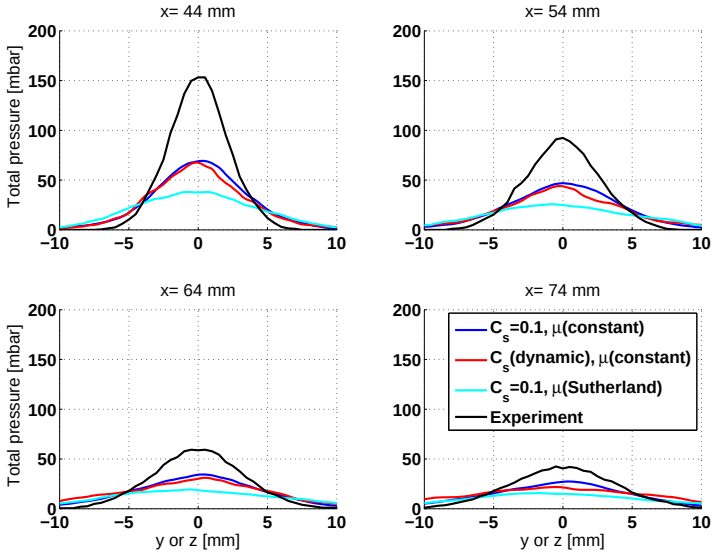

Figure 3.22: Total pressure profiles obtained from LESs.

3.3.3 Results of another model with RANS

Many turbulence models have been developed for RANS simulation. From a general point of view, the models can be used to simulate any turbulent flow. However, it has been reported that each model gives satisfactory results for some cases and not for others. For the studied highly underexpanded jet flow, the k-ω SST model has been first used to simulate the flow field. As it is shown before, this model has not given good results in comparison to the experimental data. Thus, other models may be used to investigate whether or not the RANS simulations can predict correctly the studied highly underexpanded jet flow.

Testing other turbulence models is limited to a two-equation model. This means that only the k-ω and k-ϵ models are used. During the procedure of testing another turbulence model and before comparing the obtained results of the total pressure with the experimental data, the obtained flow field was examined. This means that, for example, if a turbulence model did not succeed in capturing the Mach disk and the subsonic flow after it, the results of that model were rejected. The k-ϵ RNG model [62] has been found to simulate the flow pattern of the studied jet with the associated characteristics. Thus, the results with this model will be shown and compared.

Figure 3.23 shows a comparison of the Mach number along the axis of the jet obtained from the results with the k-ω SST and k-ϵ RNG models. Figure 3.24 shows a comparison of the total pressure. It can be seen in Figure 3.23 and 3.24 that changing the turbulence model has not improved the results in comparison to the experimental data. The differences between k-ω SST and k-ϵ RNG are small.

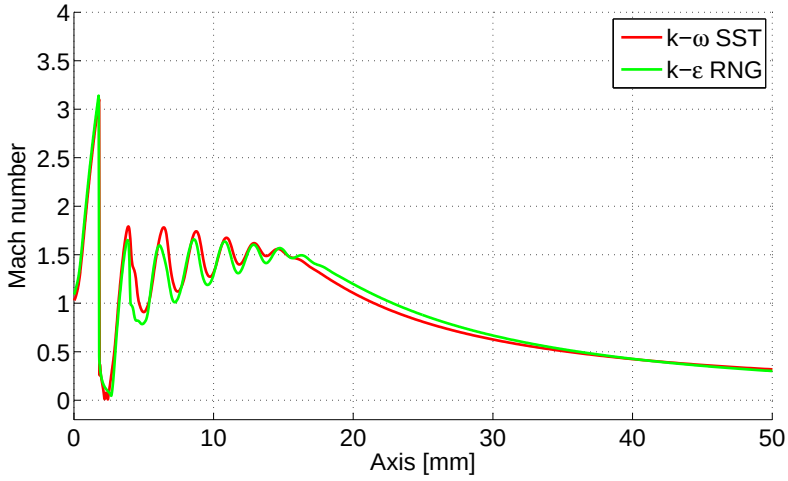

Figure 3.23: Mach number along the axis obtained from RANS simulations.

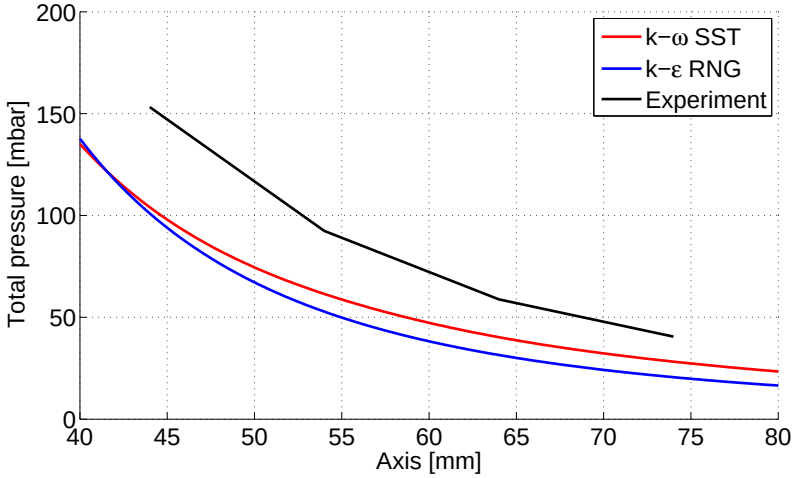

Figure 3.24: Total pressure along the axis obtained from RANS simulations.

3.3.4 Compressibility corrections

From the results presented above, it can be said that neither RANS simulations nor LESs have predicted correctly the far-field zone of the studied jet flow. This conclusion was also reported by previous studies jet flows, for example [24, 28, 30, 31, 63]. The flow field of the highly underexpanded jet is far from being completely understood or correctly captured [2]. The turbulence models which have been developed to be used with RANS simulations need further validations with the jet flow [63]. The numerical schemes, the grid resolution, the inflow conditions and the subgrid-scale model influence the results of large-eddy simulations [64]. For an incompressible flow, the turbulence affects the velocity and the pressure, while, for a compressible flow, the turbulence affects additionally the density. Most of the research on the compressible turbulence agreed that its effects on the flow are dissipative. The extra dissipation was first related to the presence of eddy shocklets as an assumption suggested by Zeman [46]. These eddy shocklets are the small shocks which occur when the convective speed of the turbulent eddy is higher than the speed of sound. However, their influence on the average dissipation rate is small [3].

Later, as mentioned before, it was suggested to take the effects of compressibility (more than the influence of the shocklets) on the turbulence into account by adding an additional dissipation part ε_d which is called the dilatational dissipation part. Then, compressibility functions have been derived to calculate the dilatational dissipation.

The functions of the compressibility corrections which were suggested by Wilcox (Equations (3.6)) and Sarkar (Equation (3.5)) have been employed with RANS turbulence models. These two functions are specifically mentioned here because they are implemented in Ansys Fluent 14.0 which has been employed to carry out the

simulations. Sarkar's compressibility correction function has been employed with the k-ϵ model and Wilcox's function with the k-ω model. These two functions are similar but the difference between them is the value of the initial turbulent Mach number. During simulations, the compressibility correction functions are not equal to zero when the turbulent Mach number is higher than the initial one. Therefore, from Equation (3.5) and (3.6) it can be seen that the initial turbulent Mach number equals 0 and 0.25 with Sarkar and Wilcox, respectively. This means that, in the results presented, the compressibility correction was taken into account everywhere in the turbulent flow with k-ϵ model, whereas with k-ω model the correction was evaluated just where $M_t > 0.25$.

Figure 3.25 shows the turbulent Mach number calculated from the results with k-ω SST model. The value in Figure 3.25 ranges from 0 to 0.25, thus the region without color in Figure 3.25 corresponds to $M_t > 0.25$. It can be seen that there is large region in which the compressibility correction function was not evaluated as $M_t \leq 0.25$. Moreover, Zeman [46] recommended to use $M_{to} = 0.1$ for flows with free shear layers. Therefore, the initial value of the turbulent Mach number is decreased to 0.1 instead of 0.25.

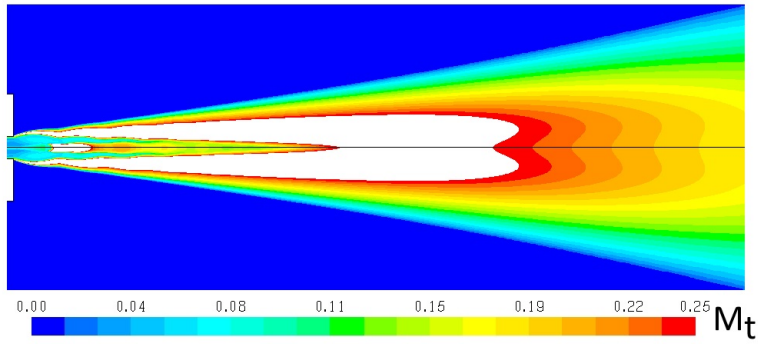

Figure 3.25: Turbulent Mach number ($M_t = \sqrt{2k}/a$) calculated from the results with k-ω SST model. The length of the shown view is x/D=35.

Figure 3.26 shows a comparison of Mach number along the axis of the jet with the default value of the initial turbulent Mach number ($M_{to} = 0.25$) and the other value ($M_{to} = 0.1$). The comparison with and without correction is made in the following section. It can be seen in Figure 3.26 that reducing the initial value of M_{to} does not affect the location of the Mach disk nor the maximum value of the Mach number. Moreover, the core zone of the jet flow extends further downstream with $M_{to} = 0.1$ than with $M_{to} = 0.25$. The Mach number of the jet increases in the far-field zone when we reduce M_{to}.

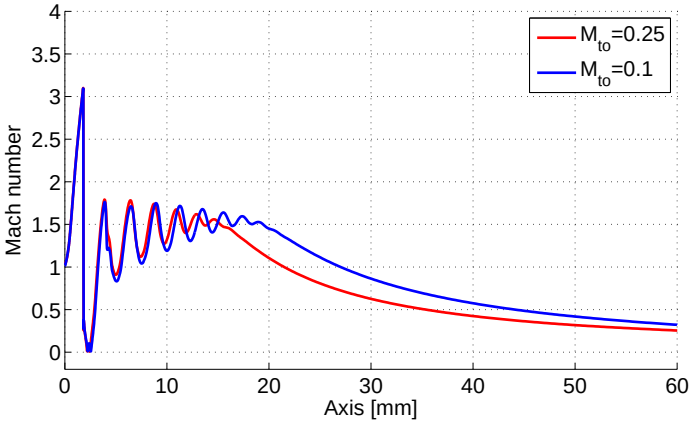

Figure 3.26: Mach number along the jet axis obtained from the results with k-ω SST model and with two initial turbulent Mach numbers.

Figure 3.27 and 3.28 show a comparison of total pressure obtained from the simulations with different M_{to} and from the experiment. The results with $M_{to} = 0.1$ are better than the results with $M_{to} = 0.25$. The profiles of the total pressure with $M_{to} = 0.1$ show less high differences than $M_{to} = 0.25$ in comparison to the experimental values close to the jet axis at x=44mm and 54mm. Furthermore, at x=64mm and 74mm the results with $M_{to} = 0.1$ are almost identical to the experiments.

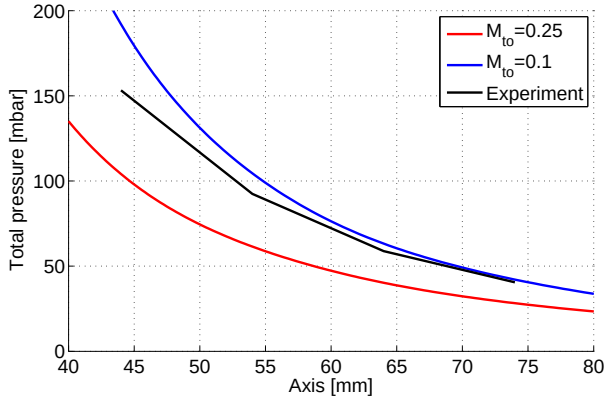

Figure 3.27: Total pressure along the jet axis obtained from k-ω SST with different M_{to} and from the experiment.

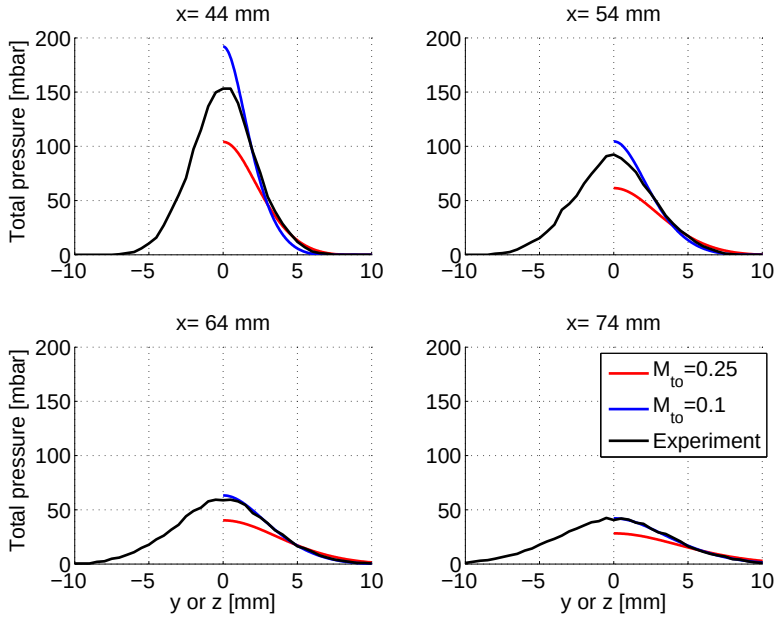

Figure 3.28: Total pressure profiles obtained from k-ω SST with different M_{to} and from the experiment.

Therefore, the compressibility correction with a reduced initial turbulent Mach number has improved the results of the RANS simulation. The longer core region predicted with $M_{to} = 0.1$ than with $M_{to} = 0.25$ had been reported in other studies [50, 51]. The initial turbulent Mach number is reduced to 0.1 because this value has been used in [63]. However, the effects of the compressibility correction as well as the initial turbulent Mach number should be investigated further in order to analyze their effects.

3.3.5 Further analysis of the initial turbulent Mach number

The effects of reducing the initial turbulent Mach number has been presented above for one value. In this section, the results of reducing M_{to} to many values will be shown and discussed.

Simulations with many values of M_{to} have been performed with preserving all other simulation setup parameters except the grid. It was no problem carrying out the simulations with the finest grid but this costs a lot of time. Therefore, the simulations to investigate the effects of reducing the initial turbulent Mach number have been carried out with a coarser grid than the finest grid.

Figure 3.29 shows the effects of reducing the initial turbulent Mach number. By reducing M_{to}, the core region extends further downstream. The core region length increases by about 4.5 mm with $M_{to} = 0$ compared to $M_{to} = 0.25$. Without

compressibility correction, the results are significantly different. The compressibility correction does not affect the first cell of the jet flow (x=0 to 2 mm).

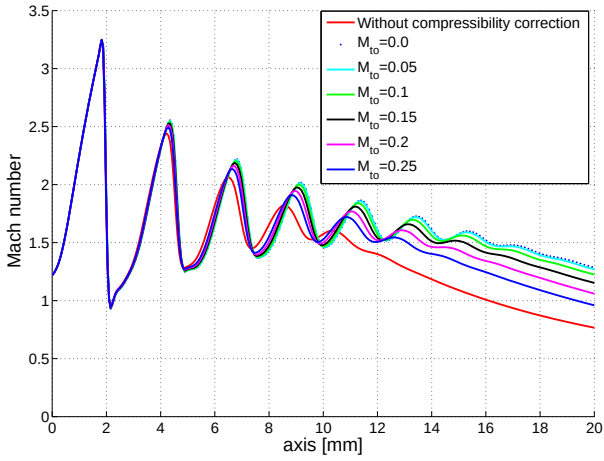

Figure 3.29: Mach number along the axis with different initial turbulent Mach numbers.

The results presented above are with an inlet pressure equal to 5 bar (relative to the atmospheric pressure). Thus, the compressibility effects exist strongly in the flow field and the compressibility corrections have affected the results. However, another test has been performed to investigate the effects of the compressibility correction with weakly compressible flow, with an inlet pressure equal to 10^4 Pa. Figure 3.30 shows the Mach number along the axis of the jet with and without compressibility correction. The initial turbulent Mach number is set to zero. It is clearly seen that the compressibility correction does not affect the flow field. Therefore, the compressibility correction is proportional to the compressibility of the flow.

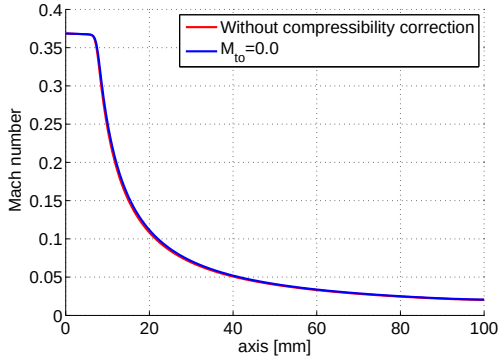

Figure 3.30: Compressibility correction effects with a weakly compressible flow, nozzle inlet pressure equals 10^4 Pa.

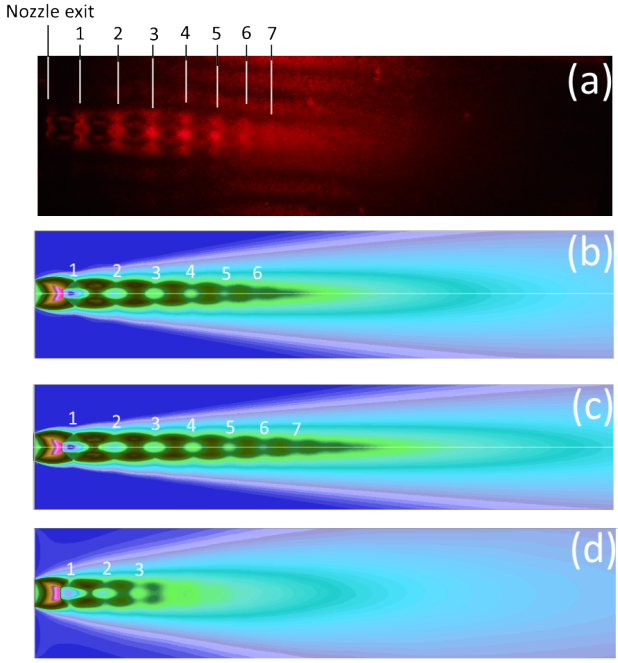

Figure 3.31: Jet flow pattern; (a) Laser image; (b) Obtained with k-ω SST with $M_{to} = 0.25$; (c) Obtained with k-ω SST with $M_{to} = 0.1$; (d) Obtained from LES with $C_s = 0.1$. The shown flow fields of the simulations are contours of Mach number ranges from 0 to 3.2.

Figure 3.31 shows the captured flow field from the experiment and the contours of the Mach number from the simulations. To compare the experimental image with those from the simulations, the nodes which are counted in Figures 3.31 are

compared. The seventh node in Figure 3.31(a) is not clearly seen but this node or region is highlighted and compared. None of the simulation flow fields correspond exactly to the experimental image. The core region from LES and from RANS with k-ω SST with $M_{to} = 0.25$ are shorter than the experimental one, whereas, the core region with k-ω SST with $M_{to} = 0.1$ is longer than the experimental one. The flow dissipates early with LES. This fast dissipation with LES may be due to two reasons: a coarse grid and ignoring the compressibility effects (see [65]). With the filtering operation employed with LES, the coarse grid results in an inaccurate flow field. The effects of the dilatational dissipation on the results of LES have been investigated by Chai and Mahesh [66]. They developed a k-equation model to calculate the subgrid-scale model kinetic energy for LES for compressible flows. With the proposed k-equation model, the dilatational dissipation term is included. They showed that if the dilatational dissipation term is not taken into account, the flow dissipates after the shock more than if it is. Moreover, they proved that the dilatational dissipation has effects on the mean values. However, Moin et al. [65] reported that the dynamic subgrid-scale model takes into account the dilatational dissipation. As the results with fixed and dynamic C_s are less than 20% different the grid which has been used with LES in this work may not be fine enough to obtain good results in comparison to the experiments.

It is not straightforward to compare the turbulent quantities obtained from LES and from RANS due to the different procedure in dealing with turbulent flows. However, as multiple simulations have been performed with LES as well as with RANS, the different results of one type, LES or RANS, can be compared. Figure 3.32 shows that the turbulent kinetic energy decreases sharply after the Mach disk because the flow becomes subsonic after the Mach disk. Moreover, the values of the turbulent viscosity ratio are not high in the core region (x < 15 mm) as it is seen in Figure 3.33. Downstream, when the free shear layers mix with the core flow, the flow becomes fully turbulent and due to the high turbulent viscosity, the flow dissipates by turbulent effects. It is seen in Figure 3.33 that the turbulent viscosity ratio reaches high values earlier with $M_{to} = 0.25$ than with $M_{to} = 0.1$.

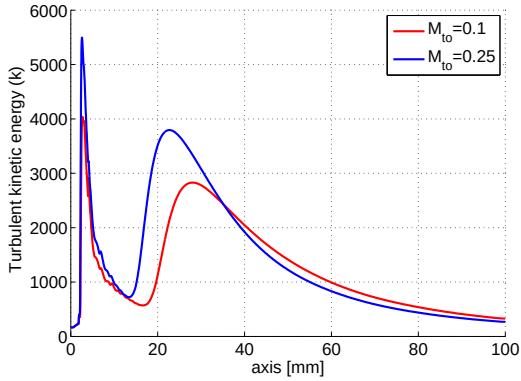

Figure 3.32: Turbulent kinetic energy (k $[m^2/s^2]$) along the axis obtained from RANS with two different M_{to}.

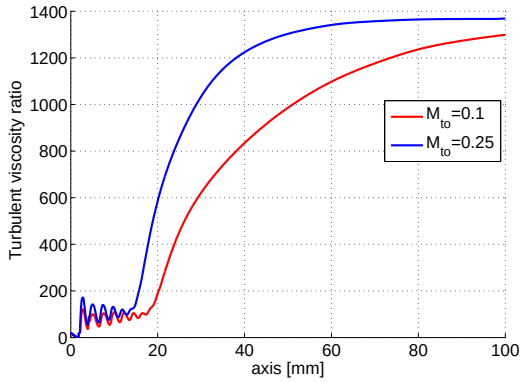

Figure 3.33: Turbulent viscosity ratio along the axis obtained from RANS with two different M_{to}.

3.4 Conclusion

In this chapter, the numerical results of RANS simulations and LES of a highly underexpanded jet flow have been presented and compared with experimental data of total pressure and one laser image of the jet flow pattern. The general pattern of the highly underexpanded jet flow can be divided into three zones: the near-field, the far-field and the shear layers or mixing layers.

The near-field zone has been captured by LES and by RANS where the obtained dimensions of the Mach disk are acceptable in comparison to empirically calculated dimensions. Moreover, the obtained core region which belongs to the near-field zone is shorter with LES than with RANS. The visible, not calculated, thickness of the shear layers or the mixing layers is larger with LES than with RANS. This observation had also been reported in previous works conducted with LES. The far-field zone of the studied jet flow has been evaluated based on a comparison of total pressure. The measured total pressures have been compared with the obtained ones from LES and from RANS. The comparison shows that there are apparent discrepancies between them, even with different turbulence models with RANS as well as with LES.

With the default value of the initial turbulent Mach number, which equals 0.25 with the k-ω SST model, it has been found that the compressibility correction is not evaluated in large region of the jet flow. Due to a recommended value to be used with a free shear layer, the initial turbulent Mach number has been reduced to 0.1. By reducing the initial turbulent Mach number, the results of RANS with k-ω SST model have improved significantly and a good agreement has been found in comparison to the experimental data. The LES with Smagorinsky-Lilly subgrid-scale model, as reported, does not include the compressibility effects or corrections, whereas the dynamic model takes them into account. However, with the dynamic model the results of the LES do not agree with the experimental data.

The results of LES depend mainly on the grid. According to the obtained results by LES, the grid which has been employed seems to be coarse. The results of LES in the very near-field zone where the resolution of the used grid is good are acceptable. However, in the far-field zone where the comparison of the total pressure has been made the grid resolution may not be enough. Preserving a good resolution in the far-field zone was not possible because in this case the number of cells increases and high computing resources are required to carry out the simulation within acceptable time.

It can be said that for an industrial application it is sufficient to investigate a highly underexpanded jet flow based on RANS simulations with the k-ω SST model and with a recommended value of the initial turbulent Mach number. By contrast, to understand physically the phenomena associated with this type of flow and to capture the near-field and the far-field zones correctly, the LES with the dynamic subgrid-scale model on a sufficiently fine grid is the best candidate.

In the following chapters, the studied cases involve compressible flows or internal jet flows. Therefore, the compressibility effects are taken into account. This means that if large-eddy simulations are performed, the dynamic Smagorinsky-Lilly model is used. Moreover, the k-ω SST model is used with the RANS simulations, but the initial turbulent Mach number is not reduced to 0.1, it is kept equal to 0.25 as recommended for internal compressible flows.

Chapter 4

Numerical and experimental analysis of ends-together yarn splicing

For some engineering applications it is not possible to perform fluid-structure interaction simulations of flow-structure due to the complexity of the applications. In this chapter, pneumatic yarn splicing is presented as an example of such a case which is studied based on air flow simulations and on results of experiments. Large-eddy simulation of the air flow is performed in four splicing chambers. The results of the simulations are analyzed and linked to the experimental results. This chapter has been published in [8].

4.1 Introduction

Pneumatic splicing is a well-known technique in the textile industry. It is used for joining two yarn ends together by injecting air with high speed into a splicing chamber. The resultant joint needs to have the same properties as the original yarn, especially regarding strength and appearance. The process of yarn splicing is done by consecutive steps. The two yarn ends are placed together into the splicing chamber. The yarn can be introduced in the splicing chamber from opposing ends or from the same side. The latter is called superimposing or ends-together and this is studied in this work. The cover of the chamber (the lid) is then closed and they are cut together with scissors. Next, a compressed and turbulent air flow is injected into the chamber with high velocity. The aerodynamic forces created by the flow field excite the yarn ends to move, untwist and to splice them. The untwisting stage is important to prepare the yarn ends to be spliced and it affects greatly the quality of the splicing. Th process of yarn splicing affects both the quality of the yarn being spliced and the productivity of the machine in which it is used because it affects the subsequent process.

Yarn air splicing is simple in principle, but it is complex in details. Moreover, observing the splicing is difficult due to the short time of the process and the small geometry of the splicing chamber, even with current camera technology. To date, simulating yarn splicing is difficult because of the strong interaction of the yarn filaments with each other and with the turbulent air jet. Due to this complexity, most previous studies have been focusing on external parameters which can be measured and controlled and are based on experimental results. For example, Webb et al. [67] studied experimentally the influence of air pressure and duration on the splice strength. They could find the best inlet pressure and duration with specific geometries of the splicing chamber. The most important conclusion of their work was the effects of the splicing chamber geometry on the strength of the splice. This conclusion had not been reported in studies preceding theirs. Later, Webb et al. [68] verified that Computational Fluid Dynamics (CFD) can be used to analyze the flow field inside an empty splicing chamber (with the absence of yarns). They found good agreement between the air flow simulations and the results of a visualization technique. Moreover, they investigated the flow patterns inside two splicing chambers and they found that strong vortices resulted in better splicing. Zhou and Qin [69] carried out numerical simulations of the flow field inside different splicing chamber geometries and also they confirmed the effectiveness of CFD in studying pneumatic splicing. These two works [68, 69] employed the k-ϵ turbulence model for the flow simulations which were performed in ends-opposed splicing chambers.

Xing and Ye [70] used the k-ϵ model to simulate the flow field inside an untwisting pipe of a splicing chamber. By analyzing the flow field, they discussed the principle of yarn untwisting and their conclusions confirmed the pneumatic splicer maker's suggestions principle. Wu et al. [71] investigated the structural parameters which affect the untwisting stage. They made comparisons between the flow field simulation and experimental data. They determined the geometrical parameters that affect and improve the performance of untwisting yarn ends.

Some works studied yarn splicing based only on CFD. Degong et al. [72] studied the influence of the inlet pressure on the velocity and pressure inside a splicing chamber. In this way they could determine the best inlet condition for a particular chamber geometry. Wang et al. [73] concluded that a rounded shape of a splicing chamber is better than a square or a hexagon. Moreover, when investigating yarn splicing experimentally, CFD simulation can provide additional insights based on the simulated flow field to interpret the experimental results. However, there is no common way to discuss and study yarn splicing due to the diverse geometry of splicing chambers and the variety of the yarns to be spliced. This is the reason why in the previous studies a specific splicing chamber with specific yarns has been studied and discussed.

The geometry of the splicing chamber, the air jet pressure and velocity and the duration of the air injection must be chosen carefully to result in yarn splicing with good quality. The shape of the splicing chamber must be designed to drive the air flow creating the flow pattern needed for the splicing goal (e.g. create vortices according to Wang et al. [73] and Wu et al. [74]). The air jet pressure and velocity should be appropriate to create sufficient aerodynamic forces, but when they become excessive the appearance and the quality of the yarn will be influenced [75].

4.2 Objective

The basis of this work is an experimental study on ends-together yarn splicing chambers without untwisting stage. That study was conducted by De Meulemeester et al. [76]. In that work, it was shown that chamber size is important to obtain good splices, as well as the symmetry of the chamber and the cutting position (length along which the vortices can act). Inlet pressures above a certain threshold did not influence the splices much. The goal is to use CFD to obtain insights into why these experimental conclusions are obtained. No previous studies of CFD on ends-together splice chambers are available.

The numerical simulations of the air flow have been performed in four selected ends-together splicing chamber geometries with two inlet pressures. The simulations are carried out in empty chambers, without yarn ends being present in the chambers. The effect of the air pressure and the effect of the geometry of the splicing chambers are investigated. Furthermore, the air flow characteristics are used to interpret the experimental results obtained with these four chambers.

4.3 Simulation setup

4.3.1 Chamber geometries

Figure 4.1 (top) shows the different geometries of the chambers and the corresponding air volume within the chambers (bottom). The air volume consists of two parts: the air inlet channel and the splicing part. The air inlet channel is the cylindrical part. The splicing part consists of the union of the V shape with the half cylinder.

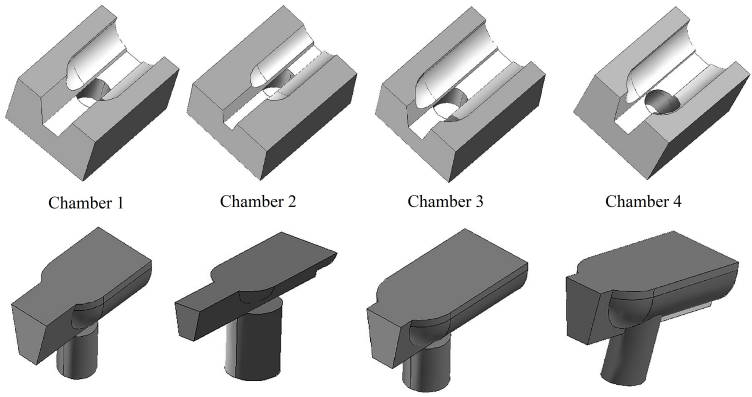

Figure 4.1: The geometry of the chambers (top) and corresponding air volume inside the different chambers (bottom).

Figure 4.2 shows 2D views of the CFD geometry for one of the chambers with indications of the important dimensions. The axis of the air inlet channel is parallel to

the y axis in chambers 1, 2, and 3, whereas it makes a 10^o angle with the y axis or the xy-plane in chamber 4.

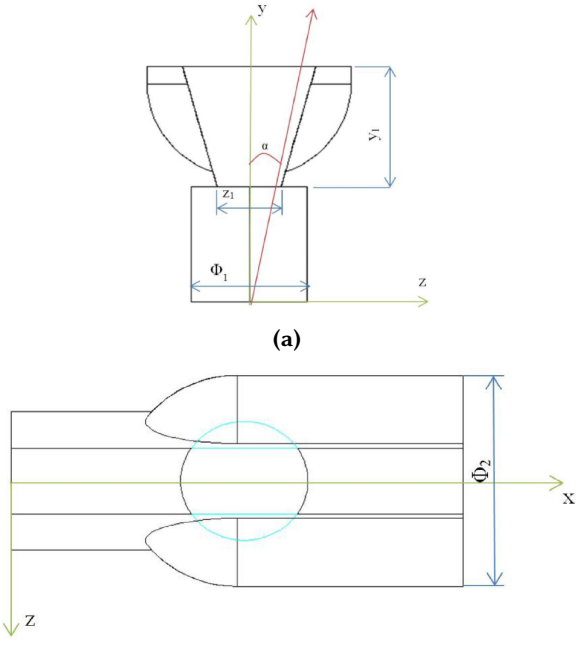

Figure 4.2: 2D views with geometrical characteristics of the chambers: (a) Side view; (b) Top view.

Table 4.1 represents the indicated dimensions of the four chambers. All chambers have the same length and height $X = 16mm$ and $Y = 10mm$. Φ_1 represents the diameter of the inlet channel, the location of the inlet channel is made to be in the middle of chambers 1 and 2 while it is shifted to the left in chambers 3 and 4; y_1 is the height of the splicing part; z_1 is the width of the base of the V shape and its angle is equal for the fours chambers; Φ_2 is the diameter of the half cylinder, α is the angle between the y axis and the axis of the inlet channel.

Table 4.1: Dimensions of the different geometries (mm except for the last column in degrees).

Geometrical characteristics	Φ_1	y_1	z_1	Φ_2	α^o
Chamber 1	4.5	5.1	2.5	8	0
Chamber 2	4.5	3.6	1.5	5.8	0
Chamber 3	4.5	5.1	2.5	8	0
Chamber 4	4	5.1	2.5	8	10

It can be seen from Table 4.1 that chambers 1, 2 and 3 have the same inlet channel

diameter, whereas it is smaller in chamber 4. The intersection between the V shape and the half cylinder is determined by the location of the air inlet channel. In chambers 1, 2 and 3 the diameter of the half cylinder and the height of the inlet channel are dependent on each other as the height of the chambers is fixed to fit in an automated splice cover. This means that an increase in height of the cylindrical inlet part indicates a decrease in cylinder diameter of the splicing part, like in chamber 2. Chamber 4 is made so that the splicing part's dimensions are as for chamber 3, with different inlet channel diameter and location. The main geometrical differences between the four chambers are as follows: chamber 2 is the smallest chamber, chamber 1 and 3 have a different air inlet channel location, while chamber 4 is asymmetrical. The yarn ends are superimposed into the chamber (ends-together) when they are inserted for splicing. They are fixed at the side towards the V part (left part of a chamber in Figure 4.1) and they are free at the other side (right side). The distance between the air inlet channel and the chamber exit (right side) is almost the same in chamber 3 and chamber 4, while it is shorter in chamber 1 and chamber 2 by about *2 mm*. This distance is important and it can be considered as the region where the splicing process occurs.

4.3.2 Air flow simulation model

The air flow which is used for yarn splicing is highly turbulent (the Reynolds number is in the order of 10^5 based on the vent hole width). Therefore, a turbulence model must be used to handle the effects of turbulence in the flow field. In this work Large Eddy Simulation (LES) has been used as turbulence model. The numerical solutions were obtained using Ansys Fluent 14.5. The coupled scheme is used as solution method for pressure and velocity. The second-order upwind scheme is used for the density and energy and the bounded central differencing method is used for the momentum. The least squares cell based method is used for the gradients. The second-order implicit scheme is used for the time discretization.

4.3.3 Air flow domain and grid sensitivity

The domain of calculation, in addition to a chamber, is extended sufficiently in the three dimensions as shown in Figure 4.3. The mostly block structured meshes are created using Gambit (Ansys Inc.). The white unmeshed regions in the grid in Figure 4.3 represent the external wall of the chamber and the lid (the cover).

The mesh is created to have the same step size inside a chamber in the three directions ($\Delta x = \Delta y = \Delta z$). Outside of a chamber, the mesh is gradually stretched. A mesh sensitivity study has been performed to make sure that the results of the simulations are independent of the mesh. The mesh sensitivity is carried out with chamber 2 with inlet pressure 10 bar. Three mesh levels are tested. The total number of cells in the three levels are 1.5, 2.5 and 4 million (grid 1, grid 2, and grid 3 respectively). To test the mesh sensitivity, the average velocities in planes parallel to the yz-plane are plotted in Figure 4.4 where x ranges from 0 mm to 16 mm with step size equal to 1 mm. This means that for each of these planes which correspond to an x value (0:1:16 mm) the average velocity is compared in the different meshes.

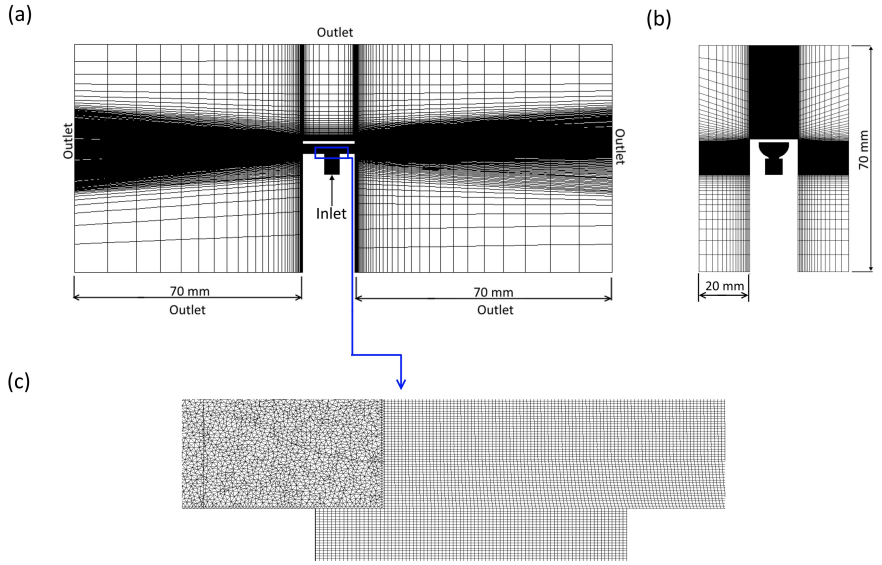

Figure 4.3: The flow grid: (a) the complete domain in xy-plane; (b) the complete domain in yz-plane; (c) close view of the grid inside a chamber.

From Figure 4.4 it can be seen that the differences between grid 2 compared to grid 1 are bigger than grid 3 compared to grid 2. Although the errors between grid 3 and grid 2 are small, the characteristics of grid 3 are chosen to carry out the simulations as there is no comparison in literature. Adopting a finer grid than grid 3 would increase highly the cost of the simulations. Moreover, it is difficult to obtain a LES which is completely independent of the mesh. Therefore, the characteristics of grid 3 are sufficient to have accurate results with acceptable cost. The same mesh characteristics of grid 3 are used to carry out the simulations for the four chambers.

4.3.4 Boundary conditions

Two conditions of the inlet pressure were tested: 10 bar and 15 bar (relative to the atmospheric pressure). The outlet condition is static pressure for outflow and total pressure in case a reversed flow would occur at the outlet and the value is equal to the atmospheric pressure. The initial conditions are: the velocities are zero everywhere, the pressure is equal to 10 bar or 15 bar in the inlet channel and atmospheric pressure elsewhere. The time step is equal to 5×10^{-6} seconds. In experiments, the splicing time is also important and typically it is some seconds. As no yarn is present in the simulations, the total time of one simulation is chosen to give a statistically steady flow field. This takes typically 75 milliseconds.

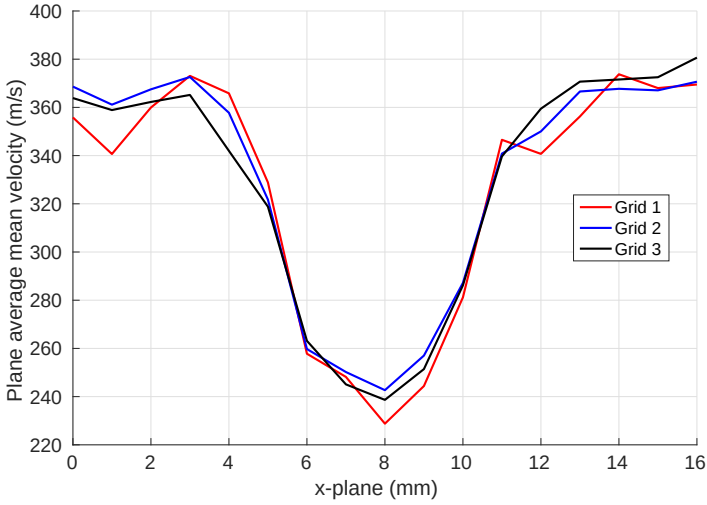

Figure 4.4: Grid sensitivity: (Vertical axis) the average mean velocity magnitude in a plane parallel to the yz-plane; (Horizontal axis) the x-coordinate of this yz-plane: x=0:1:16 mm; (grid 1) the coarsest grid; (grid 3) the finest grid.

4.4 CFD results

For each chamber, inlet pressure 10 bar and 15 bar have been simulated. It has been observed that the conclusions regarding the effect of the inlet pressure are the same for all chambers. Therefore, chamber 1 is chosen to represent the effect of the inlet pressure. Inlet pressure 10 bar is chosen to investigate the effect of the splicing chamber geometry.

The results of the flow field will be presented in three planes, as shown in Figure 4.5. First, the results in the chambers 1, 2 and 3 will be presented and compared. Then the results in the chamber 4 will be presented separately.

Figure 4.6 shows the contours of the mean velocity magnitude in plane 1 for the different inlet pressures for chamber 1 and for the inlet pressure of 10 bar for chambers 2 and 3. The air flow passes from the inlet channel to the splicing chamber through the vent hole, an orifice determined by the intersection between the two parts. It is known that when the flow passes through an orifice and if the ratio of the total pressure upstream over the static pressure downstream is equal to or higher than 1.89, the flow is choked. This means that the flow passes through the throat section with a velocity equal to the acoustic speed. This happens for all three chambers 1, 2 and 3. Behind the throat section, the air flow continues to expand inside the splicing chamber forming an underexpanded jet which eventually runs into a normal shock. When the flow reaches the wall of the lid, it divides in both directions. With the inlet pressure equal to 15 bar the flow expands to higher velocity than with the inlet pressure equal to 10 bar, but only when the flow reaches the atmosphere. Therefore,

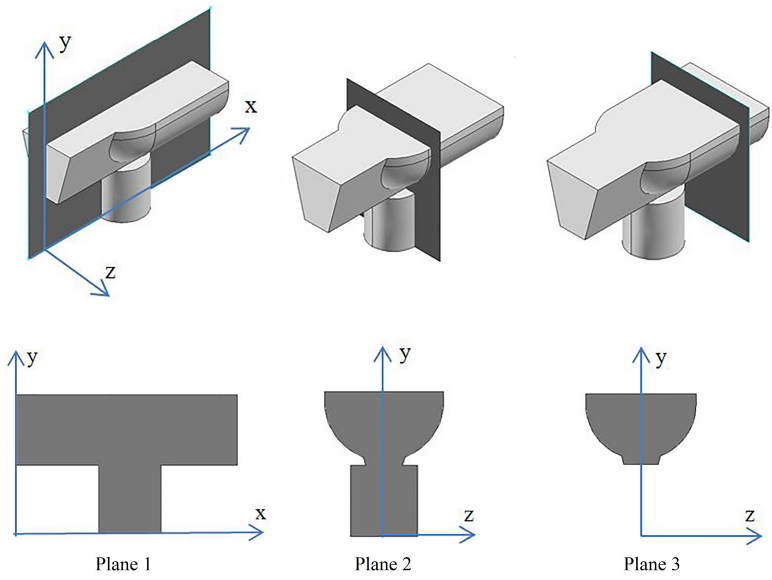

Figure 4.5: Definition of the 3 cut-planes: plane 1 corresponds to the xy-plane, which is the symmetry plane, planes 2 and 3 are parallel planes to the yz-plane, where x corresponds to the location of the air inlet channel center for plane 2, and x=13mm for plane 3, with the origin as indicated plane 1.

we can conclude from Figure 4.6(a) and (b) that the inlet pressure does not affect the flow pattern inside the splicing chamber. Of course it influences the mass flow rate (45% higher for the inlet pressure equal to 15 bar) and the forces that can be executed on the yarn by the air jet, since the density of the fluid will be higher with the higher inlet pressure.

The geometrical effects on the flow field with inlet pressure 10 bar can be seen in Figure 4.6(b) to (d). It can be seen in Figure 4.6(b) and (d) that the region of the jet flow for both chambers shows not much differences. The air flow is totally expanded inside the chamber 3 (see Figure 4.6(d)). It is seen that the values of the velocity are higher inside the chamber than outside in Figure 4.6(b) and (d). The mean velocity magnitude in Figure 4.6(c) for chamber 2 (the smallest chamber) shows that the flow did not expand sufficiently as in the other chambers due to the smaller height of the splicing part. The maximum values of the mean velocity are outside of chamber 2, in the ambient air.

Above considerations show that one should not expect large changes in splicing strength when increasing the pressure above 10 bar. By contrast, smaller chambers or shorter chambers result in maximal velocity outside instead of inside the chamber, suggesting that yarns will need to be cut longer to undergo the same effects. Apart from this, a really small chamber like chamber 2 has less zones with high mean velocity. It can be concluded that specific features of splice chambers are visible in the CFD analysis, but not yet how splicing can happen at all. For this we consider

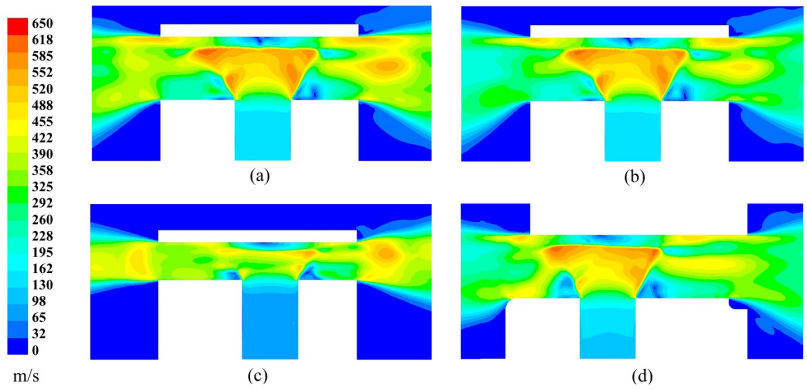

Figure 4.6: Contours of mean velocity magnitude in plane 1: (a) chamber 1, 15 bar; (b) chamber 1, 10 bar; (c) chamber 2, 10 bar; (d) chamber 3, 10 bar.

flow directions.

Vortices are a major component of the turbulent flow. They have been identified to play a crucial role in ends-opposed yarn splicing, and we assume that to be the case also in the ends-together splice chambers. The vortices apparently make the yarn fibers intermingle together. The geometry of a splicing chamber has a big impact on the formation of these vortices. To demonstrate the created vortices in this type of chambers, chamber 3 is chosen. Figure 4.7 shows velocity vectors in chamber 3 with inlet pressure equal to 10 bar, Figure 4.7(a) and (c) show the mean velocity vectors in planes 2 and 3 respectively, Figure 4.7(b) and (d) show instantaneous velocity vectors, at the last time step of the simulation, in the same planes.

The velocity vectors represent the directions and the magnitude of the flow velocity. It can be seen from Figure 4.7(a) that when the jet flow reaches the lid, it divides into two directions forming two contra-rotating vortices. Figure 4.7(b) shows that the essential changes in the directions and the values of the velocity vectors occur in the regions of intersections between the vortices and the jet flow and in the center of the vortices (right and left of the jet flow). Figure 4.7(c) shows that the mean flow is symmetrical with regard to the middle of the shown plane. Moreover, the mean flow consists mainly of two vortices. Each vortex occupies half of the shown plane. However, the instantaneous velocity vectors shown in Figure 4.7(d) indicate that the flow is unsteady, there is a strong interaction between the two vortices. This interaction takes place in the middle of the shown plane. Close to the chamber's wall, the flow moves parallel to the wall. At the bottom of the chamber, the flow changes direction going upwards. This implies that the flow in the middle of the chamber oscillates to the left and the right. The most important is that the two vortices are always seen or present. We believe that these rapid changes are a requirement for splicing, allowing the mixing of yarn ends trapped in the left or right vortex.

In videos, it is clearly seen that the borders of the jet flow shown in Figure 4.7(b) and the flow in the middle of plane 3 shown in Figure 4.7(d) oscillate. Many factors can

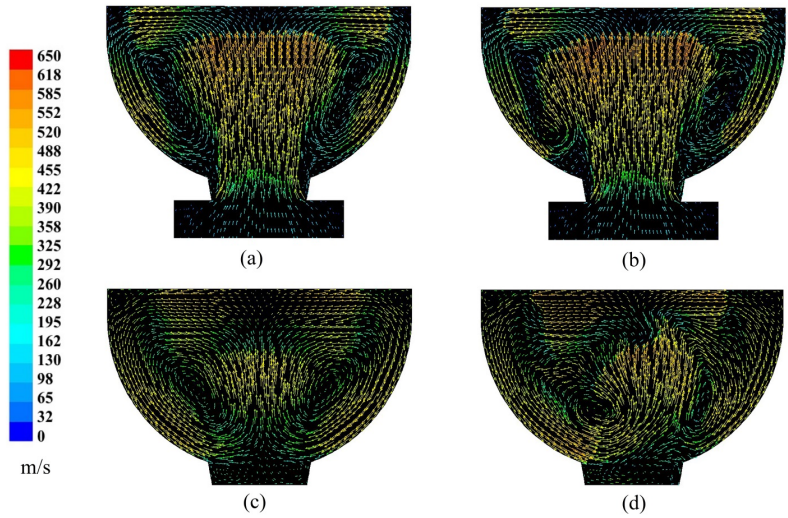

Figure 4.7: Illustration of velocity vectors in chamber 3: (a) mean velocity vectors in plane 2, (b) instantaneous velocity vectors in plane 2, (c) mean velocity vectors in plane 3, (d) instantaneous velocity vectors in plane 3.

make the flow oscillate. First, the case of the flow inside a splicing chamber may be a fluidics case. Fluidics or fluidic logic is the use of a fluid to perform analog or digital operations without any moving parts. However, the flow in a fluidics case switches completely from left to right, while in the studied splicing chambers, the flow oscillates, but not completely from left to right. Second, the two vortices seen in Figures 4.7(b) and (d) are unstable. These vortices are of large scales. This means that there are flow oscillations due to unsteadiness of large scales. Third, the jet flow shown in Figure 4.7(b) is turbulent. Thus, the flow may oscillate due to the instabilities of the shear layer which eventually run into turbulence. This means that there are flow oscillations due to turbulence effects. It is not clear to conclude which factor is dominant and contributes most to flow oscillations. By consequence, the flow in the studied splicing chambers is unsteady and the unsteadiness of the flow may be caused by the three factors mentioned above.

The root mean square values of the velocity (RMS) are commonly used to characterize the amount of turbulence in a flow. It represents the deviations of the velocity from the mean values. For an unsteady flow like the flow in the studied splicing chambers, the velocity deviates from the mean value due to two effects: turbulence and flow oscillations. The RMS provides an interesting insight regarding the splicing process in each chamber due to flow unsteadiness, bringing forward the unsteady zones with the most violently changing velocities. Mathematically, the root mean square of velocity is calculated as follows: $\mathrm{RMS}\,(V) = \sqrt{\mathrm{mean}\,(V^2) - (\mathrm{mean}\,(V))^2}$ where mean refers to time averaging at a certain fixed point. In Fröhlich et al. [77] the RMS of the velocity is used in many simulation results to highlight the velocity fluctuations, or the velocity deviations from the

mean values, and to compare RMS values of LES and DNS (an example is shown in Fröhlich et al. [77] page 417).

Figure 4.8 shows the contours of the root mean square (RMS) of the velocity magnitude in plane 3 for the different chambers for an inlet pressure equal to 10 and 15 bar for chamber 1 and 10 bar for the other chambers. For the three chambers, the highest RMS values are located in the middle of each chamber, where the flow is changing most as has been shown already in Figure 4.7. The RMS values in chamber 1 show no significant difference for the inlet pressure equal to 10 and 15 bar. The bigger geometries of chambers 1 and 3 allow higher fluctuations than the small geometry of chamber 2. In chamber 3, the RMS values close to the wall of the chamber are somewhat higher than in chamber 1. The different pattern of the RMS contours between chambers 1 and 3 is due to the shifted position of the vent hole, as is shown in Figure 4.6. We can assume that one yarn, or part of a yarn, is trapped in one vortex, and the rest in the other, with the region with high fluctuations allowing transfer of fiber strands from one vortex to the other. Transfer can only happen after a yarn has been sufficiently untwisted, after which retwisting (splicing) can occur due to this chaotic nature of the air flow.

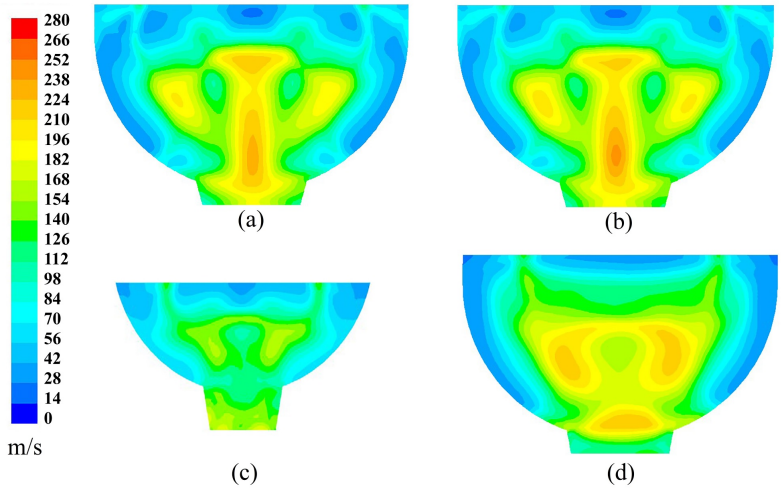

Figure 4.8: Contours of RMS of velocity magnitude in plane 3: (a) chamber 1, 15 bar; (b) chamber 1, 10 bar; (c) chamber 2, 10 bar; (d) chamber 3, 10 bar.

Chambers 1, 2 and 3 are symmetrical geometries and the results presented above show that these symmetrical geometries give almost symmetrical mean flow inside the chambers, which agrees with our expectations. Conversely, chamber 4 is asymmetrical, thus it is expected to give asymmetrical mean flow inside it. It is worth to investigate how much the asymmetrical mean flow will affect the yarn splicing. Figure 4.9 shows the contours of the mean velocity magnitude and the instantaneous velocity vectors with inlet pressure 10 bar in the plane 3. Figure 9(a) shows that the flow inside chamber 4 is indeed asymmetrical as there are high differences in the values of the mean velocity magnitude inside the chamber. In Figure 4.9(a) we see a region with low velocity and another with high velocity. From Figure 4.9(b), it can

be seen that, there is no clear formation of two big vortices as in chamber 3. Instead there are rather many vortices. One vortex is seen on the right side of the shown plane, but on the left side, there are many small vortices.

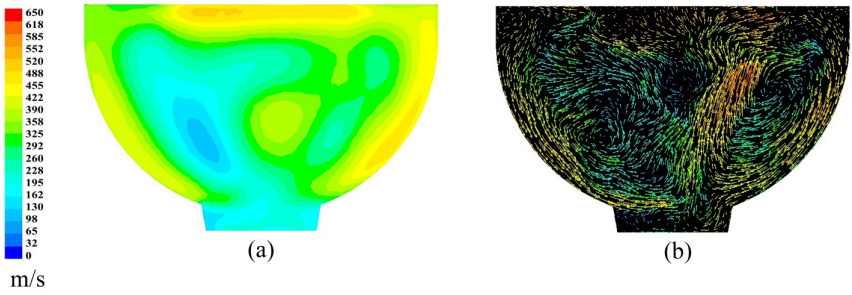

Figure 4.9: Contours of mean velocity magnitude and velocity vectors in chamber 4: (a) contours of mean velocity magnitude in plane 3; (b) instantaneous velocity vectors in plane 3.

4.5 Experimental method

4.5.1 Experimental setup

The splice chambers used in the CFD study presented above were 3D printed and tested on a splicing machine, as described in De Meulemeester et al. [76]. The splicing machine can be used at pressures from 5 to 15 bar with splice duration from 10 ms to 5000 ms and has a fixed scissors position. The setup is given in Figure 4.10. It should be noted that there is a tube between the pressure vessel and the valve, which should be eliminated to avoid pressure oscillations in the nozzle. Tests were done at 10 and 15 bar and a duration of 1000 ms. Above a splicing duration of 250 milliseconds, splicing duration has little influence on splice strength and was hence not varied. To show the influence of the jet leaving the splice chamber, the cutting length was varied by cutting the yarns at the standard position or at the chamber exit and then manually moving the scissors to cut the yarns towards or away from the chamber exit in steps of 1.5 mm.

As yarn we selected a common yarn used in tapestry splicing machines: a yarn consisting out of 3 ring spun strands of about 250 tex each, with a resulting composed tex number of 751.4 tex. The twist of the strands is 248 tpm, the twine is 147 tpm and the material is polyamide + wool. The strength of this yarn is 55.7 N with a standard deviation of 5.0 N, as tested on a Textechno Statimat M tensile tester. The yarn diameter is 2mm with porosity approximately equal to 40%. Depending on the application, different evaluations are possible of the resulting splices. In tapestry applications, the splice is normally not visible and one is only interested in the

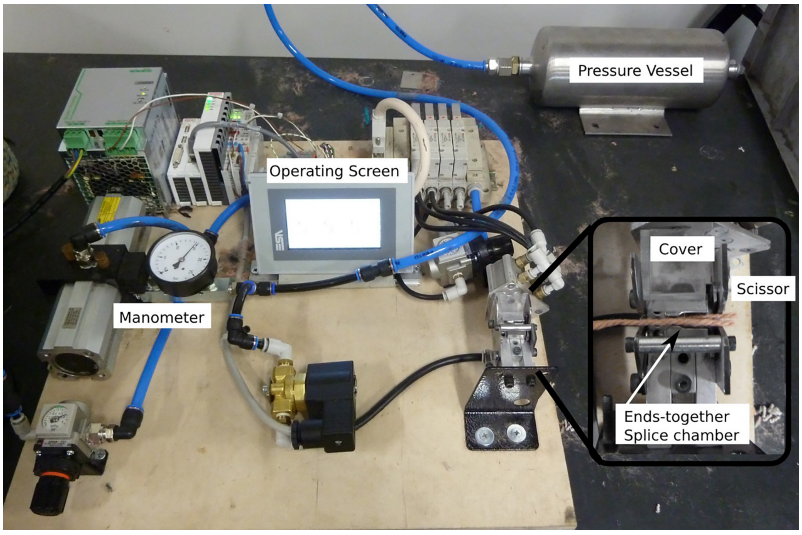

Figure 4.10: Experimental setup, with inset showing the ends-together splice chamber with cover and scissors.

resulting strength of the splice, which should be sufficiently high to allow weaving. The value of interest is then the retained splice strength RSS, defined as

$$\mathrm{RSS} = \frac{\text{Tensile strength post splice}}{\text{Mean tensile strength single not spliced yarn}} \tag{4.1}$$

From a production point of view, the RSS should be as high as possible, as that offers the best guarantee that the yarn will not break during the weaving process. In an industrial tapestry setting a tensile strength test of 20 N after the splicing is common to test if the splice is good or should be redone.

We start with comparing the 4 chambers at inlet pressure 10 bar and 15 bar for this yarn. We also evaluate the chambers at different cutting lengths of the yarn. We consider the default position of the scissors as 0 mm and investigate an additional splice length of +1.5 mm and +3.0 mm.

4.5.2 Experimental results

The resulting average splice strength of 20 samples as described in De Meulemeester et al. [76] is listed in Tables 4.2 and 4.3.

In spite of a low splice strength for chamber 1 at the standard cutting position with inlet pressure 15 bar, we observe the lowest strength for chamber 2. One possible reason for this may be due to the small size of splice chamber 2 relative to the yarn. The yarn has little space to move and friction of the yarn with the walls of the splice chamber is consequently a lot higher. The strength changes with changing the

Table 4.2: Splice strength in N at 10 bar.

Splice length	0 [mm]	CV%	+1.5 [mm]	CV%	+3.0 mm	CV%
Chamber 1	18.7	52	25.9	35	26.2	24
Chamber 2	13.5	46	20.0	20	19.3	24
Chamber 3	29.5	15	25.3	22	25.6	24
Chamber 4	0		0		0	

Table 4.3: Splice strength in N at 15 bar.

Splice length	0 [mm]	CV%	+1.5 [mm]	CV%	+3.0 [mm]	CV%
Chamber 1	18.4	55	29.9	21	30.1	21
Chamber 2	24.3	23	22.1	23	24.4	16
Chamber 3	33.1	11	30.4	17	27.3	22
Chamber 4	0		0		0	

cutting position: with inlet pressure 10 bar it increases at 1.5 mm and then decreases at 3 mm, while the contrary happens with inlet pressure 15 bar.

For chamber 1 with the standard cutting position of the scissors we observe a dramatically lower strength. This is due to the small length of yarn ends extending past the splice hole. During splicing, the yarn ends twist around each other, shortening the yarn length to the right of the splice hole, while the yarn length to the left remains the same. This often leads to premature ejection of the splice through the yarn entry hole to the left during the splicing process, ejecting the splice before it has reached proper strength. Apart from this lower strength value for chamber 1 at the standard cutting position we observe a higher strength than for chamber 2 because the chamber is also larger and allows easier movement of the yarn within the splice chamber during splicing. The strength increases by extending the cutting position to 1.5 mm and 3 mm behind the standard cutting position, with only a small increase from 1.5 mm to 3 mm. This is explained in the following section.

For chamber 3 we observed the highest strength at the standard cutting position. The reason for this is the larger length of the splice chamber towards the right of the splice hole. This allows more yarn to be contained within the splice chamber during the splicing process. Even when the length of yarn towards the right shortens due to the twisting of the ends around each other, there is still sufficient length such that the yarn is not ejected prematurely out through the yarn inlet hole but remains in the chamber until the splicing process is complete. The splice strength decreases when the cutting position and thus the splice length is increasing.

For chambers 2 and 3 we observed higher strength at inlet pressure 15 bar than at inlet pressure 10 bar, while this is not observed for chamber 1 at the standard cutting length. By extending the cutting position by 1.5 mm or 3 mm we observe higher strength at inlet pressure 15 bar than inlet pressure 10 bar for all chambers. In De Meulemeester et al. [76], it was found that splice strength increases rapidly from zero after a certain minimum pressure, but then often reaches a plateau after which the strength no longer increases. For chamber 1 and 3 the splice strength reached

a maximum at 12 bar, while the splice strength in chamber 2 kept increasing all the way up to the maximum achievable pressure of 15 bar.

With chamber 4 no splices could be made. The idea of an asymmetric entrance hole was to create a more powerful vortex, as rotation of fiber strands around each other is how splices are formed. Although the separate yarns untangle correctly with chamber 4, the fiber strands of the two yarns intermingle too weakly to form good splices.

From the experimental study one can conclude that the splice chamber needs to be large enough to contain the yarn which may allow sufficient motion during the splicing process and that a correct cutting length is important to achieve the maximum splice strength possible for a chamber at a given entry pressure. Instead of changing cutting length, one can also provide a sufficient amount of chamber to the right of the splice hole, which leads here to the strongest splices. Finally, an asymmetric entrance hole as considered here in chamber 4 is not a viable way to construct a splice chamber.

4.6 Discussion

There is no apparent discrepancy in the values of the velocity magnitude inside the chambers, for the inlet pressures of 10 or 15 bar. An inlet pressure higher than 10 bar gives a higher mass flow rate as the density is higher. Moreover, as it has been observed from the values of the root mean square of the velocity magnitude, the two inlet pressures provide the same RMS values, which means that the velocity fluctuations remain constant with both inlet pressures. Therefore, the vortices are identical. By consequence, for this type of chambers, when the inlet pressure is higher than 10 bar, the yarn ends will be subjected to the same air flow pattern with higher aerodynamics forces. The experimental results confirm these observations. It is noticed that the splicing strength increases with increasing the inlet pressure on the standard and extended cutting position. However, it is not always so that higher forces lead to better splicing. There is limit or threshold for the inlet pressure after which there is no increase in the splicing strength or there is even a decrease, as it is shown in the experimental results for chamber 1 at the standard cutting position.

By contrast, the velocity outside of the chambers is higher for higher inlet pressure and this has an effect on the splicing. In some cases, it is observed that the yarn ends are blown out of a chamber, especially when the inlet pressure increases. This means that the aerodynamic forces which act on the yarn ends in that direction are considerable. The aerodynamic forces could not be calculated because the simulation was carried out in empty chambers. We investigate instead the calculated mass flow rate which may account for this phenomenon. It has to be calculated at the left side of the chamber where x=0. For chamber 1, it is higher 45% with inlet pressure 15 bar than with 10 bar. Furthermore, with inlet pressure 10 bar it is 10% higher for chamber 1 than for chamber 3. However, by extending the cutting position at the right side of the chamber, the outer flow gives better splicing strength to some extent. For example, the splicing strength increases with increasing the cutting positions in chamber 1. The flow did not completely expand inside the chamber. When it goes

out of the chamber, it continues expanding to higher velocities. By consequence, the splicing strength is improved.

The expansion of the flow is constrained by the dimensions of the chamber. The bigger geometry of chambers 1 and 3 allows the flow to reach higher velocities inside them than in chamber 2. The CFD analysis shows for chamber 2 lower maximum speeds and lower RMS between the two vortices, which apparently reduces the maximum splice strength that can be obtained at a specific inlet pressure compared to chambers 1 and 3. Moreover in Webb et al. [78] the effect of the cross section (or volume) of the splicing chamber was analyzed by an experimental study. They changed the yarn count to study the influence of the cross section of the splicing chamber. They found that increasing the cross section of a chamber improved the splicing strength, but when the yarn count became too big, increasing the cross section did not improve the splicing strength. Here, in this work, the yarn or the yarn count is the same with all chambers. On the one hand, the effect of the cross section of the chambers with the same inlet pressure can be seen by flow characteristics as mentioned above. On the other hand, with the smallest cross section, chamber 2, the splicing strength improves when increasing the inlet pressure or increasing the cutting position. The numerical and the experimental observations of the smallest cross section effects render difficult to draw a definitive conclusion about whether these effects are related to the geometry of the chamber or related to the flow features. It can be said that both the volume of the chamber compared to the yarn volume and the flow characteristics do influence the splicing quality.

The cylindrical inlet part shifted towards the entrance in chamber 3 leads to a shifted flow field. This results in better splicing because the length of the flow field region that contributes in the splicing is longer and the length of the yarn ends in the splicing region are longer. Moreover, this region can be increased by changing the cutting position for chamber 3, but the splicing strength is lower in this case because the flow will dissipate in the ambient after leaving the chamber and too much yarn is present that needs to be untwisted. It can be seen that chamber 3 has the highest splicing strength compared to the others chambers on the standard cutting position.

The asymmetrical geometry of chamber 4 does not produce splices. This means that there are flow features which do not result in splices. A comparison between chamber 3 and chamber 4 is made to understand and highlight those flow features. Figure 4.11 and 4.12 show the instantaneous velocity vectors inside chamber 3 and 4 in four frames. The frames in Figure 4.11 and 4.12 are chosen at moments where the flow deviates a lot from the mean flow. This means that the times of the frames in Figure 4.11 are not necessarily equal to the times of the frames in Figure 4.12.

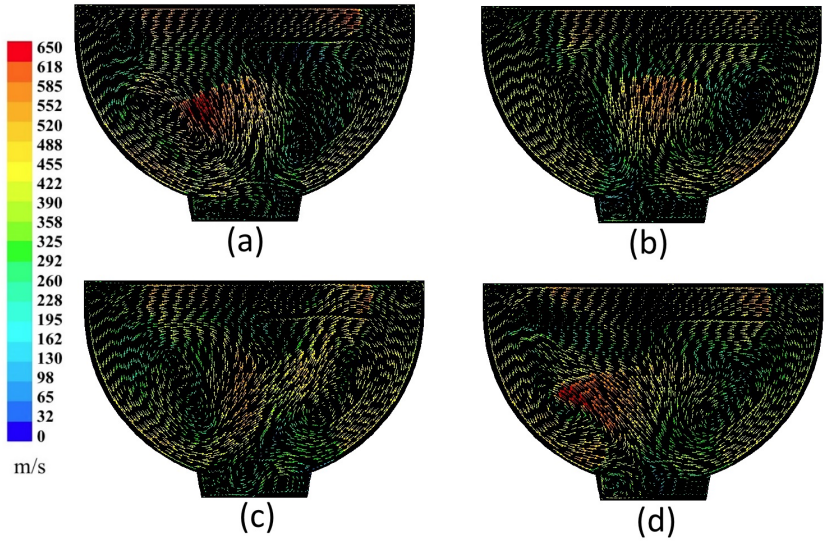

Figure 4.11: Illustration of the instantaneous velocity vectors in chamber 3 in plane 3 at time: (a) t_1; (b) t_1+0.0175ms; (c) t_1+0.103ms; (d) t_1+0.145ms.

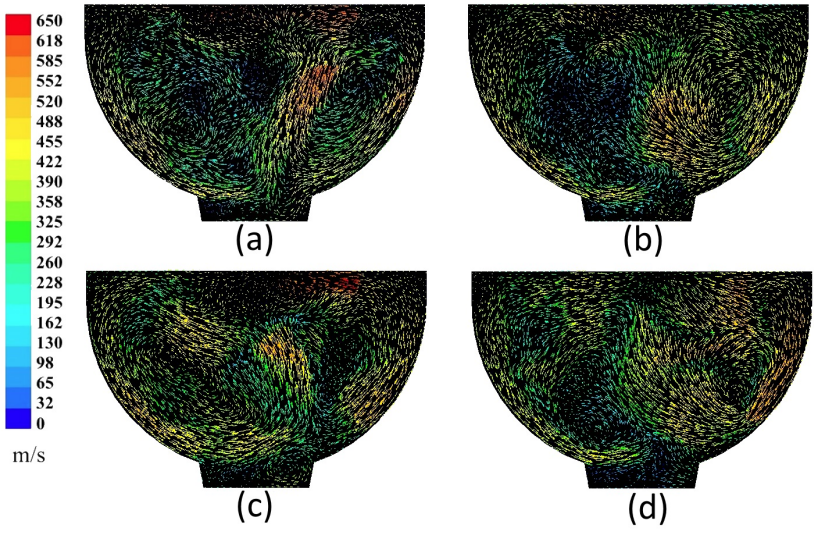

Figure 4.12: Illustration of the instantaneous velocity vectors in chamber 4 in plane 3 at time: (a) t_2; (b) t_2+0.0175ms; (c) t_2+0.10815ms; (d) t_2+0.243ms.

In chamber 3, Figure 4.11 shows that two counter-rotating vortices are seen in the four frames, the flow oscillates in the middle of the chamber where the two vortices interact and the flow close to the chamber's wall does not change that much. In

chamber 4, Figure 4.12(a) and (b) show that one big vortex is seen on the right side of the shown plane, but on the left side there are many smaller vortices. The formation of two big vortices is seen in Figure 4.12(c) and (d). However, Figure 4.9(a) shows that there are high differences in the value of the mean velocity around the middle of the chamber. The experimental results for this chamber show that the flow is able to untwist the yarn ends but not to retwist them in a usable splice. Additionally, it has been seen that the flow is asymmetric with high differences around the middle of the chamber. By consequence, it can be deduced that an important flow feature for splicing process is two strong and big vortices.

Figure 4.13 shows the contours of the RMS of the velocity magnitude in chamber 3 and 4 in plane 3. The RMS values in chamber 4 are as high as in chamber 3, or even higher. However, Figure 4.13 shows that the RMS of the velocity is symmetrical in chamber 3, but in chamber 4, the RMS is not symmetrical. Figure 4.13 confirms the flow patterns seen in Figure 4.11 and 4.12. Therefore, it can be drawn that the oscillations of the flow are not important in the absence of powerful vortices which are able to untwist the yarn ends and splice them.

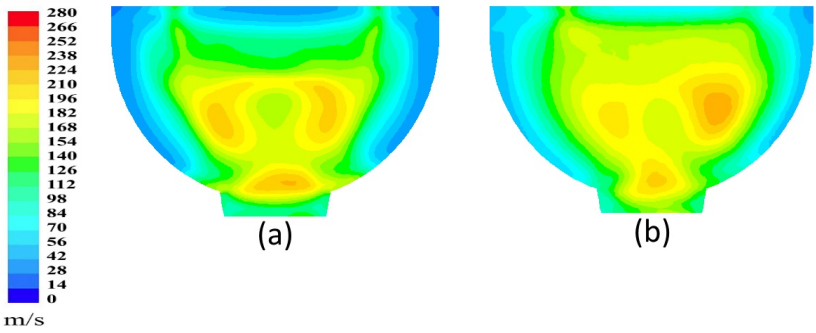

Figure 4.13: Contours of RMS of velocity magnitude in plane 3: (a) chamber 3; (b) chamber 4.

4.7 Conclusion

In this chapter, large-eddy simulations of the flow field in four splicing chambers have been carried out. Based on the numerical and experimental results presented in this chapter, it can be concluded that a splicing chamber will give splicing if it creates the flow field pattern which is needed for splicing purposes: two large counter-rotating vortices and unstable velocity directions at the interface of these counter-rotating vortices. The yarn ends will be subjected to the same flow field with higher aerodynamics forces if a splicing chamber supplied by an inlet pressure higher than 10 bar.

The volume of the splicing chamber plays an essential role in allowing the flow to reach sufficiently high values of velocity, resulting in the necessary aerodynamic forces that can make the yarn ends intermingling together, but these forces may

not guarantee good splicing if the geometry of a splicing chamber does not have sufficient space to let the yarns intermingle together.

The location of vent hole or air inlet channel is important to create sufficient length of the splicing region, which gives better splicing properties. A splicing chamber which is used to splice superimposed yarns should not have excessive amounts of backwards flow (flow towards the left, not in the direction of splicing) because on the one hand, it does not contribute in the splicing of the yarn ends and on the other hand it causes the yarn ends to be blown out of chamber prematurely if it creates high aerodynamic forces.

Increasing the length of the splicing inside the chamber by changing the position of the air inlet chamber is better than increasing it by changing the cutting position.

The values of the root mean square of the velocities represent a new flow factor to evaluate the unsteadiness of the flow inside a splicing chamber. The values of the RMS correspond to regions where the flow is unsteady due to the effects of turbulence or due to oscillations. High values of RMS together with two strong vortices are an indication to obtain good splicing, but only high values of RMS do not indicate to a good or bad flow feature for splicing purpose.

In weaving, knots can be created in the yarn, but this is of course undesired. If one understands how splices are created in a splicing chamber, this insight can also be useful to understand how these knots in a weaving machine can be avoided.

Chapter 5

Optimizing the main nozzle geometry

In this chapter, an optimization procedure for the geometry of main nozzles in weaving machines will be presented. It is based on coupling three tools together: one for geometry and mesh creation, another for air flow simulations and an optimization solver.

After an introduction, the steps and the assumptions which have been considered to perform the optimization are explained. The obtained optimum geometries are then presented and compared with a reference geometry.

5.1 Introduction

An air jet loom (see Figure 1.2) is a weaving machine which uses the air flow to accelerate weft yarns. The air jet loom is widely used in textile industries due to its high productivity and effectiveness. This machine can be used to weave monofilament and spun yarns. The motion of the weft yarn in an air jet loom can be divided into two stages according to the guiding device. The first stage starts with the main nozzle (see Figure 1.2). The main nozzle is supplied with compressed air which expands to high velocities inside and beyond the main nozzle. The air flow exerts aerodynamic forces on the weft yarn. Those forces suck the weft yarn from the prewinder and launch it into the reed where the second stage starts. The relay nozzles guide the weft yarn in the reed where it is woven in. However, the second stage is not considered in this chapter.

The productivity of the air jet loom is related to the insertion time. The insertion time decreases if the speed of the yarn increases and then the productivity increases as well. The speed of the weft yarn cannot be increased indefinitely by increasing the amount of compressed air due to the consumption of air [79] and the resultant high tension on the weft yarn [80]. High air consumption increases the weaving cost, for the compressor and electricity, and the weft yarn may break under high tension.

However, if the high tension is not the limiting factor, the speed of the weft yarn can be increased by optimizing the geometry of the main nozzle to generate the highest aerodynamic forces under a specific inlet air flow rate. This means less air consumption for the same forces and speed.

The principal objective of optimizing the geometry of the main nozzle is to find the optimum geometry which gives the best air flow. The previous related research achieved this objective by changing either geometrical properties of the main nozzle, dimension or shape, or air flow inlet conditions. Figure 5.1 shows the structure of the main nozzle with indications of the most important regions or parts.

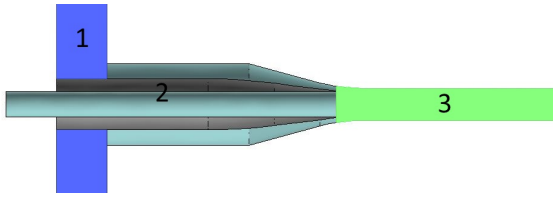

Figure 5.1: Simplified representation of the main nozzle structure: (1) Compressed air supplier; (2) Needle (internal edges) and nozzle body (external edges); (3) Tube.

Analysis of the air flow inside the geometry of the main nozzle started early in the mid of the previous century. However, the first attempts to optimize the geometry of the main nozzle were only based on experiments and simplified equations. Uno et al. [81] and later Uno [82–84] studied the effects of the main nozzle shape and dimensions on the speed of the weft yarn. Mohamed and Salama [85] investigated the performance of another main nozzle geometry which looked like a modern main nozzle. Ishida and Okajima[86, 87] conducted two series of experiments to investigate the effects of tank pressure and tube length on the performance of a main nozzle. They reported the importance of the effects of the needle tip on the air flow inside main nozzles. The previously mentioned works paved the way for developing the shape of the main nozzle and determining the influential geometrical factors like the tube length and diameter and the needle tip.

Oh et al [88] showed that the recirculation region after a rounded needle tip is shorter than the one after a squared tip. Therefore, the longer region results in high loss of total pressure. The effects of the shape and the dimensions of the needle were studied by Prabkeao and Aoki [89]. They carried out experiments to investigate the flow pattern and characteristics with changing needle. They performed the study with seven needle models and tank pressure ranges from 2 to 6 kgf/cm^2 (196133 to 588399 Pa). No clear conclusion was stated in their works with regard to the needle shape. However, the shortest needle with the highest tip diameter gave the best performance amongst the others.

Some works were conducted to investigate the flow fields with specific geometries of the main nozzle [90, 91]. These works discussed generally the flow fields inside main nozzles. The aerodynamic forces on the weft yarn increase with increasing tube length [92]. However, by increasing the tube length, the pressure loss increases due to friction with the wall of the tube. Therefore the inlet pressure has to increase.

Few attempts have been made or published which used the powerful tools of CFD and computing resources to optimize the geometry of the main nozzle. Belforte et al. [93] studied two geometries of a main nozzle. The shapes of the geometries are the same but the dimensions are different. They found that an increase of the tube length increased the forces but it reduced the suction capability of the nozzle. Moreover, they stated that the divergent tube was better than the cylindrical one. Chen et al. [94] proposed a new design of main nozzle. The new design consisted of two needles connected in series. The goal of the new design was to decrease the effects of turbulence and the reversed flow. Although the new suggested design had a reverse flow, its performance was better than the common design (one needle). Jin et al. [95] optimized the structure of the main nozzle based on CFD. The optimum structure had different internal diameters in comparison with the basic or common one. The optimum structure improved the velocity inside the nozzle along the tube but it generated more turbulence.

All works mentioned above attempted to optimize the geometry of the main nozzle by different ways. However, these works were based on predefined dimensions of the potential optimum geometry. This means that the performance of the optimum geometry in those works was relatively better than others but it was not the absolute optimum geometry. In this work a new procedure to find the optimum geometry of the main nozzle is proposed. The basic idea of this procedure is to describe the geometry of the main nozzle with parameters. Therefore, an optimization solver can be employed to find the optimum geometry by changing freely these parameters. This procedure will be explained in detail.

5.2 Optimization setup

The speed of the weft yarn increases by increasing the axial aerodynamic force generated inside the main nozzle. Thus, the objective of the optimization is to find the geometry of the main nozzle which gives the highest axial aerodynamic force.

5.2.1 Structural simplifications and geometry decomposition

The geometry of the studied nozzle consists of a needle, a nozzle body and a tube, like the basic or common one used with weaving machines (Figure 5.1). The shape of the needle, the nozzle body and the tube are axisymmetric. It is expected that the optimization solver will test hundreds of geometries. Moreover, the objective of the optimization solver is the aerodynamic force which means that one air flow simulation has to be performed with each geometry. Although the three-dimensional air flow simulation could be done, this would cost a lot of time to perform the optimization. By representing the weft yarn as a uniform cylinder along the axis of the main nozzle, a two-dimensional axisymmetric air flow simulation can be chosen during the optimization.

The needle, the nozzle body and the tube of the main nozzle are decomposed separately into a set of segments (2D representation). The points of the segments

are determined mathematically. Thus, a parametric description of the geometry is obtained. By changing these parameters, the coordinates of the points change and thus also the segments and the resultant geometry. Figure 5.2 shows the geometry of the main nozzle in a two-dimensional axisymmetric representation. D_1 is the yarn inlet diameter and D_2 the external needle diameter. R and α are a radius and an angle of an arc which belongs to the needle or the nozzle body. D_7 and D_9 are the tube inlet and exit diameters. D_8 is the diameter of the needle tip. L_2 is the total length of the nozzle.

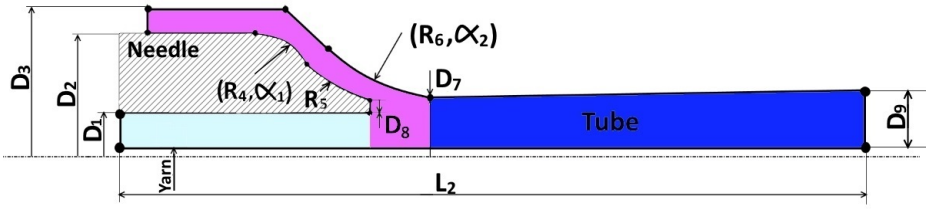

Figure 5.2: Two-dimensional axisymmetric representation of the geometry of the main nozzle, the three colored regions depict the tube, the needle and the nozzle body.

A set of 15 parameters, in total, determines the coordinates of the shown points or segments. Each point's coordinate is either explicitly determined or calculated by solving a system of equations.

5.2.2 Fluid domain and boundary conditions

The two-dimensional axisymmetric fluid domain consists of the nozzle geometry (Figure 5.2) and two extra regions on the left and the right as it is shown in Figure 5.3. The two extra regions which are colored in red are added to take into account the effects of the outer flow. The cylinder wall represents the weft yarn.

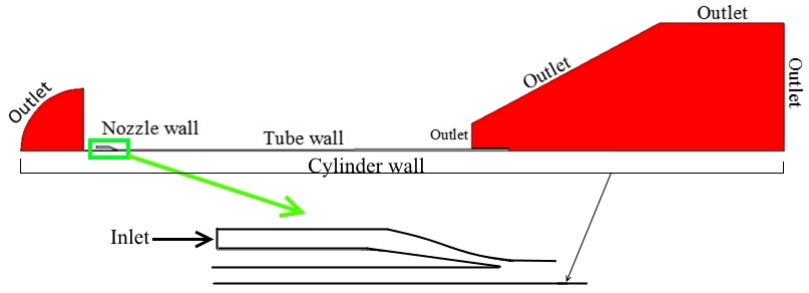

Figure 5.3: Fluid domain with the boundary conditions.

The boundary conditions are set as follows. At the inlet, the static pressure equals 5 bar relative to the atmospheric one. At the outlet, the static pressure equals the

atmospheric one. The nozzle wall and tube wall are no-slip stationary walls. The cylinder wall is a no-slip wall moving at a given speed.

The compressible, turbulent and steady air flow simulations have been performed with the k-ω SST turbulence model. The relative convergence tolerance of the flow quantities is set to 10^{-6}.

The grid of the fluid domain is created based on two factors which are the accuracy of the simulations and the computational time. As the optimization is based on air flow simulations, the computational time of one simulation is very important. To validate the grid and the results of the simulations, grid convergence studies have been performed and the results have been compared to experimental results. The experiment was carried out to measure the pressure inside a main nozzle. The pressure was measured with a probe on the centerline and with pressure taps on the tube wall. The results are independent of the grid and the results agree with the experimental data.

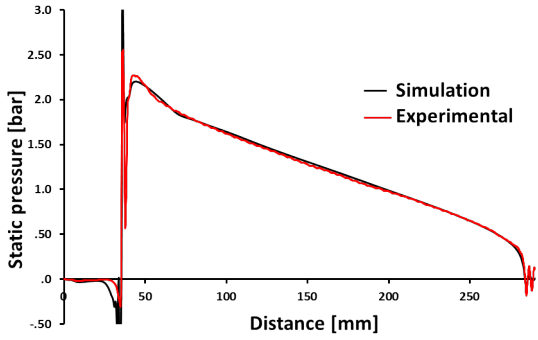

Figure 5.4: Grid validation. Pressure along the probe on the centerline of the main nozzle.

Figure 5.4 shows a comparison between the experimental data and simulation results. The differences between the results of the simulation and the experimental data are small except at x=30 to 40 mm with the origin located at the yarn inlet. The high differences are seen at an axial distance (30 to 40 mm) where there is reverse flow, flow expansions and shocks, as will be shown later. However, the differences occur at small distance and reducing these differences implies increasing the resolution of the grid in this region, which increases the computational time of the overall optimization. Therefore, the grid characteristics whose results are shown in Figure 5.4 are fixed to perform the optimization. The grid is structured as shown in Figure 5.5 and the total number of cells is about 30 000.

5.2.3 Fixing the mass flow rate

The axial aerodynamic force on the weft yarn depends on the inlet mass flow rate. Increasing the inlet mass flow rate increases the axial force. Therefore, effective optimization of the geometry implies fixing the inlet mass flow rate. With an inlet

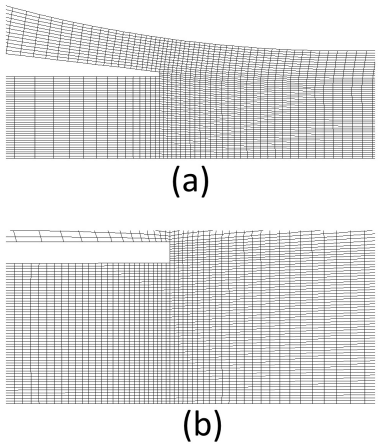

Figure 5.5: Parts of the grid: (a) Around the needle tip; (b) Around the tube exit.

pressure of 5 bar the main nozzle is always choked. Figure 5.6 shows contours of the Mach number for a typical main nozzle. The throat section which is highlighted in Figure 5.6 can be used to adjust the mass flow rate. Increasing or decreasing the area of the throat increases or decreases the inlet mass flow rate.

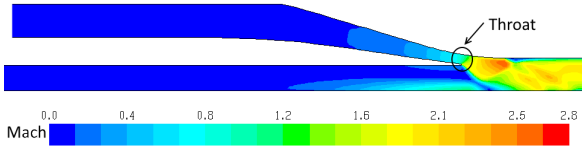

Figure 5.6: Contours of Mach number with a typical main nozzle.

Figure 5.7 shows how the mass flow rate is adjusted. The highlighted segments in black color are axially shifted to the left (blue points) or to the right (red points).

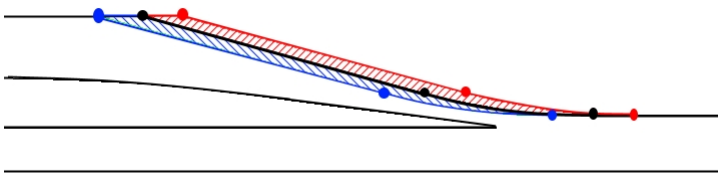

Figure 5.7: Adjusting the throat area. The highlighted segments in black are axially shifted to the left (blue segments) or to the right (red segments).

The mass flow rate is verified to change almost linearly with the modified axial distance. This implies $\Delta\dot{m} = a \triangle x$ with a a constant which is determined by performing several simulations with different Δx. Therefore, during each optimization iteration, the first simulation is performed and the mass flow rate is obtained. The

obtained value has to be equal to a given value. Thus, according to the equation mentioned above, the axial coordinates of the three highlighted segments or points in Figure 5.7 are increased or decreased. Then, the second simulation is performed and a new mass flow is obtained. This is repeated until the obtained mass flow rate is equal to the given one with a convergence tolerance equals 10^{-6} (relatively to the given value). Although fixing the mass flow rate increases the computational time of the optimization, this constrains the optimization solver to not go for a higher mass flow rate during the optimization.

5.2.4 Optimization constraints

The geometry of the main nozzle has been optimized with two types of yarns which are a filament and a spun yarn. The only difference between them in the simulations is considered to be the diameter. Three constraints are taken into account in the optimization. The first constraint is the mass flow rate which has to be fixed during the optimization as mentioned. The second constraint is related to the geometry of the main nozzle, geometrical considerations. Table 5.1 lists the geometrical constraints of the optimization. Depending on the yarn diameter, the yarn inlet diameter D_1 has not to be smaller than a specific value and the needle tip diameter D_8 is fixed. The tube exit diameter D_9 and the nozzle total length L_2 have not to be higher than specific values.

Table 5.1: Geometrical constraints. The symbols are as in Figure 5.2

Constraints	Filament yarn	Spun yarn
Yarn diameter [mm]	0.2	0.4
Yarn inlet diameter	D_1	
Needle tip	D_8	
Tube exit diameter	D_9	
Nozzle total length	L_2	

The third constraint is related to what is called the threading or suction property of the main nozzle geometry. A "threadable" geometry of the main nozzle is the geometry which is able to suck air from the ambient air through the yarn inlet when it is supplied with a low mass flow rate. The threadable property is useful when the air jet loom is not working to easily insert a yarn inside it, as the yarn is inserted from the yarn inlet. Inserting a yarn is easier with an air flow which is sucked inside the main nozzle from the yarn inlet, than if the air flow goes out of the main nozzle from the yarn inlet. The goal of this constraint is to investigate the difference in the optimum force between a threadable and not threadable main nozzle geometry.

5.2.5 Optimization solver and inputs

The objective function for the studied cases changes nonlinearly and depends on multiple design variables which are constrained. The interior-point algorithm [96] is chosen to perform the optimization. The gradients of the objective function are set

to be estimated based on the central finite difference scheme with predefined step sizes of the variables. The objective function tolerance is set to 10^{-6}. Employing predefined step sizes for the gradients is important for two reasons which are the different variable values and effects. The values of the variables are not equal, for example, 1% of the total main nozzle length might be more than 2 mm which affects the force and, thus, the gradients. By contrast, 1% of the yarn inlet diameter might be less than 0.02 mm which might not generate any change in the force.

The inputs of the optimization are the lower and the upper bounds of the geometrical parameters, the corresponding step sizes and the initial values. The geometrical parameters which are included in the optimization are the ones which are shown in Figure 5.2 except the needle tip diameter D_8. The constraints in Table 5.1 are included in the bounds. If a variable is not constrained by a given value, the bounds of that variable are set to be in logical limits. The initial values of the variables are set to the ones of a reference geometry.

The optimization solver searches to find the minimum of the given objective function. Thus, the objective function for the optimization without threading constraint is set as $f = -\text{force}$. For the optimization with the threading constraint, the objective function is set as

$$f = -(\text{force}) \ : \ \text{if} \ \dot{m}_{\text{sucked}} \geq \dot{m}_{\text{given}}, \tag{5.1}$$

and

$$f = -\left(\text{force} - B\left(\dot{m}_{\text{sucked}} - \dot{m}_{\text{given}}\right)^2\right) \ : \ \text{if} \ \dot{m}_{\text{sucked}} < \dot{m}_{\text{given}} added, \tag{5.2}$$

with *B* is a constant which can be considered as a penalization factor and $\dot{m}_{given}$ the given mass flow rate which has to be sucked from the ambient.

Figure 5.8 shows the steps which are performed with each iteration of the optimization with threading constraint. The flow chart of the optimization without threading constraint is the same as in Figure 5.8 but without the step "Simulation with threading inlet condition" and after adjusting the mass flow rate, the objective function is directly calculated.

The code which is written to perform the optimization couples three tools: the optimization solver which is implemented in Matlab and which is used without modifications, geometry and grid creation which is Gambit (ANSYS Inc.) and the flow solver which is Ansys Fluent 15.0.

The geometry of the main nozzle is optimized with two different yarn diameters which are 0.2 mm and 0.4 mm. With each diameter two optimization types are performed: one with threading constraint and one without threading constraint. Therefore, in total four optimum geometries have been obtained.

5.3 Results and discussion

With the chosen optimization solver, the geometry obtained at the end of the optimization process corresponds to a local minimum of the objective function. This

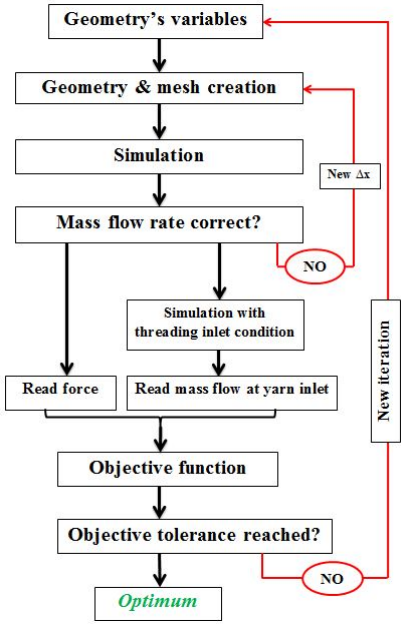

Figure 5.8: Flow chart of the optimization with threading constraint.

means that it might be possible to find another better geometry. Many factors affect the results of the optimization. Some of the factors are the initial point, the gradient estimating scheme and the gradient step sizes. Although the central scheme is expensive because it evaluates the gradient using two calculations (backward and forward) for each variable and each iteration, it is recommended for obtaining better results than the backward or the forward scheme.

Many attempts have been made to check that the obtained minimums are global and not local. First, the effects of changing the initial point are checked by carrying out two optimization attempts with different initial points. The initial point affects the direction in which the optimization solver goes and a different local minimum has been obtained with 5% difference in the values of the local minimums. Next, the effects of changing the gradient step sizes are checked by employing two sets of step sizes: the first set ranges from 2% to 5% and the second set ranges from 5% to 10%. A small difference is observed in the values of the local minimums which have been obtained with these two sets of the gradient step sizes.

For the optimization with threading constraint, constant B in Equation (5.2) is set to be high enough to force the optimization solver to go for a threadable geometry. The best obtained geometries from the four performed optimization cases will be presented and those geometries will be called the optimum geometries.

Figure 5.9 and 5.10 show contours of the Mach number with the optimum geometries and with a reference geometry for yarn diameter 0.2 mm and 0.4 mm, respectively. The improvements in the axial aerodynamic forces of the optimum geometries in

comparison to the forces of the reference geometry are listed in Table 5.2.

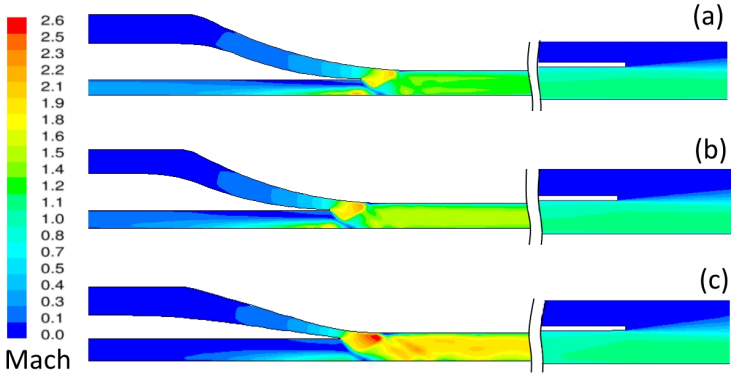

Figure 5.9: Contours of Mach number with yarn diameter 0.2 mm: (a) The optimum geometry without threading property; (b) The optimum geometry with threading property; (c) The reference geometry.

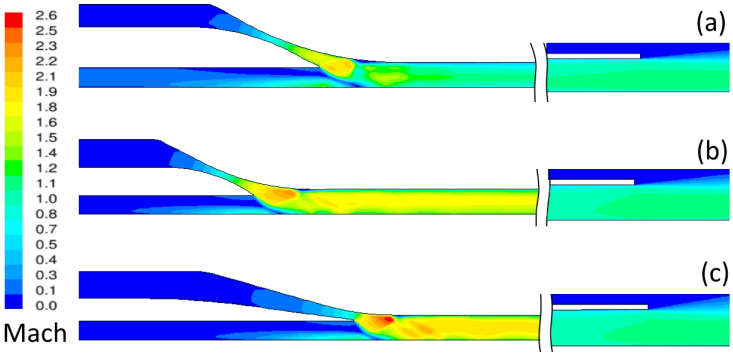

Figure 5.10: Contours of Mach number with yarn diameter 0.4 mm; (a) The optimum geometry without threading property; (b) The optimum geometry with threading property; (c) The reference geometry.

It can be seen in Figure 5.9 and 5.10 that the reference geometry generates higher velocities in the first part of the tube, after the needle tip, while, in the second shown part (around the tube exit) the velocities of all geometries are similar. Moreover, the differences in the values of Mach number between the reference geometries and the optimum ones with threading are smaller than the differences between the reference geometries and the optimum without threading. To show how the Mach number changes inside the geometries a line is chosen which is line1. The x-coordinate of line1 extends from the yarn inlet to the tube exit and the y-coordinate of line1 is equal to $D_{yarn\,inlet}/4$. Figure 5.11 and 5.12 show the Mach number along the x-coordinate of line1 with yarn diameter 0.2 mm and 0.4 mm, respectively.

It can be seen in Figure 5.11 and 5.12 that the flow in the tubes can be divided into two regions: a region with supersonic flow and another region with subsonic flow,

Table 5.2: Axial aerodynamic force of the optimum geometries in comparison to the reference ones.

Geometry	Optimum without threading	Optimum with threading
yarn diameter 0.2mm	+20.6%	+14.0%
yarn diameter 0.4mm	+15.4%	+3.6%

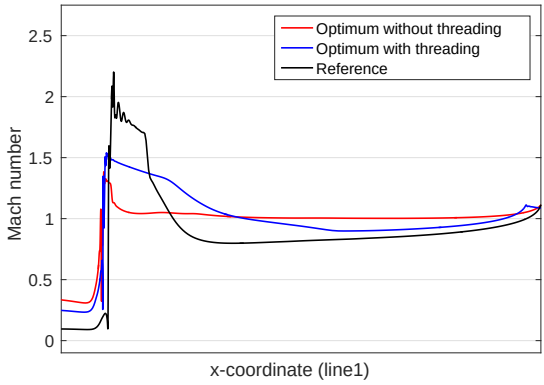

Figure 5.11: Mach number along line1 inside the nozzles with yarn diameter 0.2 mm. x-line1=yarn inlet:tube exit and y-line1=$D_{yarn\,inlet}/4$.

except in the optimum geometry without threading with yarn diameter 0.2 mm the second region is sonic rather than subsonic. Moreover, the region of the supersonic flow is shorter in case that the flow expands to higher Mach numbers in the first part of the tube. In all geometries, the flow at the tube exit is slightly supersonic.

These seen flow patterns are due to the tube inlet diameter (D_7 in Figure 5.2). This diameter is higher in the reference geometry than in the optimum geometries. Therefore, with almost the same throat section and the same upcoming mass flow, the flow has larger section (tube inlet) to expand which results in a higher velocity. Moreover, with the optimization the tube inlet diameter is affected by another diameter which is the yarn inlet diameter (D_1 in Figure 5.2). The yarn inlet diameter is constrained to be smaller than a specific value which is also smaller with yarn diameter 0.2 mm than with yarn diameter 0.4 mm, a thicker yarn needs a larger inlet hole. The inlet diameter data obtained from the optimization indicates that the optimization solver went for the smallest values of the yarn inlet diameter, especially if the threading constraint was not included. Eventually, the obtained tube inlet diameters are smaller than the one of the reference geometry.

The total length of the geometry (L_2) is the same in the reference geometry and in the optimum ones without threading property, whereas the total length is sightly shorter in those with threading property. Therefore, based on the above discussion and on the improvements listed in Table 5.2 it can be stated that it is better not to have a strong expansion of the flow at the beginning of the tube. This may be due

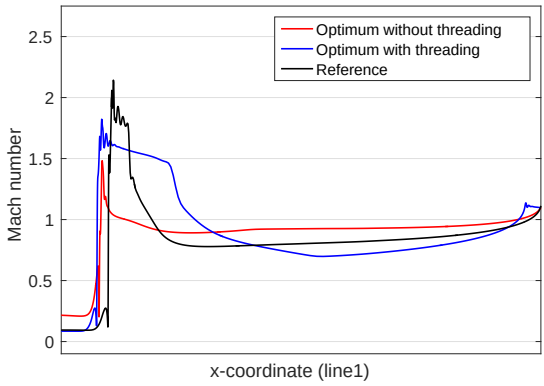

Figure 5.12: Mach number along line1 inside the nozzles with yarn diameter 0.4 mm. x-line1=yarn inlet:tube exit and y-line1=$D_{yarn\,inlet}/4$.

to two reasons: the tube length and the associated shocks. A stronger expansion will be associated with stronger shocks which increase the pressure loss. Moreover, there is pressure loss due to friction with the wall of the tube. Therefore, with the same inlet pressure, a stronger expansion of the flow at the beginning of the tube implies a smaller flow velocity far downstream inside the tube.

The threading constraint in the optimization reduces the maximal force in comparison to the cases without threading constraint. This was expected from experimental point of view. However, many geometrical differences exist between a threadable and non-threadable optimum geometry. The total length is shorter by about 3.2% in the threadable optimum geometries and the inlet yarn diameter is higher.

The air flows obtained from axisymmetric simulations, thus the axial aerodynamic force is only due to a viscous force. Therefore, the velocity gradient is the only variable which account for a high or a small force on the yarn or the cylinder wall. The axial velocity gradient in the radial direction ($\partial v_x/\partial r$) is shown in Figure 5.13 and 5.14 with yarn diameter 0.2 mm and 0.4 mm, respectively. The main nozzle geometry can be divided into two regions. The first region starts from the inlet of the yarn on the left hand side up to the needle tip and this region will be called the cylindrical tube. The second region starts from the tube inlet up to the tube exit and this region will be called the divergent tube as it is divergent in the shown geometries. In the cylindrical tube, all geometries generate a negative gradient in part of the tube due to the direction of the flow. The flow in the cylindrical tube goes out of the geometries (backward flow). Thus, the weft yarn is subjected to a negative force in part of the cylindrical tube. However, the negative force is limited to a short length of the weft yarn and it does not affect significantly the global force.

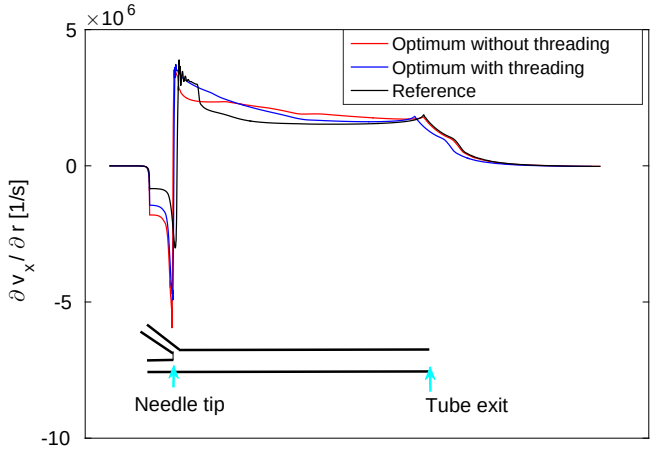

Figure 5.13: Axial velocity gradient along the cylinder wall (weft yarn) with diameter 0.2 mm.

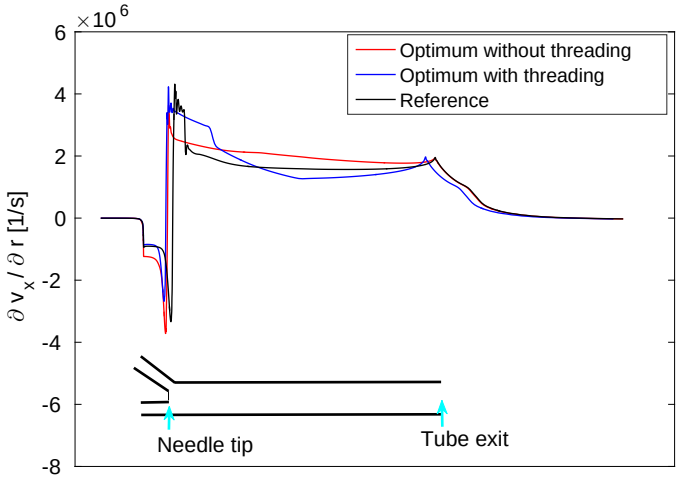

Figure 5.14: Axial velocity gradient along the cylinder wall (weft yarn) with diameter 0.4 mm.

Based on the plotted velocity gradients it can be said that with cylinder diameter 0.2 mm the optimum geometry without threading property generates a higher negative force than the one with threading property whose negative force is higher than the reference geometry. Conversely, with cylinder diameter 0.4 mm, the highest negative force is also seen with the optimum geometry without threading property

but the reference geometry generates higher negative force than the optimum one with threading property.

The backward mass flow rate of the optimum geometries in comparison to the reference one are listed in Table 5.3. It can be seen that the optimum geometries with and without threading property with yarn diameter 0.2 mm generate almost the same backward mass flow rate. By contrast, with yarn diameter 0.4 mm the optimum geometry without threading generates a higher backward mass flow rate than the one with threading. We deduce that the velocity gradients are linked directly to the backward mass flow rates. However, no clear link can be found between the values of the backward flows and the position of the throat sections. The general remark is that the backward flow in the cylindrical tube is greatly affected by the expansion and the shocks which take place next to the needle tip and the tube inlet.

Table 5.3: Backward mass flow rate of the optimum geometries in comparison to the reference one.

Geometry	Optimum without threading	Optimum with threading
yarn diameter 0.2mm	+55.9%	+54.4%
yarn diameter 0.4mm	+79.6%	-23.7%

The plotted velocity gradient increases sharply at the inlet of the divergent tube due to the expansion of the flow. The velocity gradient fluctuates more at the entrance of the divergent tube in the reference geometry than in the optimum ones with the two yarn diameters. These fluctuations are due to stronger expansions and shocks waves which happen with a higher velocity or pressure. After the divergent tube entrance, the velocity gradient in the optimum geometries without threading property decreases suddenly and then it maintains with very slow and smooth decrease in the remaining length of the cylinder wall. This trend, to some extent, is seen in the other geometries but the velocity gradient decreases to smaller values over a longer length of the cylinder wall in the optimum geometries with threading property and in the reference one.

The conclusion which can be drawn about the best flow pattern inside the tube of the main nozzle is that the strong expansion of the flow at the first part of the tube increases the pressure loss associated with the shocks and, eventually, this decreases the global aerodynamic force on the yarn.

5.4 Conclusion

In this chapter, an optimization procedure has been proposed to optimize the geometry of the main nozzle of air jet looms. This procedure is based on coupling three tools together which are an optimization solver, a geometry and mesh creation tool and a fluid flow solver. The structural geometry of the main nozzle is described through parameters which allow performing the optimization with a solver. The geometrical constraints are set as inputs to the optimization solver, whereas the

threading property is included in the objective function of the optimization. The weft yarn is presented as a cylinder in the fluid domain moving at a specific speed. The optimization has been performed for two cylinder diameters 0.2 mm and 0.4 mm with a given and fixed mass flow rate.

Many steps have been performed to check that the obtained results represent global and not local minimums. However, a global optimization solver is not effective to be used with the studied case and the proposed procedure due to the high required computational time with such a solver. Moreover, there is no guaranty that a global minimum can be obtained with such a solver due to the complexity of the studied case and the erratic change of axial forces, the objective function, in response to the geometrical changes.

The results of the optimization indicate that the axial forces with the obtained optimal geometries have been improved in comparison to reference values. Moreover, including the threading constraint in the optimization has reduced the optimum forces in comparison to the case without threading constraint. Two factors affect the threading property of the main nozzle. These two factors are the total length of the main nozzle and the expansion of the flow downstream of the needle tip. The total length of the nozzle is shorter with a threadable geometry than with a non-threadable one. The results of the optimization show that it is better to control the first expansion of the flow at the entrance to the tube. A strong expansion increases the pressure loss, thus decreasing the global force on the yarn.

The results of the optimization confirm the effectiveness of the proposed procedure to optimize the geometry of the main nozzle. Moreover, it would be no problem to add other constraints or variables for further investigation or optimization of the main nozzle geometry.

Chapter 6

Analytical analysis of the instability of the weft yarn inside the main nozzle

6.1 Introduction

In this chapter, the instability of a yarn inside a geometry of a main nozzle will be studied and investigated based on an analytical solution. By considering the yarn as a slender cylinder, the equations of motion of a slender circular body in axial flow can be used. Those equations have previously been derived based on the assumption that the cylinder does not move axially and only radial motion is analyzed. Although in reality the yarn inside the main nozzle moves axially and radially, the analytical solution might be used to study the flow or the yarn characteristics which generate the radial motion.

Axial flow-induced vibrations of slender circular bodies has attracted a great deal of research recently. This type of flow has been proven to produce dynamic instability at high flow velocities [97–104]. Moreover, it is not always possible to carry out experiments when the length of the cylinder is large. Two types of analytical equations of motion for a slender cylinder in axial flow have been derived. First, Païdoussis [97] derived the linear equations of motion and later Lopes et al. [105] derived the nonlinear equations of motion (detailed derivations can be found in [106, 107]). The linear equations of motion will be used in this work to calculate the analytical solutions. The nonlinear analytical equations and solutions are more complex to obtain and they have not provided substantially different dynamical aspects with regard to the linear ones [108].

6.2 Linear equations of motion for a slender cylinder in an axial flow

The linear equations of motion for a slender cylinder in an axial flow have been presented in detail in [7]. The assumptions and the equations will be presented here briefly. Figure 6.1 illustrates the schematic of a smooth cylinder in an axial flow inside a tube. The flow is considered to be incompressible and the axial velocity *U* is uniform. The assumption regarding the incompressibility is obviously an approximation for the flow in a main nozzle. The cylinder has a uniform cross section *A*, it is considered to be flexible, it is confined to move inside the tube and it is cantilevered. According to the procedure suggested in [7], the flow generates different types of forces on the cylinder which are viscous, inviscid and pressure forces.

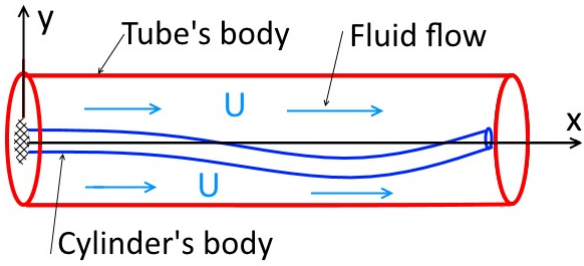

Figure 6.1: Schematic of a smooth cylinder in an axial flow inside a tube.

The inviscid force has been derived based on the potential flow theory. This force had been elaborated by Lighthill [109]. He considered that for lateral displacements of the cylinder *y(x,t)*, with *t* the time, the lateral force per unit length equals the rate of change of momentum of the fluid around the cylinder

$$L = -\left(\frac{\partial}{\partial t} + U\frac{\partial}{\partial x}\right) MV\,(x,t)\,, \tag{6.1}$$

where *L* is the lateral inviscid force per unit length or the lift force, *V(x,t)* is the relative lateral velocity between the fluid and the cylinder given as

$$V(x,t) = \left(\frac{\partial y}{\partial t} + U\frac{\partial y}{\partial x}\right), \tag{6.2}$$

and M is the added mass of the fluid per unit length. In a confined flow, the added mass equals $M = \chi\rho_f A$ where the cross section equals $A = \pi D^2/4$, (D is the cylinder's diameter), ρ_f fluid's density and χ the confinement parameter given as

$$\chi = \frac{\left(D_t^2 + D^2\right)}{\left(D_t^2 - D^2\right)}, \tag{6.3}$$

where D_t is the diameter of the tube.

The viscous forces on the cylinder have been derived by Taylor [110]. The normal friction force component F_N and the longitudinal one F_L (both per unit length) are equal to

$$F_{N,\text{viscous}} = 0.5\rho_f DU^2 \left(C_f \sin(i) + C_{Dp} \sin^2(i)\right), \tag{6.4}$$

$$F_{L,\text{viscous}} = 0.5\rho_f DU^2 C_f \cos(i), \tag{6.5}$$

where C_f and C_{Dp} are the friction and form drag coefficients. i is angle between the uniform axial flow and the cylinder (inclination angle). Païdoussis [7] suggested linearized and general forms of the viscous forces which are

$$F_{N,\text{viscous}} = 0.5\rho_f DUC_N \left(\frac{\partial y}{\partial t} + U\frac{\partial y}{\partial x}\right) + 0.5\rho_f DC_D \frac{\partial y}{\partial t}, \tag{6.6}$$

$$F_{L,\text{viscous}} = 0.5\rho_f DU^2 C_T, \tag{6.7}$$

with the normal and the tangential viscous force coefficients C_N and C_T. C_D is the zero-flow normal coefficient with $U = 0$ and its unit is $m.s^{-1}$.

The equation of motion for a slender cylinder with a free end at $x = L$ in axial flow after summing up all the forces, the above mentioned forces and the ones due to pressure drop and tension, can be written as reported in [7]

$$\begin{aligned} &EI\frac{\partial^4 y}{\partial x^4} + \chi\rho_f A\left(\frac{\partial}{\partial t} + U\frac{\partial}{\partial x}\right)^2 y + 0.5\rho_f DUC_N\left(\frac{\partial y}{\partial t} + U\frac{\partial y}{\partial x}\right) + 0.5\rho_f DC_D\frac{\partial y}{\partial t} \\ &- \left\{\left[0.5\rho_f DU^2 C_T\left(1 + \frac{D}{D_h}\right) + (m_s - \rho_f A)\, g\right](L - x) + 0.5\rho_f D^2U^2C_b\right\}\frac{\partial^2 y}{\partial x^2} \\ &\left[(m_s - \rho_f A)\, g + 0.5\rho_f DU^2 C_T\left(\frac{D}{D_h}\right)\right]\frac{\partial y}{\partial x} + m_s\frac{\partial^2 y}{\partial t^2} = 0, \end{aligned} \tag{6.8}$$

where E is the Young's modulus, $I = \pi D^4/64$ the second moment of area, $D_h = D_t$ the hydraulic diameter and it is equal to the tube diameter for the studied case. $m_s = A\rho_s$ is the mass of the cylinder per unit length with ρ_s is the density of the cylinder. $g = 9.81 m.s^{-1}$ is the acceleration of gravity, C_b the base drag coefficient of the cylinder's free end. No material damping is taken into account.

6.3 Solution method

Equation (6.8) is a differential equation. This involves imposing boundary conditions which are for a cantilevered cylinder

$$\begin{aligned} &\frac{\partial y}{\partial x} = 0,\ y = 0 \qquad &at\, x = 0, \\ &\frac{\partial^2 y}{\partial x^2} = 0 \qquad &at\, x = L. \end{aligned} \tag{6.9}$$

These boundary conditions mean that there is neither displacement nor rotation at the fixed end and the bending moment is zero at the free end. Moreover, if the free end is not blunt, it is subjected to aerodynamic forces. The boundary condition for a tapered free end is given as

$$EI\frac{\partial^3 y}{\partial x^3} + f\chi\rho_f AU\left(\frac{\partial y}{\partial t} + U\frac{\partial y}{\partial x}\right) + \left[f\chi\rho_f A\left(\frac{\partial^2 y}{\partial t^2} + U\frac{\partial^2 y}{\partial x \partial t}\right) + m_s\frac{\partial^2 y}{\partial t^2}\right]x_e$$
$$-\left(m_s - \rho_f A\right)g\frac{\partial y}{\partial x}x_e - 0.5\rho_f DU^2 C_T\frac{D}{D_h}x_e - 0.5\rho_f DUC_N\left(\frac{\partial y}{\partial t} + U\frac{\partial y}{\partial x}\right)\overline{x}_e = 0, \tag{6.10}$$

where f is a parameter whose value depends on the shape of the free end. The value of f is less than unity and it is zero when the free end is blunt. x_e and $\overline{x}_e$ are given as

$$x_e = \frac{1}{A}\int_{L-l}^{L} A\left(x\right)dx, \quad \overline{x}_e = \frac{1}{D}\int_{L-l}^{L} D\left(x\right)dx, \tag{6.11}$$

with l the length of the tapering and L the total length. It can be seen that Equation (6.10) contains time derivatives. Therefore, Païdoussis [7] suggested to include the boundary condition equations into the equation of motion which is expressed as

$$F\left(y\left(x,t\right)\right) + \delta\left(x - L\right)B\left(y\left(x,t\right)\right) = 0, \tag{6.12}$$

where F represents the equation of motion and B the boundary condition equation.

Equation (6.12) is solved by means of the Galerkin method $y\left(x,t\right) = \sum_{i=1}^{n}\phi_i\left(x\right)q_i\left(t\right)$ with $\phi_i\left(x\right)$ the mode shape function or the eigenfunction and $q_i\left(t\right)$ the generalized coordinate function $q_i\left(t\right) = q_i e^{\lambda_i t}$ with λ_i the eigenvalue. Equation (6.12) is first nondimensionalized and then the Galerkin method is applied, with a nondimensional eigenfunction, the resultant equation is similar to a damped free vibration equation (see [7] for more details).

Some of the dimensionless parameters which will be mentioned later in the discussion are

$$\beta = \frac{\rho_f A}{\rho_f A + m_s}, \quad \gamma = \frac{\left(m_s - \rho_f A\right)gL^3}{EI}, \quad \varepsilon = \frac{L}{D}, \quad u = \left(\frac{\rho_f A}{EI}\right)^{1/2}UL,$$
$$h = \frac{D}{D_h}, \quad c_N = \frac{4}{\pi}C_N, \quad c_T = \frac{4}{\pi}C_T, \quad c_b = \frac{4}{\pi}C_b,$$
$$c = \frac{4}{\pi}\left(\frac{\rho_f A}{EI}\right)^{1/2}LC_D, \quad \chi_e = \frac{x_e}{L}, \quad \overline{\chi}_e = \frac{\overline{x}_e}{L}.$$

The analytical solutions will be shown with Argand diagram, and critical values of the flow velocity will be highlighted.

6.4 Aerodynamic force coefficients

The aerodynamic force coefficients will be discussed according to the general formulas in Equation (6.6) and (6.7). Hoerner [111] suggested that $C_f = C_T$ and based on data fitting he found $C_T = 0.02$. He also reported a general formula to calculate C_T with turbulent boundary layers $C_T = 0.044\,(Re_L)^{-1/6}$. However, this formula is for a flat plate and not for a cylinder. Moreover, Keith et al. [112] and Cipolla and Keith [113] reported that the theory for the boundary layer on a flat plate cannot be used with cylinders and a different theory has to be used to determine the boundary layer on cylinders. The boundary layer on long and thin cylinders is thinner than the one on flat plates [114–116].

White [117] investigated turbulent boundary layers on long cylinder and he illustrated the obtained friction coefficient with Reynolds numbers and with different cylinder lengths. Richmond [118] performed experiments to measure the viscous coefficient of cylinders in axial, turbulent, subsonic and hypersonic flow. For a cylinder with diameter $6 \times 10^{-4} m$, he reported that the viscous coefficient is

$$\begin{aligned} C_f &= 0.00234 \quad \text{with Mach} = 5.59, \\ C_f &= 0.00518 \quad \text{with Mach} = 0.036. \end{aligned}$$

Ersdal and Faltinsen [119] measured the normal force coefficient of a long cylinder in near axial flow. They reported that $C_N = 0.068\alpha$ (with α in [rad]) for $\alpha \leq 4^o$. Divaret et al. [120] found almost the same conclusion of Ersdal and Faltinsen [119] by experimental study. Moreover, they found that the slope of the normal force coefficient decreased with increasing slenderness of the cylinder (*Length/Diameter*). They showed that for $L/D > 60$ the normal force coefficient could be calculated as $C_N = (0.11 \pm 0.016)\,\alpha$ (with α in [rad]) for $\alpha \leq 5^o$. However, the instability of the body studied in this work is a yarn which has to be considered as a cylinder with a rough surface. Païdoussis [7] suggested that $C_N/C_T = 0.5$ for a cylinder with very rough surface.

Little information exists on the zero-velocity normal force coefficient C_D. Païdoussis [7] suggested that this coefficient can be neglected. For the base drag coefficient C_b Hoerner [111] suggested that this coefficient can be calculated as $C_b = (\pi/4) \times 0.029/\left(C_{fB}\right)^{0.5}$ where C_{fB} is the drag coefficient for the forebody and it is equivalent to C_T.

6.5 Properties of the studied yarn

The yarn which is studied is Cotton 104 tex. Its properties are measured experimentally and they are as follows: the diameter equals $D = 0.4mm$, the material density $\rho_s = 875\,kg/m^3$ and Young modulus $E = 10345071\,N/m^2$.

Only the diameter of the geometry in which the cylinder is confined is included in the equation of motion. No other parameters or dimensions are included in the instability analysis. Moreover, as seen before, the tube of the main nozzle is

not cylindrical, it is rather conical. Therefore, the average tube diameter will be considered $D_{t,\text{average}} = D_h = (D_{t,\text{inlet}} + D_{t,\text{exit}})/2 = (3+4)/2 = 3.5mm$.

A steady state three-dimensional simulation has been performed with the reference geometry of the main nozzle which is shown in Figure 5.9. The obtained mean axial velocity, one value for the complete tube and with an inlet pressure of 5 bar relatively of the atmospheric pressure, $U_{x,mean} = 240.08m/s$ and the mean density $\rho_{mean} = 2.353kg/m^3$. Therefore, the Reynolds numbers based on the diameter and the length of the cylinder are

$$\begin{aligned} Re_D &= \frac{240.08 \times 2.353 \times 0.0004}{1.7894 \times 10^{-5}} = 12627, \\ Re_L &= \frac{240.08 \times 2.353 \times 0.28}{1.7894 \times 10^{-5}} = 0.88 \times 10^7, \end{aligned} \tag{6.13}$$

where the diameter of the cylinder is equal to the yarn diameter and the length (0.28 m) is the length of the cylinder inside the main nozzle. Moreover, the obtained tangential force on the cylinder is $F_T = 0.14379N$. With this value of the tangential force and based on the formula in (6.7)

$$C_T = \frac{0.14379/0.28}{0.5 \times 2.353 \times 240.08^2 \times 0.0004} = 0.0189. \tag{6.14}$$

Tables 6.1 lists the force coefficients which are taken from the mentioned references (first column). The specifications (second column) are the conditions with which the coefficient were obtained. Those specifications are close to the studied case specifications.

Table 6.1: Aerodynamic force coefficients. The tangential and the normal coefficients are taken for the references and the base drag coefficient is calculated according to Hoerner [111].

Reference	Specification	C_T	C_N	C_N/C_T	C_b
[120]	$Re_D = 24000$	0.012	0.0095	0.79	0.207
[118]	hypersonic flow	0.00735 ($C_f.\pi$)	-	-	0.0265
[117]	$Re_L = 10^7$ L/D=1000	0.0022	-	-	0.4855

As it can be seen in Table 6.1, the reported values of the tangential coefficient are different. Moreover, these values are not close to the value obtained from the simulation. However, the obtained value is not completely accurate because the mean values of the velocity and density are considered to be the same for the complete tube which is not the case. The most relevant value of the tangential force coefficient can be taken from [117] because the slenderness of the cylinder and the Reynolds number are close to the studied one ($L/D = 0.28/0.0004 = 700$). However, investigating multiple values of the force coefficients in the analytical solutions will be considered and presented.

6.6 Results and discussion

The analytical solutions are based on modal analysis. Thus, the response of the system or the free vibrations will be discussed based on complex eigenvalues. For a system with damping and without external force, the general solution can be expressed as

$$q(t) = Ae^{-Im(\omega)t} sin\left(Re(\omega)t + \phi\right), \tag{6.15}$$

where $Im(\omega)$ is the imaginary part of an eigenvalue, $Re(\omega)$ is the real part. Clearly, the response of the system depends mainly on the exponential function. If the exponential function increases with time, the vibration will be amplified. The exponential function increases if the imaginary part is negative. Therefore, for a negative imaginary part the instability occurs. The instability without periodic oscillations ($Re(\omega) = 0$) is a static instability and it is called divergence. With periodic oscillations $Re(\omega) \neq 0$, the instability is dynamic and it is called flutter. Therefore, the discussion will be focused on the critical flow velocities after which the cylinder is statically or dynamically unstable.

Table 6.2 lists the obtained values of mean velocity and density with different inlet pressures. Table 6.3 lists the properties of the yarn which will be used to obtain the critical velocities.

Table 6.2: Results of steady state simulations with different inlet pressures.

Inlet pressure	$U_{x,mean}[m/s]$	$\rho_{mean}\,[kg/m^3]$
1bar	151.25	1.323
2bar	194.97	1.496
3bar	220.03	1.740
4bar	234.69	2.036
5bar	240.08	2.353

Table 6.3: Properties of the studied yarn.

Property	Value
Length [m]	0.28
Diameter [m]	0.0004
Density [kg/m^3]	875
Young modulus [N/m^2]	10345071
Tangential force coefficient (C_T)	≥ 0.0022
Normal force coefficient (C_N)	0.0095 or $0.5C_T$
Zero flow drag coefficient (C_D)	0
Base drag coefficient (C_b)	≤ 0.4855

Figure 6.2 shows the lowest four modes with a fluid density equivalent to inlet pressure 1bar. A part of the fourth modes is shown and not the complete mode. It can be seen that the first and the second mode are stable, while the cylinder becomes

unstable in the third and in the fourth mode by flutter (single mode flutter). In the third mode, the cylinder loses stability at a critical flow velocity higher than 26.27 m/s. No divergence occurs before flutter. At a velocity higher than 33.16 m/s, the fourth mode restabilizes.

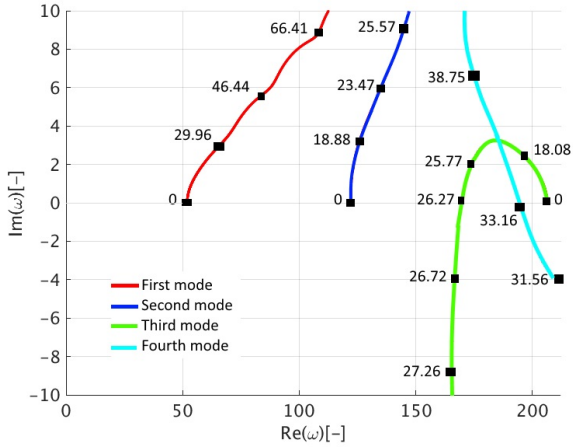

Figure 6.2: Argand diagram of the complex frequencies ω of the lowest three modes as a function of flow velocity (m/s) for $\rho_f = 1.323 kg/m^3$, $C_T = 0.0022$, $C_N = 0.0011\,(0.5C_T)$, $f = 0$ and $C_b = 0.4856$.

By increasing the density of the flow, according to different inlet pressures, the mass ratio β increases as it is listed in Table 6.4. Moreover, the critical flow velocity of flutter with the third mode decreases. The system remains stable in the first and the second modes with increasing density of the air.

Table 6.4: Effect of increase the density of the flow on the critical velocities of the third mode. The other parameter values are the same as shown in Figure 6.2: β is the mass ratio; U_{cf} is the critical velocity of flutter.

Inlet pressure	$\rho_{mean}\,[kg/m^3]$	β	$U_{cf}\,[m/s]$
1bar	1.323	0.0015	26.27
2bar	1.496	0.0017	24.70
3bar	1.740	0.002	22.90
4bar	2.036	0.0023	21.17
5bar	2.353	0.0027	19.77

In the above results, the force coefficients were not changed. However, Table 6.5 lists the obtained results with changing force coefficients according to the values listed in Table 6.1. It can be seen that by increasing the force coefficient the first three modes are stable. Moreover, the critical flow velocity of the flutter in the fourth mode increases with increasing force coefficients. It seems that by increasing the axial force coefficient the cylinder resists to oscillate at a small flow velocity.

Table 6.5: Effects of the force coefficients on the instability of the cylinder.

C_T	C_N	C_N/C_T	C_b	Stable modes	Unstable mode (flutter)
0.0022	0.0011	0.5	0.4855	1st & 2nd	3rd ($U_{cf} = 19.77m/s$)
0.0075	0.00375	0.5	0.263	1st & 2nd & 3rd	4th ($U_{cf} = 24.41m/s$)
0.012	0.0095	0.79	0.207	1st & 2nd & 3rd	4th ($U_{cf} = 40.81m/s$)

The effects of the flow properties on the instability of the yarn can be summarized as follows. Increasing the inlet pressure increases the density of the flow which decreases the critical flow velocity. Moreover, as the aerodynamic force coefficients for a yarn are higher than the ones for a cylinder, the yarn is more stable than a similar cylinder.

The shape of the free end of the cylinder has effects on its stability [98, 121, 122]. To investigate these effects, it is considered that the free end has a conical shape of 1mm length instead of being blunt. In this case, according to Lopes [106] (Table 1), $x_e = l_{end}/3 = 0.000334m$, $\overline{x}_e = l_{end}/2 = 0.0005m$ and $f = 0.8$.

Figure 6.3 shows the lowest three modes of the cylinder with the values of the critical velocities. It can be seen that the dynamics of the cylinder have changed significantly by changing the shape of the free end. In the first mode, the divergence occurs at a flow velocity 11.16 m/s but before this velocity is reached, the cylinder loses stability by flutter in the second and in the third mode at a velocity of 9.81 m/s and 10.33 m/s, respectively. In the second mode and at a velocity of 16.25 m/s the divergence occurs, then at a velocity of 16.33 m/s the cylinder restabilizes and again divergence occurs at a velocity of 17.82 m/s. In the third mode, after flutter, the cylinder restabilizes at a velocity of 16.4 m/s, then divergence occurs at a velocity of 24.26 m/s. However, in the second mode and by increasing the velocity, restabilization and divergence alternatively occur. Conversely, in the third mode the sequence of flutter, restabilization and divergence takes place by increasing the velocity. Therefore, the shaped free end of the cylinder has destabilizing effects on the dynamics of the cylinder. The shaped free end is subject to normal forces which excite it to move and thus, affect the dynamics of the cylinder.

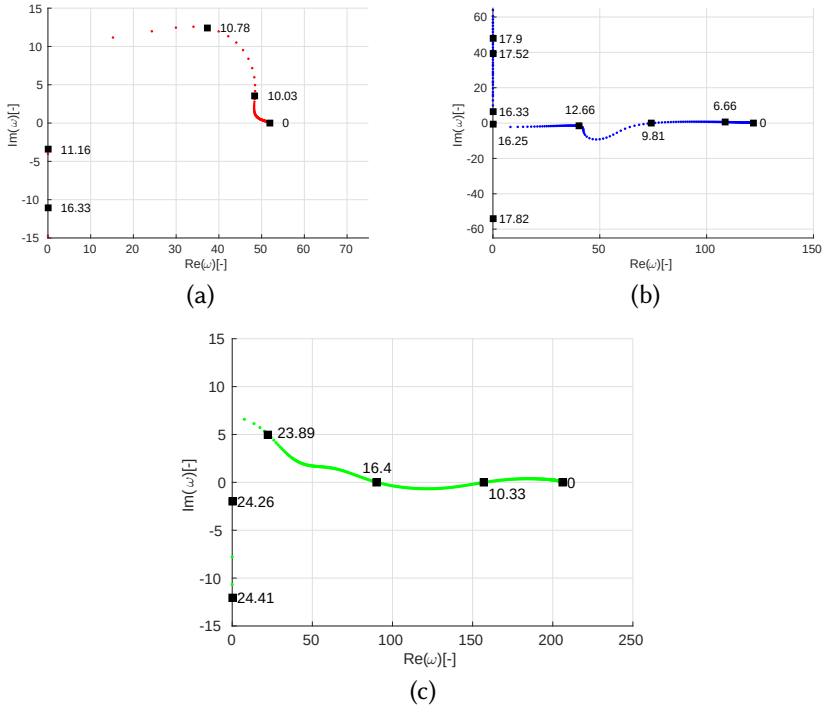

Figure 6.3: Argand diagram of the complex frequencies ω of the lowest three modes as a function of flow velocity (m/s) for $\rho_f = 2.353kg/m^3$, $C_T = 0.0022$, $C_N = 0.0011\,(0.5C_T)$, $f = 0.8$, $C_b = 0, \chi_e = 0.00119$ and $\overline{\chi}_e = 0.00178$: (a) First mode; (b) Second mode; (c) Third mode.

To investigate the effects of the cylinder's length on the stability, the length is increased and decreased by 0.1m. Table 6.6 lists the critical velocities with three lengths of the cylinder where 0.28m is the basic length. By decreasing the length of the cylinder, neither the critical velocities nor the mode are affected. However, by increasing the length of the cylinder, the second mode and the third mode are affected. It can be seen in Table 6.6 that with a length of 0.38m the cylinder in the second and in the third mode restabilizes before the divergence which is not the case with the length of 0.18m and 0.28m.

The effects of the cylinder length on the stability were investigated by De Langre et al. [122]. They found that a very long cylinder might be subjected to flutter. Moreover, Lemaitre et al. [123] found the same conclusion and, in addition, they found that the critical velocity at which flutter occurred was not affected after the cylinder became long enough (longer than 2.5 m). With the studied case, the length of the cylinder, the yarn, inside the main nozzle would not be higher than 0.35m. Therefore, it can be said that the cylinder will always be subjected to flutter.

Increasing and decreasing the channel diameter or the tube diameter by 1 mm has no effects on the critical velocities, the changes in the critical velocities are less than 1%. However, the yarn diameter has effects on the critical velocities as shown in

Table 6.6: Effects of the length of the cylinder on the critical flow velocity [m/s]. The parameters of the system are the same as shown in Figure 6.3 with the length being varied; U_{cd} is the critical velocity of divergence, U_{cf} the critical velocity of flutter and U_s the velocity of restabilization.

Length of the cylinder [m]	First mode	Second mode	Third mode
0.18	$U_{cd} = 11.18$	$U_{cf} = 9.67$ $U_s = 16.19$	$U_{cf} = 11.42$ $U_s = 16.77$ $U_{cd} = 25.16$
0.28	$U_{cd} = 11.16$	$U_{cf} = 9.81$ $U_{cd} = 16.25$	$U_{cf} = 10.33$ $U_s = 16.4$ $U_{cd} = 24.26$
0.38	$U_{cd} = 11.42$	$U_{cf} = 10.15$ $U_s = 16.22$ $U_{cd} = 19.2$	$U_{cf} = 10.1$ $U_s = 16.55$ $U_{cf} = 34.1$ $U_s = 34.87$ $U_{cd} = 75.59$

Figure 6.4. It can be seen that the critical velocities of divergence and flutter increase by increasing the yarn diameter. This means that a thinner yarn loses its stability at a smaller velocity than a thicker yarn. This can be understood by the effect of the diameter on the forces. Increasing the diameter of the cylinder increases the tangential force more than the normal force and, as has been seen before, increasing the tangential force has stabilization effects.

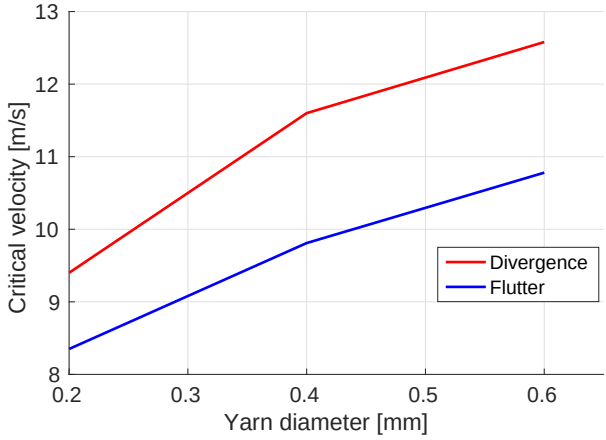

Figure 6.4: Effects of the yarn diameter on the critical velocities of divergence and flutter, the other parameters of the cylinder and the flow are as in Figure 6.3.

6.7 Conclusion

In this chapter, the instability of yarns, represented as cylinders, has been analyzed based on the analytical equations. The results of the analytical solution indicate that the instability of the weft yarn can be postponed to a higher flow velocity if the free end is blunt as opposed to not blunt, having for example a conical shape. Increasing the density of the flow decreases the critical velocity at which the cylinder loses stability. However, the stability of a cylinder can be improved by increasing the roughness of its surface which is the case with a similar yarn. With the working conditions of weaving machines (inlet pressure of 5 bar), the weft yarn is unstable and it is subjected to flutter. However, with holding flow conditions, the weft yarn is not necessarily unstable depending on its diameter and length because the air flow velocity may be smaller than the critical velocity of divergence or flutter.

The analytical equations are based on the assumption that the flow is incompressible. This means that there are effects which are not taken into account and which affect the instability of yarns, for example, shock and expansion waves. However, obtaining the analytical solution is much faster than a three-dimensional fluid-structure interaction simulation. Therefore, it can be employed to investigate generally the dynamic behavior of yarns.

Chapter 7

Fluid-structure interaction simulations of air flow-yarn with fixed mesh

In this chapter, fluid-structure interaction simulations of air flow-yarn with a fixed mesh inside a main nozzle of an air jet loom will be presented. With this type of simulations, the effect of yarn motion on the air flow is added by a source term. This chapter has been published in [9].

This chapter starts with an overview of the previous studies about the motion of the yarn inside main nozzles. Next, the fluid model which has been derived and implemented and the structure model which has been employed are explained. These two models are coupled with an in-house code to perform the fluid-structure interaction simulations. The results of the simulations are then presented and compared with experimental data and video.

7.1 Introduction

The main nozzle plays an essential role in the weft insertion system of an air jet loom. The weft yarn is supposed to move along the nozzle's axis. However, the supersonic and turbulent air flow inside the main nozzle and the associated shock waves give rise to additional normal forces if the yarn deviates from the axis, which always happens due to gravity and inevitable small perturbations during insertion. The complexity of the air flow pattern inside the main nozzle and the flexibility of a yarn make the prediction of the motion of the weft yarn a challenge. It principally involves modeling the interaction between the weft yarn and the air flow.

In the previous chapter, the instability of a yarn inside a geometry of a main nozzle has been analyzed based on the linear equations of motion. It has been reported that there are some flow characteristics which are not present in the analytical equations,

such as the shock waves. Therefore, to analyze the motion of yarns inside main nozzles, a better method or procedure has to be conducted which is based on coupled fluid-structure interaction simulations.

Modeling the dynamic behavior of the weft yarn has been attracting interest. The previous related works can be divided into two types or categories: one-way and two-way fluid-structure interaction (FSI) simulations. In the one-way FSI simulation, the effects of the yarn motion on the air flow are not taken into account. By contrast, in the two-way FSI simulation, the mutual interaction between the air flow and the yarn is taken into account.

7.1.1 One-way fluid-structure interaction simulations of air flow-yarn

Research on dynamics of weft yarns started early in the 1970s. For example, Uno [124] derived the equations of motion of air jet weft insertion utilizing empirical relations to determine the air flow velocity and the air friction coefficient. Moreover, he considered that yarns moved along the axis of the main nozzle, with no radial motion. He concluded, based on the derived equations of motion, that the initial air flow velocity should be high to accelerate the weft yarn in a short time. Moreover, the obtained equations of motion were employed by Uno et al. [125] to study some parameters which influence the weaving process, for example, the effects of the weft yarn count on its velocity or on the time for one insertion. Adanur and Mohamed [126] and [127] derived theoretical models for yarn motion and tension in drum and loop-storage systems for air jet insertion. They presented a numerical technique to solve the equations of motion for the yarn and to calculate the resulting yarn velocity. Moreover, they found that to increase the speed of the weft yarn the tension which restrains the yarn should be decreased.

Turel et al. [128] and Adanur and Turel [129] developed an air jet filling insertion simulator to analyze the effects of yarn and of air flow characteristics on the insertion time. They found that by decreasing the mass of the weft yarn and increasing its hairiness decreased the insertion time. Celik et al. [130], Nosraty et al. [131], Patkó [132] and Szabó et al. [133] derived the equation of yarn motion in air jet weaving machines and solved it numerically to calculate yarn's position and velocity [130, 133] or yarn tension [131].

Simulations of the air flow in all above mentioned works were not carried out. The air flow velocity or pressure were estimated based on empirical relations. Moreover, they dealt with the yarn as a whole and they derived the equations of motion based on this assumption. However, their results were important. For example, Nosraty et al. [131] obtained based on their model results in good agreement with experimental data, as shown in Figure 7.1. The differences in Figure 7.1 between the theoretical and the experimental data were explained by model simplifications.

The first work which divided the yarn into segments and which studied the dynamic behavior of the weft yarn based on a fully numerical model might be the one conducted by Vangheluwe et al. [134]. They derived a numerical model that

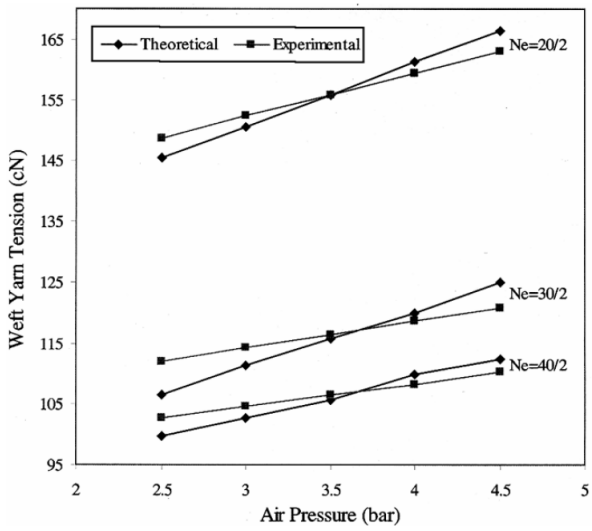

Figure 7.1: Effects of the air pressure on the maximum yarn tension; Ne is the yarn count, taken from [131].

described the motion of a flexible weft yarn. They divided the weft yarn into cylindrical segments (finite volume). Their goal was to calculate the tensions in the weft yarn during the weft insertion on a projectile and rapier loom. They showed that the tension was not constant along the length of the weft yarn. De Meulemeester et al. [135] developed a one-dimensional model and extended it later to a three-dimensional model (De Meulemeester et al. [136]) to study the dynamic motion of the weft yarn. They included the aerodynamic, contact and tensile forces in their model. They validated their results with high speed camera recordings.

Cai and Oxenham [137] performed one-way simulations of air flow-fibers in the fiber transfer channel of a rotor spinning machine. They calculated the air flow with a CFD software package and transferred the resultant velocity and pressure to a fiber movement model. They showed the effectiveness of using numerical tools to study the dynamics of fibers in textile processes. Tang and Advani [138] and Kondora and Asendrych [139] modelled the motion of fibers by representing the fiber as a chain of spheres connected by ball and socket joints.

The one-way FSI simulation can predict the yarn motion but it is not accurate in case that the influence of the yarn displacements is significant. The yarn, or the structure in general, has effects of the air flow field. For small yarn displacements, these effects might be neglected, therefore, the one-way FSI simulation can be used. However, during the insertion process in the weaving machine the weft yarn moves axially and radially with big displacements, thus the one-way FSI simulation cannot predict the weft yarn motion accurately and only the two-way FSI simulation can do that.

7.1.2 Two-way fluid-structure interaction simulations of air flow-yarn

The most important step to perform two-way FSI simulations is to satisfy the equilibrium conditions at the interface between the structure and the fluid at each time step as explained in Section 2.5. Therefore, in the two-way FSI simulation, the mutual interaction of air flow-yarn is taken into account by applying and satisfying those conditions.

Pei and Yu [140, 141] performed a two-dimensional two-way fluid-structure interaction simulation of the fiber motion inside the air jet nozzle of a Murata vortex spinning (MVS) machine. A direct FSI coupling solution method, the so-called monolithic approach, was used, which means that the fluid and the structure equations were solved together in one system. They used the arbitrary Lagrangian-Eulerian (ALE) technique in which the mesh is dynamic. They could highlight the trailing end yarn motion and they studied the effects of nozzle pressure and yarn delivery speed on the fiber motion. Wu et al. [142] studied the effects of yarn whipping at the exit of a main nozzle on the insertion process during the start-up stage by carrying out two-way FSI simulations of air flow-yarn. They represented the geometry of the main nozzle as well as the yarn in a two-dimensional configuration and they fixed the yarn at the exit of the main nozzle. They also employed the ALE technique. Furthermore, they took into account the pressure effects but ignored the viscous force.

Employing the ALE technique in a two-way FSI simulation of air flow-yarn interaction may distort the mesh, especially with a flexible body like weft yarn. Therefore, Jin et al. [143] suggested an adaptive grid control method to overcome the mesh distortion due to large deformations of the yarn.

7.1.3 Air flow-yarn interaction inside the main nozzle of an air jet loom

In the weaving machine, the process of transporting the weft yarn from the yarn package to the reed is called the insertion process. Based on the above discussion it can be said that the insertion process cannot be studied and analyzed without taking into account the air flow-yarn interaction. Moreover, dealing with the weft yarn as a whole is not completely accurate because the motion of the weft yarn depends on the different forces which act on it and which are not uniform along it. The one-way FSI simulation is not accurate because the effects of the weft yarn motion on the air flow are not taken into account. However, the two-way FSI simulation with the arbitrary Lagrangian-Eulerian (ALE) technique becomes complex due to the difficulties in handling the dynamic mesh with a flexible yarn. Moreover, the three-dimensional two-way FSI simulation requires a high amount of computational resources. Owing to the reasons mentioned above, a different procedure is proposed to perform the FSI simulation of air flow-yarn during the insertion process. In the proposed procedure the ALE technique is not employed, but instead the effects of the weft yarn on the air flow in the two-way FSI simulation is included by employing the added source term approach with a static mesh. In the following sections, the structure and the fluid models will be presented.

7.2 Numerical models

A fluid and a structure numerical model have been developed and employed to simulate the motion of the weft yarn. The contact, gravity, tensile and bending forces and the interaction between the air flow and the weft yarn are all considered in these models. One-way and two-way FSI simulations of the air flow and the yarn inside two different main nozzles are carried out. In the two-way FSI simulation, the air flow exerts aerodynamic forces on the weft yarn which in turn exerts forces on the air flow. These forces are added as a source term to the momentum equation of the air flow. By contrast, in the one-way FSI simulation, the yarn's force on the air flow is not added by disabling the source term. The structure model which is employed to calculate the deformations of the weft yarn is a three-dimensional model of the flexible yarn, consisting of a chain of line segments. The fluid model is two-dimensional axisymmetric as the main nozzle is axisymmetric after the inlet.

An in-house code is employed to couple the structure and the fluid solvers. Figure 7.2(a) shows the most important steps which are performed in the fluid and structure solvers. The coupling algorithm controls both solvers and transfers data between them (see Figure 7.2(b)). In the following paragraphs, some steps will be explained in detail, while others will only be mentioned and the reader will be referred to related work.

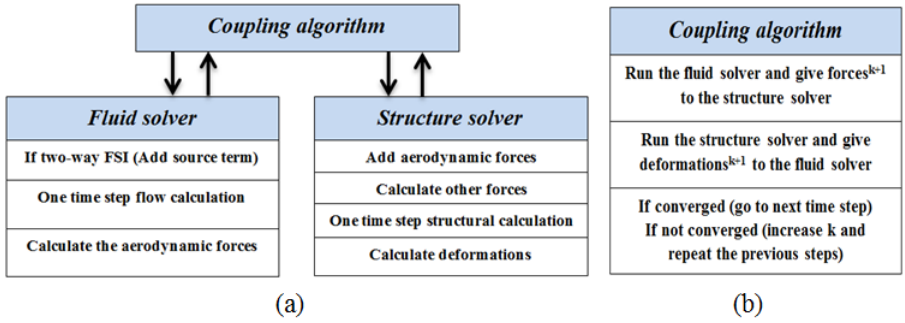

Figure 7.2: The numerical models: (a) the performed steps in the fluid and structure solvers; (b) the sequence in the coupling algorithm in each time step (k is the iteration's number).

7.2.1 The structure model

The structure model which is employed in this work is the same as in De Meulemeester et al. [136] with wall contact improvements and bending forces added. The yarn is represented with a three-dimensional model which consists of a chain of line segments. The geometry with which the yarn can make contact (nozzle, prewinder, ...) is represented by 3D objects. The yarn is divided into N segments. The mass of each segment (m_i) is concentrated at its center which is called a node. Each node is connected to the neighboring nodes by springs as shown in Figure 7.3.

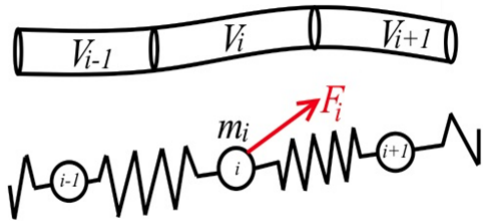

Figure 7.3: Representation of yarn segments and nodes in the structure model.

This means that the weft yarn is assumed to be a flexible body. The Second Law of Newton is applied to each node resulting in

$$F = m\frac{dv}{dt} \longrightarrow \overrightarrow{F}_i = m_i \frac{\triangle \overrightarrow{v}_i}{\triangle t},\ \overrightarrow{v}_i = \frac{\triangle \overrightarrow{x}_i}{\triangle t}, \tag{7.1}$$

where $\overrightarrow{F}_i$ represents the total force acting on mass m_i, $\overrightarrow{v}_i$ is the nodal velocity and $\overrightarrow{x}_i$ is the nodal position.

By using explicit forward Euler time integration twice, the velocity and the position of each node is calculated as

$$\overrightarrow{v}_i^{t+\triangle t} = \overrightarrow{v}_i^t + \overrightarrow{F}_i^t \frac{\triangle t}{m_i}, \qquad \overrightarrow{x}_i^{t+\triangle t} = \overrightarrow{x}_i^t + \overrightarrow{v}_i^t \triangle t. \tag{7.2}$$

The forces which are acting on each node are aerodynamic, gravitational, contact, bending and tensile forces. During the simulation, the weft yarn is constrained to move inside the surrounding solid surfaces using contact calculation. At the beginning of the calculation, the yarn nodes are positioned starting from the prewinder and ending at the nozzle tube's exit as it will be shown later. The different forces to which the weft yarn is subjected are all included over the complete length of the weft yarn in the structure solver. The yarn nodes which are located inside the fluid domain are also subjected to the aerodynamic forces computed by the fluid solver as will be explained below.

The tensile forces are calculated as in De Meulemeester et al. [136] and bending forces as in Baraff and Witkin [144]. For the contact it is affordable to detect contact of every node with every surface as only a limited number of mathematical objects like boxes, cones, cylinders and tori is used in the simulations. The intersection's position and time is determined for every contact and an impulse based collision response is applied as for rigid balls. This corrects the computed speeds and positions of the nodes that undergo contact.

7.2.2 The fluid model

The air flow is compressible and turbulent. This means that the governing equations which have to be solved are the Navier-Stokes equations or the momentum equation

Equation (2.2), the mass conservation Equation (2.1) and the energy conservation Equation (2.3). The two-equation shear stress transport k-ω (k-ω SST) model (Menter [13]) is employed to model the turbulence.

In the fluid model, the yarn is modeled as a rigid cylinder without shear stress on its surface and positioned along the axis of the main nozzle. The finite volume grid is stationary regardless of the yarn motion and the arbitrary Lagrangian-Eulerian (ALE) technique is thus not used. Conversely, the influence of the yarn motion on the flow is taken into account by adding a source term in the momentum equation. This approach avoids the difficulties with deforming grids for large deformation. The rigid cylinder on the axis ensures that the volume occupied by the yarn is considered in the simulation; the free-slip wall ensures that the flow is not decelerated along the wall of this cylinder as the yarn is not truly located at this position.

I. Calculating the aerodynamic forces

Although the air flow simulation domain is 2D axisymmetric, the aerodynamic forces are calculated in three-dimensional configurations. This means that the three components of the aerodynamic force are calculated: one component along the yarn and two components normal to the yarn. Two types of aerodynamic forces are considered. The first type is a regular drag force

$$\overrightarrow{F}_{i,L} = \frac{1}{2} C_L \rho_f \| \overrightarrow{v}_{i,\text{relative},L} \| \overrightarrow{v}_{i,\text{relative},L} | \overrightarrow{\triangle l}_i |, \tag{7.3}$$

$$\overrightarrow{F}_{i,N} = \frac{1}{2} C_N \rho_f \| \overrightarrow{v}_{i,\text{relative},N} \| \overrightarrow{v}_{i,\text{relative},N} | \overrightarrow{\triangle l}_i |, \tag{7.4}$$

where C_L and C_N are the longitudinal and normal force coefficients, ρ_f is the density of the air and $\overrightarrow{v}_{i,\text{relative},L}$ and $\overrightarrow{v}_{i,relative,N}$ are the longitudinal and normal components of the relative velocity between the air and the yarn. $|\overrightarrow{\triangle l}_i|$ is the length of a yarn segment which is calculated according to (see Figure 7.4(a))

$$|\overrightarrow{\triangle l}_i| = \sqrt{\left(\frac{x_{i+1} - x_{i-1}}{2}\right)^2 + \left(\frac{y_{i+1} - y_{i-1}}{2}\right)^2 + \left(\frac{z_{i+1} - z_{i-1}}{2}\right)^2}. \tag{7.5}$$

The yarn diameter is not included in Equations (7.3) and (7.4) because it is taken into account in the normal and longitudinal force coefficients.

The second type is an additional pressure drag force counting for the effects of the shock waves along which the pressure gradients change significantly

$$\begin{aligned} \overrightarrow{F}_{i,grad(p)} &= \oiint_s (p\overrightarrow{n})\, dS = \iiint_V \overrightarrow{grad}\,(p)\, dV, \\ &\approx \overrightarrow{grad}\,(p_i)\, V_i = \overrightarrow{grad}\,(p_i)\, |\overrightarrow{\triangle l}|_i \pi r_{yarn}^2, \end{aligned} \tag{7.6}$$

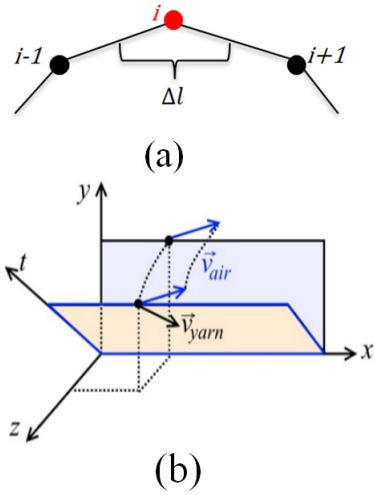

Figure 7.4: (a) The weft yarn current node with the two neighboring nodes. (b) Yarn and air velocities representation.

$$\overrightarrow{F}_{i,grad(p),N} = \overrightarrow{F}_{i,grad(p)} - \left(\overrightarrow{F}_{i,grad(p)}.\overrightarrow{n}_i\right)\overrightarrow{n}_i, \tag{7.7}$$

$\overrightarrow{grad}\,(p_i)$ is the pressure gradient vector and V_i is the volume of yarn segment i. $\overrightarrow{n}_i$ is the unit vector which is calculated as

$$\overrightarrow{n}_i = \frac{\overrightarrow{\triangle l}_i}{|\overrightarrow{\triangle l}|_i}. \tag{7.8}$$

The longitudinal component of the pressure gradient forces is not included in the resultant forces because each segment of the yarn is connected to the neighboring ones.

The data which is needed to calculate the aerodynamic forces is obtained as follows. In each time step the fluid solver receives the yarn's new nodal coordinates from the structure solver through the coupling algorithm. The yarn velocities are calculated according to

$$\overrightarrow{v}_{i,\text{yarn}} = \frac{\overrightarrow{x}_i^{t+\triangle t} - \overrightarrow{x}_i^{t}}{\triangle t}. \tag{7.9}$$

Then, the fluid cells in which the yarn nodes are located are identified. Subsequently, the air density and the pressure gradient are obtained for these cells. The velocity

components of the air flow are interpolated based on linear interpolation using the cell center velocity $\overrightarrow{v}_{i,c}$ and its velocity gradient $\overrightarrow{grad}(v_{i,c})$:

$$\overrightarrow{v}_i = \overrightarrow{v}_{i,c} + \overrightarrow{grad}(v_{i,c}) . \overrightarrow{\triangle l}_{ic}, \tag{7.10}$$

where $\overrightarrow{v}_i$ is the computed flow velocity at the location of structure node *i* and $\overrightarrow{\triangle l}_{ic}$ is the distance vector between the cell center and yarn node *i*.

The longitudinal and normal relative velocities at structural node *i* are calculated according to

$$\overrightarrow{v}_{i,\text{relative}} = \overrightarrow{v}_{i,\text{air}} - \overrightarrow{v}_{i,\text{yarn}}, \tag{7.11}$$

$$\overrightarrow{v}_{i,\text{relative},L} = (\overrightarrow{v}_{i,\text{relative}} . \overrightarrow{n}_i)\, \overrightarrow{n}_i, \tag{7.12}$$

$$\overrightarrow{v}_{i,\text{relative},N} = \overrightarrow{v}_{i,\text{relative}} - \overrightarrow{v}_{i,\text{relative},L}. \tag{7.13}$$

The air velocity $v_{i,\text{air}}$ is computed in the *xy* plane due to the axisymmetric representation of the flow domain, but it is rotated to the meridional plane *xt* which contains the yarn node to convert the two-dimensional velocity vector to a three-dimensional velocity vector $\overrightarrow{v}_{i,\text{air}}$ (see Figure 7.4(b)).

In consequence, the resultant aerodynamic force in yarn node *i* is calculated as

$$\overrightarrow{F}_i = \overrightarrow{F}_{i,L} + \overrightarrow{F}_{i,N} + \overrightarrow{F}_{i,grad(p),N}. \tag{7.14}$$

II. Source term

Two types of FSI simulations are carried out in this work: one-way and two-way. The fluid grid is static but a source term is added to the fluid equations. This source term represents the force which is exerted by the moving structure on the surrounding fluid. Therefore, the source term has to be added to the momentum equation. Since in the axisymmetric flow calculation a 3D nodal point cannot be mapped to one location, the action of the force is spread out over the cell containing the structure node and all cells at the same axial position, forming a radial set of cells. For example, Figure 7.5(c) shows a yarn node i with the associated radial set of cells (1 to m). The source term added to this radial set of cells is defined as

$$S = -\frac{\left(F_{i,L} + F_{i,N} + F_{i,grad(p),N}\right)_x}{\sum_j^m V_j}, \tag{7.15}$$

where *S* is the source term per unit of volume, *m* refers to number of cells in that radial set of cells and V_i is the i^{th} cell volume.

This is repeated for every structural node and contributions due to multiple yarn nodes in the same radial set are added. Since the flow calculation is 2D axisymmetric it does only make sense to include the axial component of this force. Therefore, the

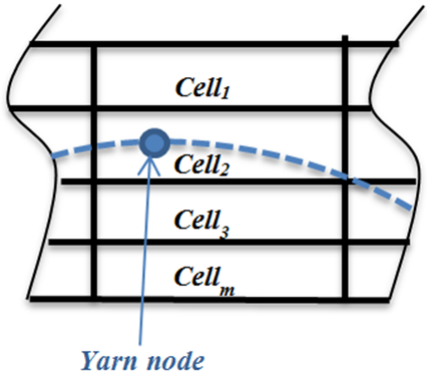

Figure 7.5: Representation of a yarn node and the cells in radial direction (1 to *m*) in which the source term is distributed.

source term is only added to the axial momentum equation of the flow. The resultant value of the source term is applied to each of the cells in the radial set. As result, the source term is distributed in each cell in the radial direction and it is weighted by each cell's volume. The source term is only calculated and distributed inside the nozzle. For the one-way FSI simulation, the source term is not added, so the effect of the yarn on the air flow is disregarded.

7.2.3 Coupling algorithm

The Gauss-Seidel coupling algorithm is employed to couple the fluid and the structure solvers. This algorithm couples the two solvers strongly or implicitly. A strongly coupled technique involves fulfilling the kinematic equilibrium (2.9) and the dynamic equilibrium (2.10) conditions on the fluid-structure interface at the end of each time step. These conditions stipulate that the velocity and traction have to be the same on the fluid and solid side of the fluid-structure interface.

The iteration scheme of the Gauss-Seidel coupling algorithm is explained in Degroote et al. [145] and it is shown in Figure 7.2(b). First the flow equations are solved based on the last position of the structure. Second, the structural deformations are calculated based on the new results of the air flow. These two steps are iterated in each time step before going to the next one until the equilibrium conditions are satisfied up to a convergence tolerance.

7.3 Experiment

To validate the results of the simulations, they are compared with experimental results provided by Picanol NV (Ieper, Belgium). The available experimental results are recorded lengths with two nozzles (called nozzle A and B) and videos recorded by a high-speed camera. The camera type is Kodak Ekta Pro EM. The image capture

rate was adjusted to 3000 frames per second to capture clearly the motion of the yarn. The recorded lengths represent lengths of the weft yarn which went out of the nozzle during the experiment, or the position of the yarn tip. These lengths were recorded at different times during the experiment. The videos show the motion of a cotton 104 tex yarn in the main nozzles. The tubes of the main nozzles are made of glass, which allows to show the motion of the yarn inside the tubes. The yarn was cut at the exit of the main nozzle's tube before the insertion.

Table 7.1 shows the properties of the used yarn. These properties are experimentally measured in Picanol, Ieper except for the aerodynamic force coefficients. In De Meulemeester et al. [136] the tests which were carried out to measure these properties are explained in detail.

Table 7.1: Properties of the yarn according to De Meulemeester et al. [136].

Property	Cotton 104 tex
Density (tex)	104
Friction: $\mu(yarn/metal)$	0.22-0.28
Elasticity: E ultrasonic (cN/tex)	480
Elasticity: E wheel (cN/tex)	254
Elasticity: E static (cN/tex)	164
Longitudinal aerodynamic force coefficient: C_L	0.00007
Normal aerodynamic force coefficient: C_N	0.000764
Bending stiffness: EI (Nm^2)	1.23×10^{-8}

The normal aerodynamic force coefficient is determined experimentally as explained in De Meulemeester et al. [136]. The longitudinal force coefficient is determined in such a way that the obtained position of the yarn tip with nozzle A with the two-way FSI simulation is the same as the one measured in the experiment. After obtaining the force coefficients with nozzle A, their applicability to the other nozzle is verified with nozzle B as will be shown later. By following this procedure, the effects of the hairiness of the yarn are included in the aerodynamic force coefficients.

A meridional section of the main nozzle (nozzle A or B) in which the experiment is carried out is shown in Figure 7.6. Table 7.2 lists the dimensions indicated in Figure 7.6 for both nozzles.

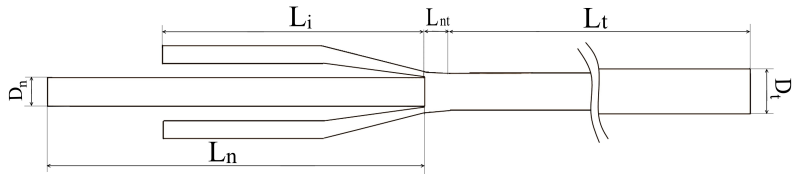

Figure 7.6: Meridional view of the geometry of the main nozzle with indication of the major dimensions.

At the beginning of the experiment the main nozzle is supplied by a holding flow with a limited flow rate. This air flow generates aerodynamic forces which are sufficient to hold the weft yarn at the axis of the main nozzle. Before releasing the

Table 7.2: Dimensions of the geometry of the main nozzles A and B [mm].

		Nozzle A	Nozzle B
L_i	Inlet length	22	18
L_{nt}	Distance between the needle and the tube	2	1
L_t	Acceleration tube length	240	218
D_t	Acceleration tube exit diameter	4	3
L_n	Needle length	30	25
D_n	Needle inlet diameter	2.2	1.8

yarn, 5 bar pressure is applied by opening a valve. 1.9 *ms* after the opening of the valve, the magnet pin is opened and the yarn is released. The main nozzle blows for 43 *ms* after the yarn has been released.

7.4 FSI simulations setup

As mentioned above, the yarn is represented as a cylinder at the axis of the tube with a diameter equal to 0.4 *mm*. The yarn wall is present along the second and the third zone (see Figure 7.7(a)). Since the effect of the force by the yarn on the flow is represented by momentum sources spread out in radial direction, this cylinder at the center is only used to take into account the volume obstruction effect and therefore its wall is treated as a no shear boundary condition (pink color in Figure 7.7(a)).

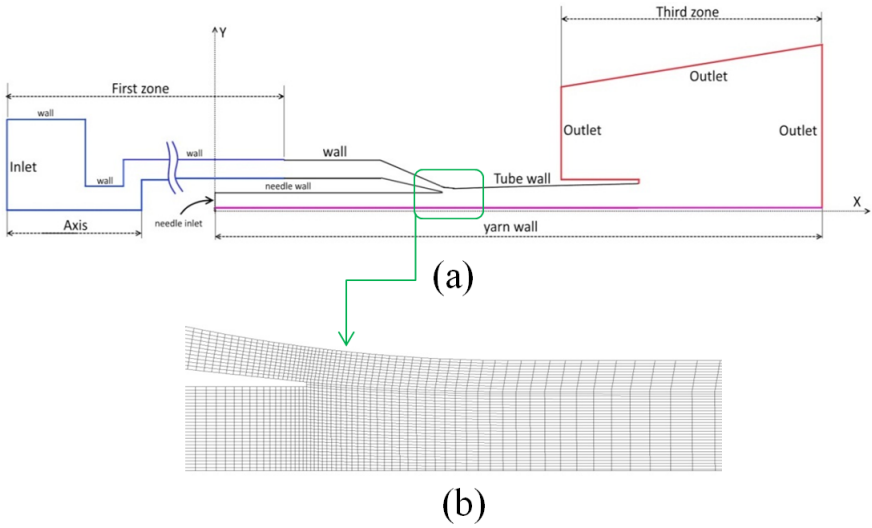

Figure 7.7: (a) Computational fluid domain with the boundary conditions; (b) detail of the mesh.

The structured (quadrilateral cells) mesh (see Figure 7.7(b)) contains about 36000 cells. The 2D axisymmetric transient numerical solutions were performed using An-

sys Fluent 14.5 in which the coupled scheme is used as solution method for pressure and velocity. Different schemes are used for the spatial discretization. The second-order upwind scheme is used for the density, momentum and energy. This scheme identifies the flow direction which influences the calculation and interpolates the flow quantities at the faces of cells based on the quantities calculated at the cell centers. The least squares cell based method is used for the gradients. This method calculates the gradients based on the assumption that the solution changes linearly between a cell and the neighboring cells. The second-order implicit scheme is used for the time discretization. This scheme is unconditionally stable. Details about these schemes can be found in Versteeg and Malalasekera [10].

In the structure solver, the experimental setup is simulated completely. The solid parts of the different components of the setup are represented as solid volumes (e.g prewinder, balloon). These solid parts are dimensioned and positioned as they are in the experiment and as shown in Figure 7.8. The total number of weft yarn nodes equals 9496.

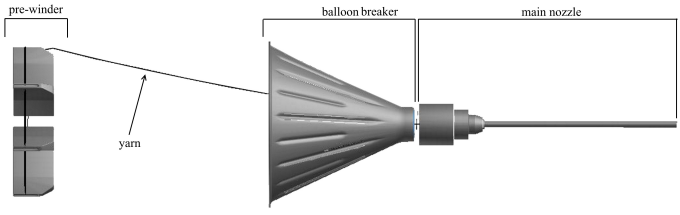

Figure 7.8: Overview of some solid parts as they are represented in the structure model and the initial position of the yarn.

Boundary and initial conditions: To validate the model all the conditions which are applied in the experiment are applied in the simulation. The computational fluid domain is shown in Figure 7.7(a). The fluid domain consists of three fluid zones. The first zone (blue color) represents the inlet zone which supplies the main nozzle with compressed air. The inlet boundary is 1.5 *m* upstream of the main nozzle. The second zone (black color) represents the main nozzle with the same dimensions as the one used in the experiment. The third zone (red colour) represents the atmosphere behind the nozzle. This zone extends up to 0.22 *m* after the tube's exit.

As mentioned above, the main nozzle is supplied with a low mass flow rate at the beginning of the experiment and the simulation. Afterwards, a total pressure of 5 bar is imposed at the inlet of the fluid domain. At the needle inlet and at the outlet, the static pressure is equal to the atmospheric pressure. All walls are no-slip walls, except for the yarn wall which is a slip wall with zero shear stress (see above). The time step which is used in the fluid simulation equals 0.1 *ms* and 500 time steps are carried out, resulting in one insertion. Sub-cycling was used for the structure as it uses a smaller time step. This means that several smaller time steps of the structural problem are performed for each time step of the fluid problem.

7.5 Results and discussion

7.5.1 Adjusting the aerodynamic force coefficients

Figure 7.9 shows the yarn speed at the exit of main nozzle A as a function of time. The yarn speed is calculated based on the measured length of the yarn which went out of the nozzle in the experiment and simulation. The horizontal time axis starts from zero which corresponds to the opening of the pin or releasing the yarn. At the beginning, the yarn is standing still. Then, when compressed air reaches the nozzle, the aerodynamic forces along the yarn start to increase and the yarn accelerates. The yarn reaches its maximum speed when the air flow is completely developed along it and the yarn speed becomes almost constant. The oscillations of the yarn speed, which are seen in the experiment as well as in the simulations, are due to collisions of the yarn with objects and tension of the yarn upstream of the nozzle. The nozzle inlet pressure is constant, so pressure oscillations in the supply line are not causing these changes in yarn speed.

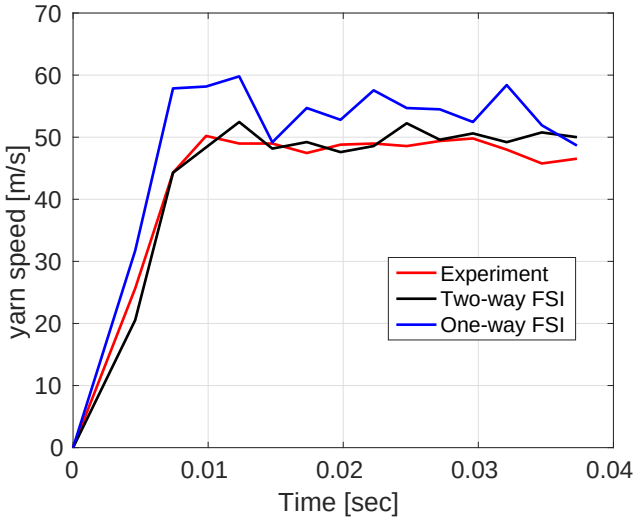

Figure 7.9: Yarn speed at the exit of main nozzle A as a function of time.

Figure 7.9 shows experiments, a one-way and a two-way simulation. As a first step, the aerodynamic force coefficients C_L and C_N have been tuned such that the two-way FSI simulation as described above is in good agreement with the corresponding experiment. Subsequently, additional two-way FSI simulations have been performed with these tuned coefficients as will be explained in the following paragraphs. Furthermore, Figure 7.9 shows that the yarn speed is higher in the one-way simulation than in the two-way simulation, with the coefficients tuned using two-way FSI simulations. This difference can be explained as follows. In the two-way FSI simulation, the source term represents the force which the yarn exerts on the air flow. This leads to a more correct flow field. The one-way FSI simulation

does not include the source term, which eliminates this interaction. This leads to higher velocities of the air flow, in turn resulting in higher aerodynamic forces and a higher yarn speed.

To verify the validity of the obtained force coefficients of the studied yarn, they are used with another main nozzle (nozzle B). Figure 7.10 shows the yarn tip position for both nozzles which were investigated. It is clearly seen in Figure 7.10 that the time for one insertion with nozzle A is shorter than with nozzle B, which means that the air flow is different. Notwithstanding the different air flow, the results of the simulation agree well with the experimental data for both main nozzles even though the force coefficients which have been tuned using nozzle A are also used for nozzle B. The yarn tip position with nozzle B is obtained using the two-way FSI simulation with a maximum error of *3.4%* in comparison to the one measured in the experiment. Therefore, the obtained force coefficients for the studied yarn are likely applicable for other main nozzles as well.

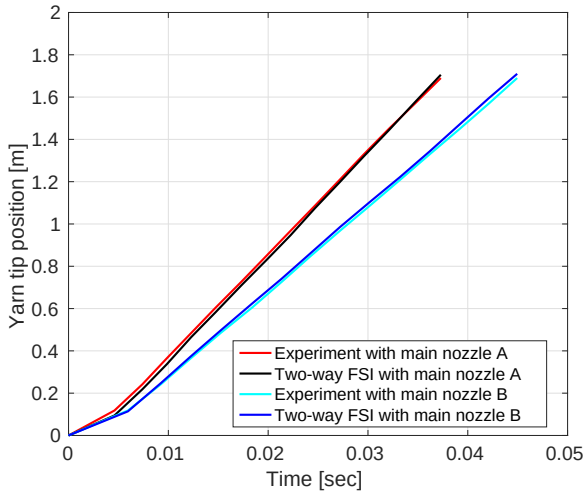

Figure 7.10: Yarn tip position with main nozzle A and B.

7.5.2 Validation of the models with nozzle A

The motion of the weft yarn is shown by frames which are taken from video recordings during the experiment. These frames are compared with the corresponding ones of simulation results (one-way and two-way FSI). The weft yarn can be seen in the recorded videos when it is moving, but it is difficult to discern when taking a single frame. This is due to the surrounding environment where the videos were recorded and due to others reasons such as yarn color, diameter and dust. To show the weft yarn clearly, the tube's border and the weft yarn have been traced carefully. Figure 7.11 shows the positions of the weft yarn at specific times for nozzle A. The time is counted starting at the opening of the pin when the yarn is released. The camera

view in the experiments corresponds to the *xy* plane in the simulation configuration and all results are presented in this plane.

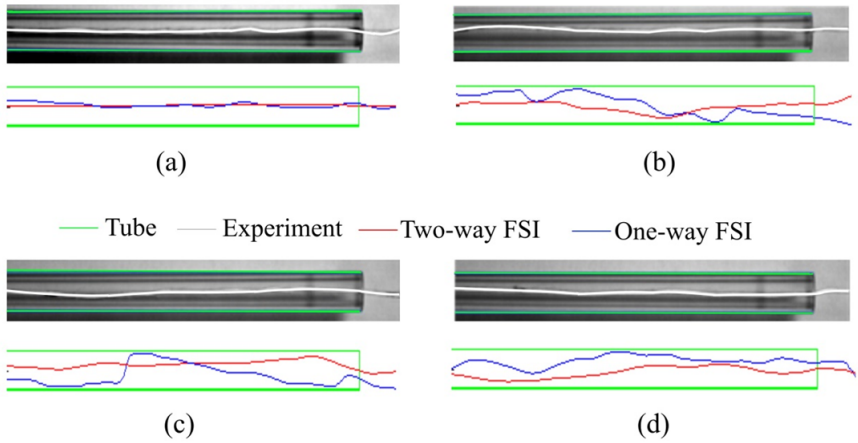

Figure 7.11: Frames of the weft yarn during experiments and the corresponding frames of the one-way and two-way simulations at the end of the tube at time: (a) 4.7 ms; (b) 14.9 ms; (c) 25.1 ms; (d) 35.3 ms. The length of the shown domain equals 143 mm and nozzle A has been used.

In Figure 7.11(a) the yarn is located almost at the axis of the nozzle in both the experiment and the simulation. In Figure 7.11(b), (c) and (d) the deviations of the weft yarn from the axis of the nozzle are seen in the experiment. In the same figures, the results of the two-way FSI show the deviations of the weft yarn with some differences in amplitude like in Figure 7.11(c), or direction like in Figure 7.11(d), whereas the results of the one-way FSI show completely different motions of the yarn in these figures. The one-way FSI simulation does not include the source term. This leads to different air flow and, therefore, important differences in comparison to the experiment are shown.

Another video of the motion of the yarn was recorded in the middle of the tube during the experiment with nozzle A. Figure 7.12 shows two frames of the experiment and simulation in the middle of the tube. The results of the two-way FSI are more accurate than the results of the one-way FSI in comparison to the experiment in these frames. The mode shapes of the weft yarn which are obtained with two-way FSI simulation agree well with those of the experiment.

Some differences between the results of the two-way FSI and the experiment are seen in Figure 7.11 and 7.12. There are many reasons which lead to these differences. The properties of the studied yarn are all measured and the flow field is calculated in two-dimensional configurations. Moreover, it is assumed, as mention before, that the starting position of the yarn is at the axis of the main nozzle. This assumption can be imposed in a simulation but not in reality. At the beginning of the experiments the main nozzle is supplied with holding flow which is assumed to keep the yarn at the axis but some deviations are inevitable. Although these deviations are small, they

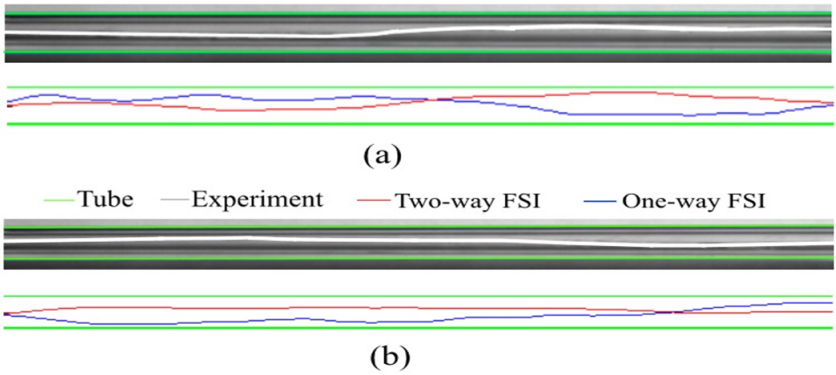

Figure 7.12: Frames of the weft yarn during experiments and the corresponding frames of the one-way and two-way FSI simulations in the middle of the tube at time : (a) 10.9 ms; (b) 28 ms. The length of the shown domain equals 142 mm and nozzle A has been used.

could cause, in addition to the other mentioned reasons, the observed differences between the simulation and experiments.

As mentioned above, the one-way FSI does not include the source term which affects the air flow. The source term represents the forces by the structure (the weft yarn) on the air flow. These forces are opposite to the aerodynamic forces. By consequence, the source term leads to a decreased velocity inside the nozzle. Figure 7.13 shows the contours of axial velocity inside the nozzle in a one-way and in a two-way FSI simulation. It is seen in Figure 7.13 that the axial velocity inside the nozzle in a one-way FSI simulation is higher than in a two-way FSI simulation.

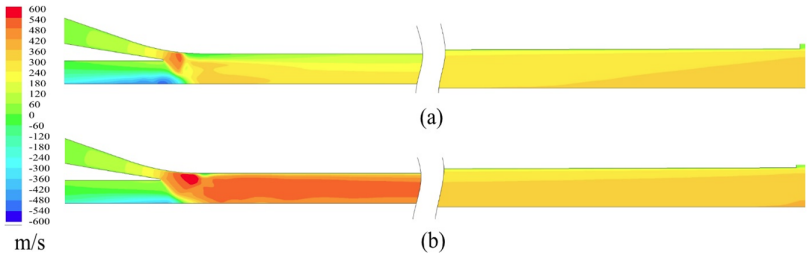

Figure 7.13: Contours of axial velocity inside nozzle A at 35.3 ms: (a) two-way FSI (with source term); (b) one-way FSI (without source term).

7.5.3 Validation of the models with nozzle B

From validating the models with nozzle A it can be deduced that the results of the one-way FSI simulation are not accurate. Moreover, there are some differences between the results of the two-way simulations and the experiments. Therefore, in

this section, only the results of the two-way FSI simulation will be compared with experiments using nozzle B. The characteristics of the deformation waves will be calculated and compared, with a deformation wave characterized by its length and speed.

Nozzle B generates a different flow field and, therefore, different yarn motion. Figure 7.14 shows the speed of the yarn as a function of time. The yarn reaches almost a steady speed after 0.01 s.

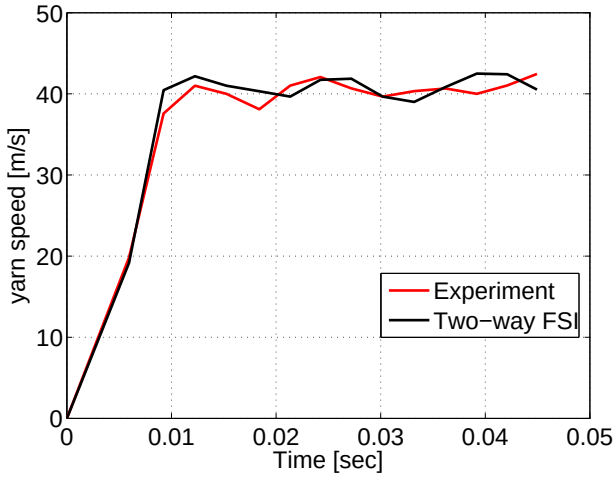

Figure 7.14: Yarn speed at the exit of main nozzle B as a function of time.

Figure 7.15 shows three frames taken from the recorded video with nozzle B. At the beginning, Figure 7.15(a), no deformation waves appear. After releasing the yarn, Figure 7.15(b) and (c), the deformations start to form and move along the weft yarn. The best way to measure the wave length and speed is to follow a complete wave in the experimental video, like this it is sure that the measured length and speed belong to the same wave.

For example, in Figure 7.15(b) the highlighted waves "wave 1" can be easily seen and its length can be measured. In Figure 7.15(c) the same wave "wave 1" is seen after traveling inside the tube with almost the same length. The wave speed is then calculated as

$$\text{wave speed}, c = \frac{\text{traveled distance}}{\text{time}} = \lambda \times f, \tag{7.16}$$

where λ is the wave length and f its frequency. By applying this formula to the seen wave in Figure 7.15 "wave 1"

$$c = \frac{(120-65)mm}{(1.7-1)ms} = 78.57m/s \Rightarrow f = \frac{78.57}{0.03} = 2619Hz. \tag{7.17}$$

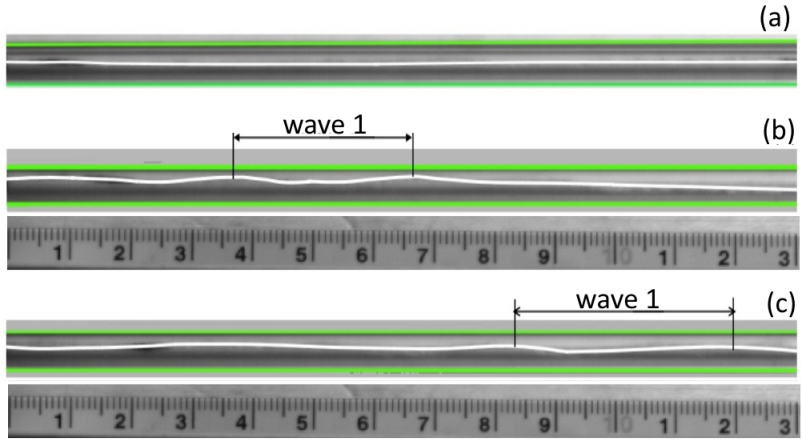

Figure 7.15: Frames of the weft yarn during experiments with nozzle B at time: (a) 0 ms; (b) 1 ms; (c) 1.7 ms.

Three waves are measured from the recorded video and the results are listed in Table 7.3. Moreover, the yarn speed is also measured with the same frames from which the waves are measured. The first two waves are taken from the first half of the nozzle tube and the third one is taken from the second half.

Table 7.3: Measured waves and yarn speed from the experiment.

Wave	Frame time [ms]	c [m/s]	λ[m]	f [Hz]	yarn speed [m/s]
1	1-1.7	78.57	0.03	2619	12.5
2	5.3-5.8	100	0.06	1666	38
3	20.4-21.0	108.33	0.06	1805	40

In the same way, the deformation waves of the simulation are measured. The deformation waves of the simulation at the first 5 ms are with lower amplitudes in comparison to the experimental ones. Figure 7.16 shows the first wave which appears in the simulation. However, after 5 ms the deformation waves are clearly seen in the simulation frames as shown in Figure 7.17. Table 7.4 lists three measured waves taken from the simulation. The second and the third waves are taken at the same time of the experiment and the simulation, while the first wave is taken as the first one which appears at the beginning of the simulation and the experiment. Moreover, the yarn speed in calculated in the part of the tube where the waves are measured.

It can be seen from Table 7.3 and 7.4 that there are differences between the characteristics of the waves of the simulation and the experiment. However, it is difficult to measure precisely the waves in the recorded video. The speed of the waves c might be the only characteristic which can be measured accurately form the recorded video. The third column in Table 7.3 and 7.4 show that the differences between the simulation and the experiment decrease with time. The high differences at the

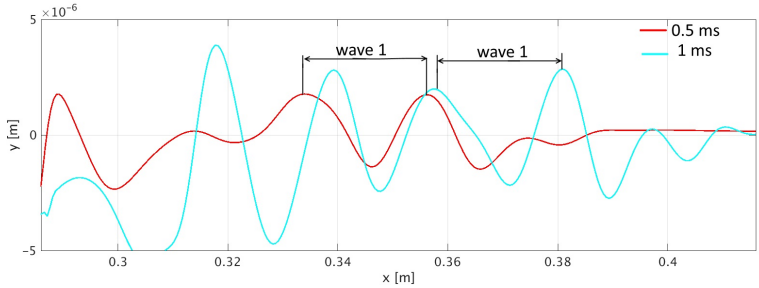

Figure 7.16: The first deformation wave of the simulation with nozzle B.

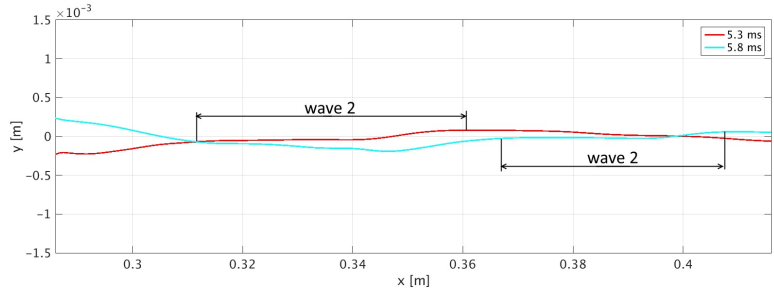

Figure 7.17: A deformation wave of the simulation with nozzle B after 5 ms.

beginning of the simulation might be due to a different initial position of the yarn. Moreover, in the simulation, the inlet pressure of 5 bar is applied at once after the low mass flow, whereas, in the experiment, the pressure was increased in very short time to 5 bar. This may lead to some differences at the beginning. In other words, after the flow has been fully developed inside the main nozzle, the results of the simulation are close to the experiment. The measured yarn speeds which are listed in the last column in Table 7.3 and 7.4 are not the same as the ones shown in Figure 7.14 because they are measured in different locations. However, the same conclusion related to the wave speeds can be drawn with these yarn speeds. Moreover, a different yarn speed affects the deformation waves, especially during the acceleration stage because the speed affects the acceleration which results in different inertial forces.

After validating the models with nozzle A and B it can be said that, with the studied yarn, the models succeed in predicting accurately the speed of the yarn during the simulations. However, the deformation wave characteristics of the simulations may not be equal to the ones of the experiment with high differences at the beginning of the insertion time and small differences at the end.

7.5.4 Yarn motion with nozzle A and B

The geometries of nozzle A and B are different as can be seen in Table 7.2. The most important difference is that nozzle A has a conical tube, while nozzle B has a cylindrical tube. From Figure 7.10 it can be seen that, as the time for one insertion is

Table 7.4: Measured waves and yarn speed from the simulation with nozzle B.

Wave	Frame time [ms]	c [m/s]	λ[m]	f [Hz]	yarn speed [m/s]
1	0.5-1	51	0.023	2170	10.47
2	5.3-5.8	118.4	0.05	2368	33.68
3	20.4-21.0	109.1	0.088	1239	41.21

shorter with nozzle A, the speed of the weft yarn is higher with nozzle A than with nozzle B. The higher speed of the weft yarn is due to higher aerodynamic forces. However, it is interesting to investigate the effects of the geometry on the motion of the yarn. The simulations with nozzle A and B are performed with identical conditions. Therefore, any differences in the motion of the yarn are due to geometrical changes which affect the air flow.

The motion of the studied yarn inside both nozzles is unstable which means that deformation waves are generated during the insertion. Therefore, investigating the mode shapes of the yarn would not lead to clear conclusions about the geometrical effects on the motion of the yarn. To analyze the effects of the nozzle geometries on the motion of the yarn three points inside the tube are chosen. The three points are located next to the needle tip in the mixing region, at the tube center and at the tube exit. The y-coordinates of the yarn in the chosen points will be plotted and investigated.

Figure 7.18 shows the y-coordinates of the yarn in the three chosen points during the insertion with nozzle A and nozzle B. Figure 7.18(a) shows that both nozzles generate strong deformations in the mixing region. Strong deformations means that the peaks (crests) of the deformations are close to each other. Moreover, there is almost as many peaks with nozzle A as with nozzle B. In fact, in the mixing region shocks always occur and thus the normal force is not zero due to the pressure gradients which change along the shocks, except when the shock is perpendicular to the yarn. Moreover, the velocity gradients also affect the normal forces as the air flow velocities are calculated based on linear interpolation. Figure 7.19(a) shows that the dominant frequency of the y-coordinates for the point in the mixing region is almost the same with nozzle A and nozzle B. There are two important peaks with nozzle B and the values of the dominant frequency is around 775 Hz. The amplitudes of the deformation waves increase by propagating downstream as shown in Figure 7.18(b) and (c). The dominant frequencies of the deformation waves at the center of the tube with nozzle A and nozzle B are close to each other (about 145 Hz) but they are not at the tube exit where the dominant frequency with nozzle A (175 Hz) is higher than with nozzle B (58 Hz).

By comparing the deformation waves along y with nozzle A and nozzle B it can be said that both nozzles generate almost the same deformations along y but with nozzle A the deformations at the exit of the nozzle are stronger and with higher amplitudes. The higher amplitudes are allowed by a larger tube exit diameter (33% larger with nozzle A than with nozzle B). The deformations of the yarn at the tube exit may affect the subsequent step of the weaving but this has not been studied in this work. The most important is the yarn speed which is higher with nozzle A than

with nozzle B.

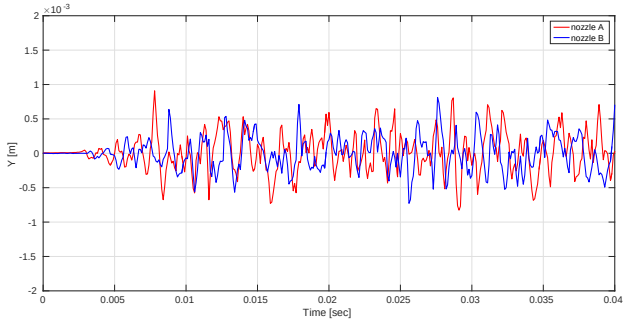

(a)

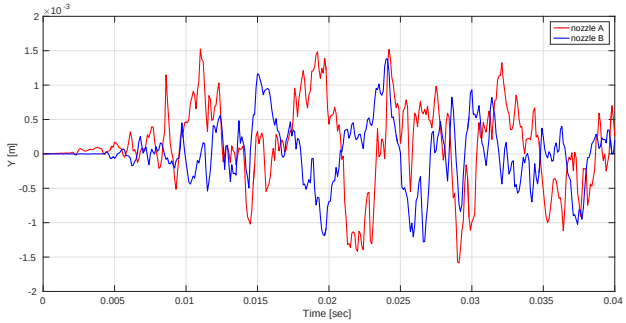

(b)

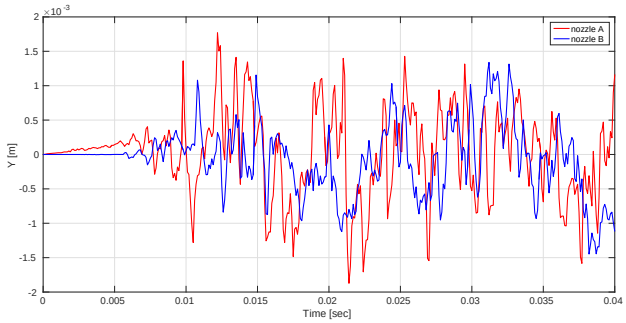

(c)

Figure 7.18: Yarn y-coordinates during the insertion time with nozzle A and B: (a) Point in the mixing region; (b) point at the tube center; (c) point at the tube exit.

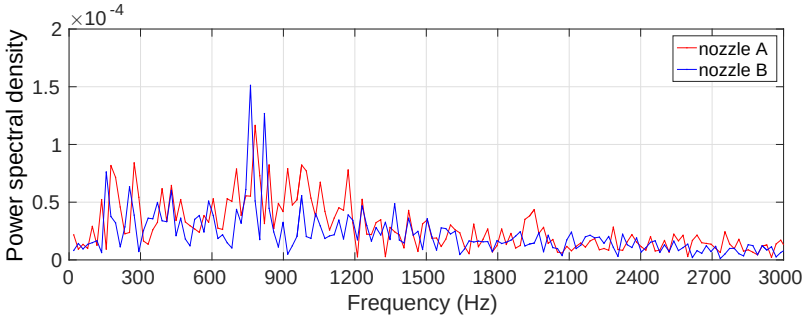

(a)

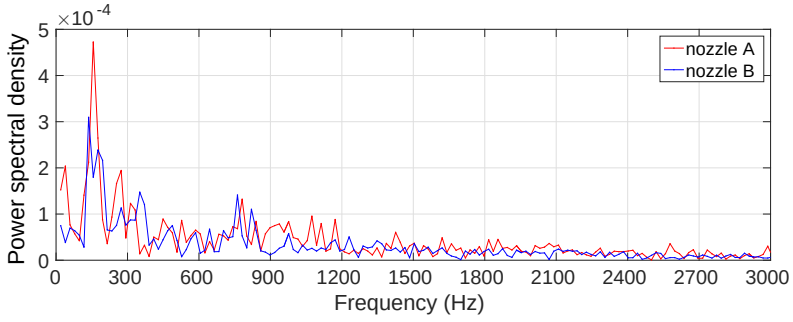

(b)

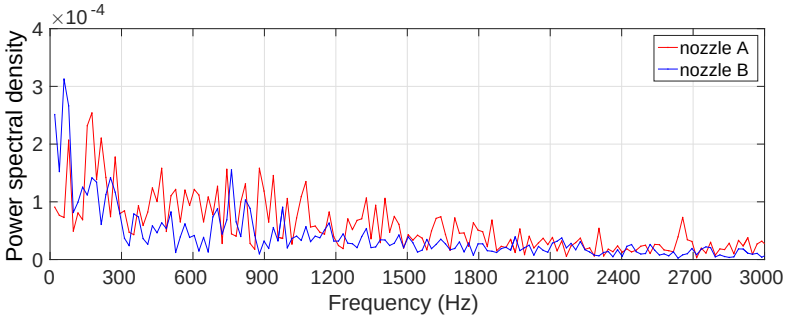

(c)

Figure 7.19: Power spectral density of the yarn y-coordinates with nozzle A and nozzle B: (a) Point in the mixing region; (b) point at the tube center; (c) point at the tube exit.

7.6 Conclusion

In this chapter, one-way and two-way FSI simulations of air flow-yarn interaction inside two different main nozzles of an air jet loom have been carried out. A three-dimensional structure model of the flexible weft yarn, consisting of a chain of line segments has been employed to calculate deformations of the weft yarn as a flexible body. The fluid model is two-dimensional axisymmetric. The results of the numerical

simulations have been compared with experimental data and recorded videos. The force coefficients have first been tuned to obtain good agreement between the simulation and the experiments for nozzle A. Afterwards, it has been demonstrated that these same coefficients give good agreement between simulation and experiment of nozzle B as well. The one-way FSI simulation type shows different yarn motion due to the inaccurately calculated air flow. After validating the two-way FSI model it can be said that the aerodynamic, contact, bending and tensile forces are sufficiently calculated. The difference in yarn tip position between the simulation and the experiment was less than 4%. Furthermore, the two-dimensional axisymmetric air flow simulation succeeds in giving good results at moderate cost with regard to a three-dimensional flow simulation.

The yarn motion has been compared with two nozzles, the yarn speed is higher with one of them than with the other. It has been found that the deformation amplitudes and frequencies are almost the same with the two nozzles. Therefore, it can be deduced that the radial deformations cannot be avoided and thus it is recommended to disregard them when designing a new main nozzle geometry because they are always generated during the insertion.

The most important conclusion of this work is that these numerical models can be used to optimize the geometry of the main nozzle. The two main factors which are important to evaluate a new main nozzle are the yarn's speed and the potential of yarn breakage due to the high tensile forces. These two factors can be extracted from simulations with these models.

Employing the proposed models to study the motion of another yarn involves first finding the aerodynamic force coefficients. This step might limit the models because it involves several simulations to find the correct values of the coefficients. Moreover, the effect of the hairiness of the yarn needs to be investigated. However, eliminating the problem associated with the dynamic mesh in the proposed procedure by using a source term makes employing the models straightforward to study the motion of different yarns in a main nozzle and their interaction with the main nozzle flow.

Chapter 8

Fluid-structure interaction simulations of air flow-yarn interaction with dynamic mesh

In this chapter, fluid-structure interaction simulations with dynamic mesh of air flow-yarn interaction inside a main nozzle of an air jet loom will be presented. In this type of FSI simulation, the fluid grid is updated in each time step according to the new positions of the fluid-structure interface.

This chapter starts with an introduction about the studied case. Then, the experiment is presented followed by the simulation's setup. Finally, the deformation waves which are obtained from the simulations are compared to those of the experiment.

8.1 Introduction

In the previous chapter, the results of one-way and two-way FSI simulations with fixed mesh have been presented. The effects of the structure motion on the fluid flow have been added by a source term. The aerodynamic forces have been calculated based on coefficients. Moreover, the tensile and the contact forces have been modeled. The advantages of those simulations and models are many. For example, with the proposed procedure, it has been possible to model the motion of a yarn inside a main nozzle for one insertion, the problems with the dynamic mesh have been avoided and the computational time of the simulation is low. However, the flow calculation was two-dimensional axisymmetric and the use of aerodynamic coefficients in non-uniform flow is a simplification, although a correction term for the pressure gradient was introduced. In this chapter, the motion of a yarn in air

flow will be studied by performing three-dimensional FSI simulations with dynamic mesh. However, the representation of the yarn surface needs to be simplified.

Performing FSI simulations with dynamic mesh of air flow-yarn interaction in a main nozzle involves employing a specific method to handle the fluid and the structure grids. The axial motion of the weft yarn implies that the grids have to be changed or adapted in each time step to take into account the length of the yarn which enters or exits the calculation domains. Moreover, two-dimensional axisymmetric simulations of the air flow cannot be done with FSI simulations with dynamic mesh. Employing the dynamic mesh implies three-dimensional simulations of the air flow which increases the duration of the simulations, especially if a complete insertion is studied. Therefore, only the first stage of the weft yarn motion is considered in this chapter.

The motion of the weft yarn in an air jet loom can be divided into two stages. In the first stage, the weft yarn is clamped and flow is built up in the main nozzle. In the second stage, the yarn is released and accelerated. In the previous chapter, the second stage is modeled and studied for a cotton yarn and in this chapter, the first stage will be analyzed. This means that the motion of a clamped-free yarn will be studied, the yarn is fixed at one side and it is free at the other side.

Experiments of a clamped-free cotton yarn have not been conducted. The available experiments are with a nylon yarn. Moreover, even if experiments were carried out with a cotton yarn, it would be difficult to perform FSI simulations with dynamic mesh with such a highly flexible yarn.

The motion of a clamped-free nylon yarn was studied numerically by Hertens [146]. The geometry of the main nozzle which was used in that work was the same as the geometry of nozzle A presented in the previous chapter. The studied yarn was a nylon 6.6. Many numerical parameters and effects have been investigated, for example the difference between using an implicit or explicit coupling algorithm. It has been found that a strongly coupled algorithm (implicit) gave different yarn positions in comparison to a weakly coupled algorithm (explicit) after 4.07 ms as shown in Figure 8.1. The reason of these differences was explained by the effects of strong shock waves. As the equilibrium conditions on the fluid-structure interface are not satisfied with an explicit algorithm, the results of the implicit algorithm are more accurate for the studied case. However, the gravity of the yarn was ignored in that work. Moreover, the obtained deformation waves were excited at the beginning of the simulations. A sine wave with a small amplitude had been imposed as initial condition.

By consequence, by including the gravitational force of the yarn and without imposing any initial deformations in this work, the simulation setup will be closer to the experiments and this may give better results. In the following sections, the experiment and the simulation setup will be presented in detail.

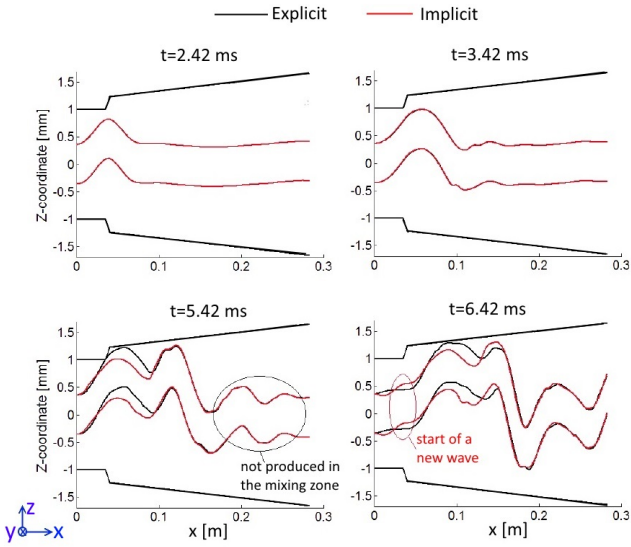

Figure 8.1: Yarn positions in the xz-plane at different times with implicit and explicit coupling algorithms, taken from [146]. The coordinate system which was used in the simulation is as shown where the x-axis is along the yarn and the xz-plane is the horizontal plane. The top and bottom lines are the main nozzle tube, while the two middle lines delineate the yarn.

8.2 Experiment

The experiment is carried out by Picanol. The experiment is carried out with the same geometry of nozzle A presented in the previous chapter. The motion of a nylon 6.6 monofilament yarn has been recorded by a high-speed camera. The properties of this yarn are measured experimentally: the diameter is equal to 0.72 mm, the density $\rho_{yarn} = 1140\,kg/m^3$ and the Young modulus $E = 2.5\,GPa$. The yarn is clamped at the yarn inlet and it is free at the exit of the tube. At the beginning of the experiment, the main nozzle is supplied with a holding flow pressure. Then, the supply pressure increases to 5 bar (relative to the atmospheric pressure). The inlet of the supply pressure is upstream of the main nozzle, but the pressure at the inlet of the main nozzle is measured during the experiment. Figure 8.2 shows the measured pressure profile at the inlet of the main nozzle. The initial pressure corresponds to the pressure of the holding flow, equal to 0.14 bar. After 5.4 ms, the valve is opened and the pressure increases sharply to 5.35 bar. This value is higher than the inlet pressure, which is equal to 5 bar. This higher value is due to pressure waves between the inlet of the supply pressure and the inlet of the main nozzle. From 18 ms to 57 ms the pressure varies between 4 bar and 5 bar. Afterwards, The pressure reduces back to 0.14 bar.

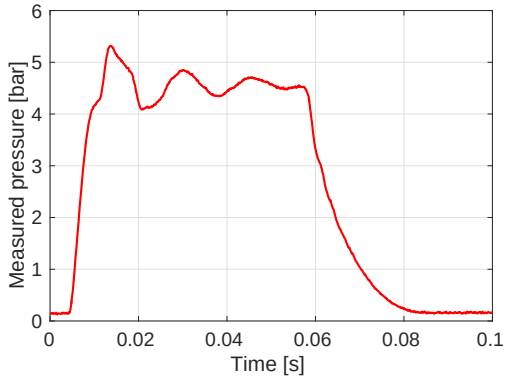

Figure 8.2: Measured pressure profile at the inlet of the main nozzle during the experiment. The values are relative to the atmospheric pressure.

The motion of the yarn is recorded during 0.1s in two parts of the nozzle tube shown in Figure 8.3. The holding flow is already blowing at the beginning of the video recordings. This can be seen in Figure 8.2 in which the measured pressure at zero time corresponds to the holding flow pressure.

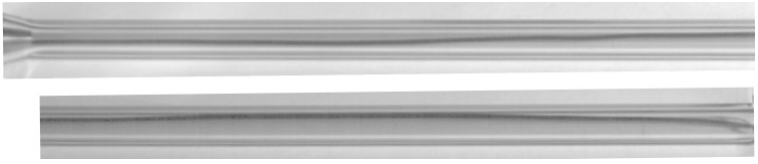

Figure 8.3: Yarn positions (black color) at the beginning of the recordings: (a) the first part of the tube; (b) the second part of the tube, at the tube exit the yarn is free.

8.3 Simulation setup

8.3.1 Flow solver

The computational fluid domain which is three-dimensional consists of the main nozzle geometry and two additional outer zones as shown in Figure 8.4(a). The yarn is represented as a cylinder whose diameter is equal to the yarn diameter 0.72 mm inside the main nozzle and the outer zone on the left. Representing the yarn inside the outer zone on the left is just for meshing consideration to avoid a high number of cells in this region. However, the yarn is clamped at the yarn inlet shown in Figure 8.4(a). At the exit of the tube, the yarn is free. The mesh is structured, as it can be seen in Figure 8.4 (b), and it contains about 200000 cells. The coordinate system is shown in Figure 8.4(a).

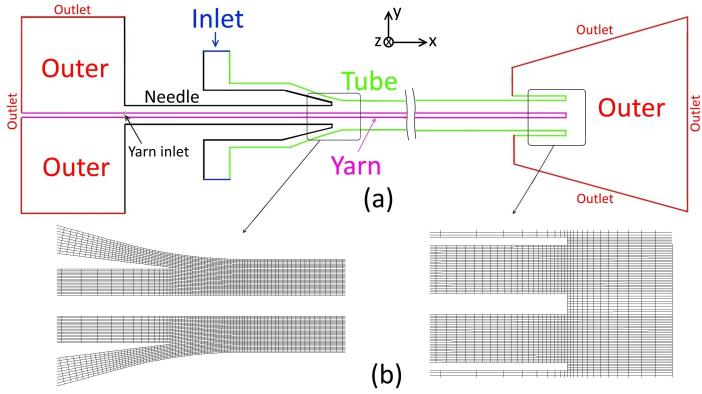

Figure 8.4: (a) Meridional view of the computational fluid domain with the boundary conditions; (b) Details of the mesh.

As the mesh is dynamic, the arbitrary Lagrangian-Eulerian (ALE) formulation of the flow equations are solved [147, 148]. The air flow is compressible and turbulent and the k-ω SST has been used as the turbulence model.

The three-dimensional transient simulations of the air flow have been performed using Ansys Fluent 17.0 in which the coupled scheme is used as solution method for pressure and velocity. The second-order upwind scheme is used for the density, momentum and energy. The least squares cell based method is used for the gradients. The second-order implicit scheme is used for the time discretization.

Several methods can be used to handle the dynamic mesh. Two of these methods are available in Ansys Fluent 17.0 which are smoothing and remeshing. The remeshing method can only be employed with an unstructured mesh which is not applicable to the studied case. The smoothing method is applicable with a structured and an unstructured mesh and it is employed with the studied case. Furthermore, the principle of the smoothing method is to extend the displacements of the fluid-structure interface to the surrounding fluid domain. The Laplacian (diffusion) technique is used here for the extension of the grid displacements. This technique is based on a diffusion equation to calculate the new positions of the grid nodes. For more details about this technique, see [149].

Boundary and initial conditions: The boundary conditions are set as follows: the inlet condition is pressure equal to the measured pressure profile shown in Figure 8.2. The outlet condition is pressure equal to the atmospheric pressure. The wall of the needle, tube and yarn are set to no-slip walls.

As mentioned above, at the beginning of the experiment the holding flow is already blowing. Therefore, at the beginning of the FSI simulation the initial values of the air flow quantities correspond to values obtained with 0.14 bar inlet pressure. The yarn initial position is at the axis of the main nozzle. The convergence tolerances are set to 10^{-6} for all flow quantities.

8.3.2 Structure solver

The structural computational domain is shown in Figure 8.5. It consists of the yarn as a cylinder and the tube of the nozzle (the fictive tube). The cylinder length is 0.28 m. The structured mesh of the cylinder contains 4800 elements of type $C3D20R$. C stands for continuum elements which are used for solid analysis, $3D$ means three-dimensional, 20 is the number of nodes and R stands for reduced-integration which reduces the number of integration points to calculate element matrices. The properties of the cylinder are set to those of the yarn which are: density $\rho_s = 1140\,kg/m^3$, Young modulus $E = 2.5\,GPa$ and Poisson's ratio $\nu = 0.39$. Neither displacements nor rotations are allowed at the fixed end of the yarn.

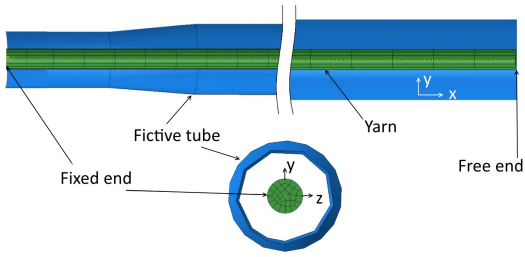

Figure 8.5: Computational structural domain.

The tube or the fictive tube which is shown in Figure 8.5 is not a meshed body, it is set as an analytical rigid body. The idea of this body is to prevent the yarn to move out of the main nozzle. Moreover, the diameters of this fictive tube are smaller than the corresponding diameters of the tube in the fluid domain for dynamic mesh considerations. The smoothing method is used to handle the dynamic mesh, thus when the cylinder will deform in the radial direction, the cells in the fluid domain will move in the same direction. Therefore, smaller tube diameters are necessary to avoid problems with the dynamic mesh like contact and negative volume cells i.e. a cell where one corner has been pushed through a face connecting other corners of this cell. The length of the fictive tube in the structural domain is equal to the length of the tube in the fluid domain, while its diameters are smaller by 15%, $D_{fictive\,tube} = 0.85 D_{real\,tube}$. Frictionless contact is set between the cylinder and the fictive tube in the tangential direction and hard contact in the normal direction.

The structure equation, Equation (2.7), is discretized with the finite element method. The Hilber-Hughes-Taylor implicit time integration method is used. The geometrical nonlinearity is taken into account. Additionally to the fluid loads which are pressure and viscous traction, the gravity is also included in the structure calculations. The three-dimensional structural implicit dynamics have been calculated using Abaqus 6.14 (Simulia Inc., Providence, RI, USA).

8.3.3 Coupling algorithm

The fluid-structure interaction simulations have been performed with partitioned codes. The air flow calculations are strongly or implicitly coupled with the structural

calculations and the interface Quasi-Newton technique with an approximation of the inverse of the Jacobian from a least-squares model (IQN-ILS) [150] has been used. With an implicit coupling algorithm, the coupling equilibrium conditions (Equations (2.9) and (2.10)) are satisfied in each time step. The relative convergence tolerance is set to 10^{-6} with a maximum number of coupling iterations equal to 20. However, after a few time steps, three coupling iterations were sufficient to reach the imposed convergence tolerance.

8.4 Remarks

Similar simulations have been discussed in the work of Hertens [146]. An important conclusion from that work is about the dynamic mesh. When the inlet pressure was raised, deformation waves ran along the yarn. Those waves reached relatively high amplitudes. Therefore, the mesh was distorted during the simulations. The yarn end with sharp edge rendered the problem more complex. Eventually, the flow solver stopped due to mesh problems, such as, negative cell volumes. Therefore, in this chapter the possibility of solving the problems with the dynamic mesh or the possibility of increasing the total time of the simulations is investigated.

As mentioned before, the remeshing method of the dynamic mesh is not used here due to the high number of cells which is required with an unstructured mesh to preserve good mesh quality. A high number of cells increases significantly the duration of the simulation. Therefore, a structured mesh is constructed and the smoothing method has been used. The spring-based smoothing method was used by [146], while the Laplacian smoothing method is used in this work. The spring-based method extends the displacements of the fluid-structure interface by considering the mesh edges as springs, while with the Laplacian smoothing method the extension is done based on the solution of the Laplace equation.

An explicit coupling algorithm has not been used in this work and the implicit one is just used. No comparison between the results of this work and the results of [146] will be presented as the simulation's setup is different.

8.5 Results and discussion

8.5.1 Time step effects

The effects of two time step sizes on the results are investigated. The time step with FSI simulations has multiple effects. It affects the air flow simulations, the structure simulations and the dynamic mesh. Figure 8.6 shows three frames of the yarn positions with time step size $\Delta t = 1 \times 10^{-5} s$ and $\Delta t = 5 \times 10^{-6} s$. The obtained positions of the yarn in Figure 8.6(a) and (b) are the same with the two time step sizes. However, some differences are seen in Figure 8.6(c), especially at the needle tip where with $\Delta t = 1 \times 10^{-5} s$ a wave is seen to start at the beginning of the tube but it is not seen with $\Delta t = 5 \times 10^{-6} s$.

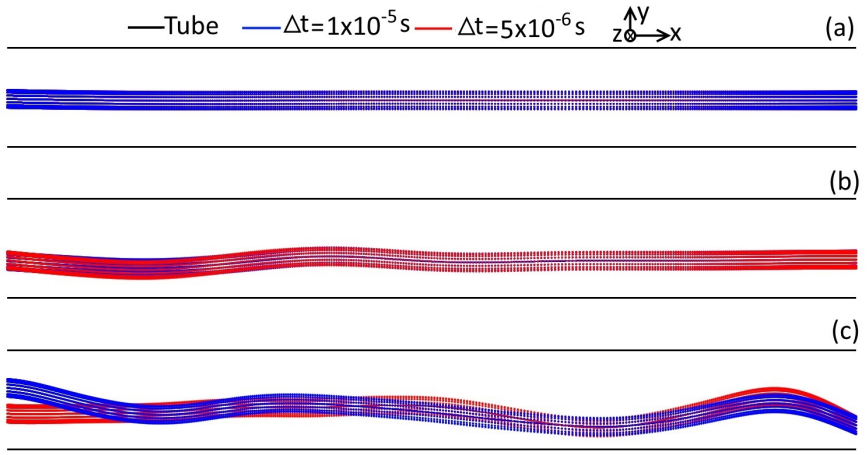

Figure 8.6: Frames of the yarn positions in the xy-plane at time: (a) 5 ms; (b) 10 ms; (c) 15 ms. The domain shown is from the needle tip to the tube exit.

To investigate further the effects of the time step size, Figure 8.7 shows coordinates of three points taken from the yarn centerline at three locations: close to the needle tip, at the tube center and at the yarn end. It can be seen in Figure 8.7(a) that the differences between the results of the two time step sizes start in the z-coordinate at 0.01 s, while at the same time the y-coordinates are almost the same with the two time step sizes. However, differences in the y-coordinate are seen later. In Figure 8.7(b) and (c) the y-coordinates are almost the same but the z-coordinates are with the same absolute values but in the opposite direction. The motion in the y-direction is influenced by gravity, while the instability in the z-direction seems to be triggered by numerical perturbations.

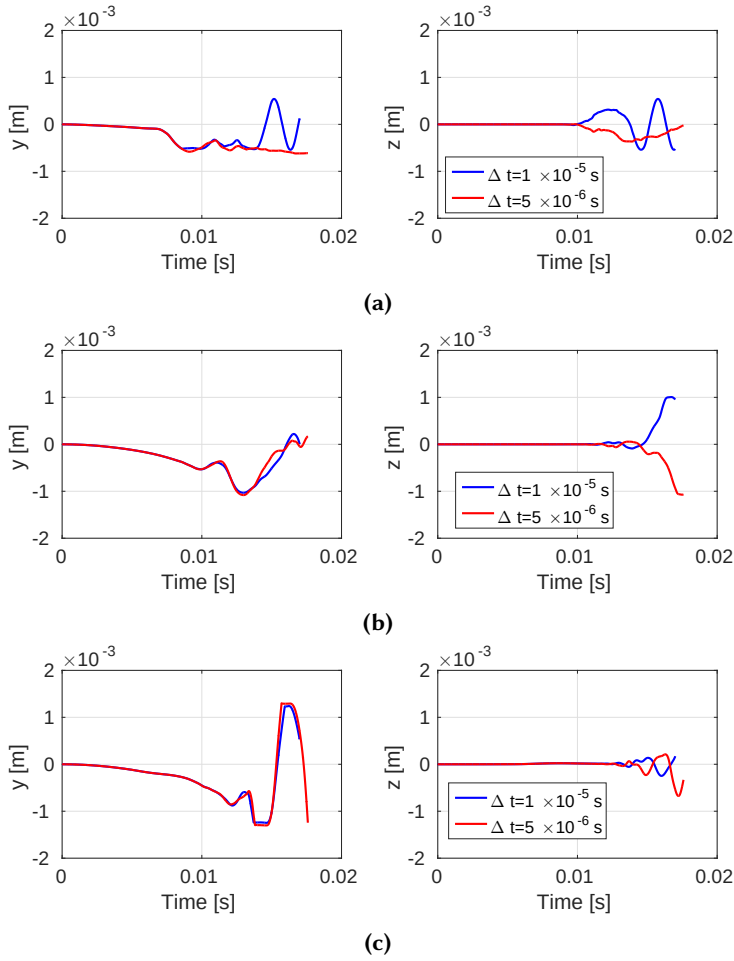

Figure 8.7: Yarn point coordinates during the simulation: (a) Yarn point close to the needle tip (mixing region); (b) Yarn point close to the tube center; (c) Yarn end.

The total time of the simulation which has been performed is almost the same with the two time step sizes and both simulations ended due to excessive mesh distortion. This means that mesh distortions could not be avoided by reducing the time step size. The reason can be seen in Figure 8.7(c) in which the y-coordinates of the yarn end are high. These high deformations combined with the sharp edge distort the mesh around the free end. Eventually, the flow solver stopped due to problems with the mesh, for example negative cell volumes. Figure 8.8 shows a part of the mesh in the xy-plane at the end of the simulation with $\Delta t = 5 \times 10^{-6} s$. It can be seen that high distortion is present around the yarn free end. No other time step sizes have been tested.

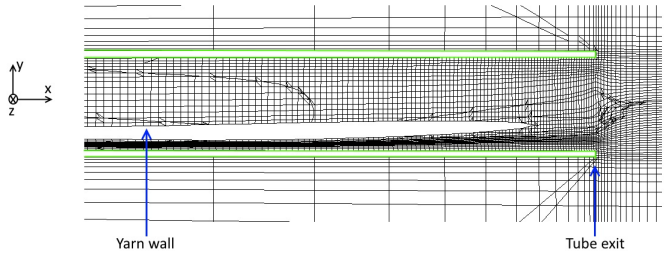

Figure 8.8: Distorted mesh in the xy-plane at the end of the simulation with time step size $\Delta t = 5 \times 10^{-6} s$. The green lines are the tube borders and the length of the domain shown is equal to 25 mm.

8.5.2 Mesh effects

The results of the simulations should be independent of the meshes. The fluid mesh has effects on the results but it has effects on the dynamic mesh motion. Refining the fluid mesh improves the simulation results but it increases the difficulty with the dynamic mesh motion as the smoothing method is used. To investigate whether the results are independent of the mesh or not, the fluid mesh which is shown in Figure 8.4(b) is refined in the circumferential direction as seen in Figure 8.9. The effects of refining the mesh on the air flow field are shown in Figure 8.10. Inside the main nozzle, the most sensitive region to mesh refinement is the mixing region where the shocks occur. Therefore, any change in the mesh affects the air flow quantities in the mixing region. This is clearly seen in Figure 8.10 in which the static pressure along the wall of the yarn is plotted. Refining the mesh downstream the mixing region does not affect the air flow that much. However, in Figure 8.10 the yarn is at the axis of the nozzle but during the FSI simulation the yarn will deform and refining the mesh may affect the results.

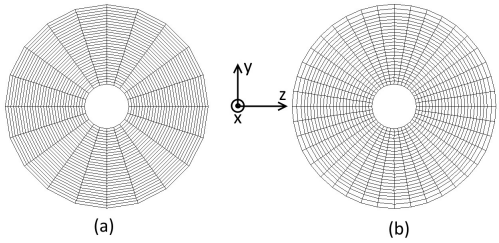

Figure 8.9: Mesh in the yz-plane: (a) Mesh 1; (b) Mesh 2.

Figure 8.11 shows three frames of the yarn centerline positions in the xy-plane. The coordinates of the yarn centerline are plotted instead of the complete yarn. It is clearly seen in Figure 8.11 that refining the mesh affects the obtained positions of the yarn. The differences might be caused by the effects of the mesh in the mixing region. More precisely, in Figure 8.10 it has been seen that the static pressure on

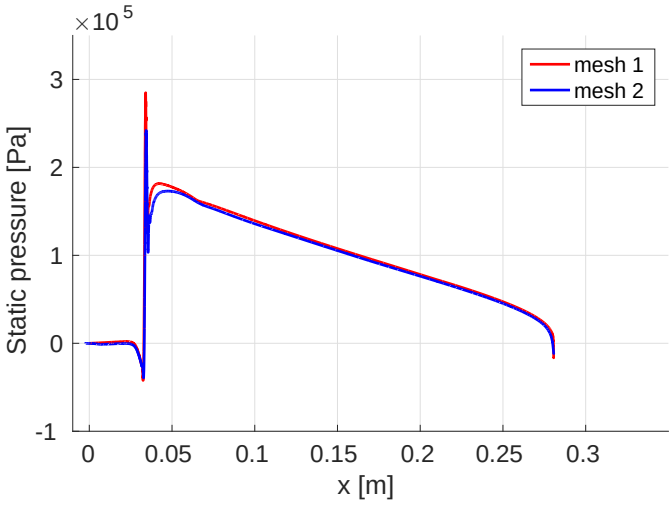

Figure 8.10: Static pressure along the yarn with 5 bar inlet pressure, mesh 2 is finer than mesh 1.

the yarn wall in the mixing region is affected by refining the mesh. Therefore, the force on the yarn in the mixing region will be different with mesh 1 than with mesh 2 which results in different deformation amplitudes. The deformations of the yarn end is also affected by mesh refinement as can be seen in Figure 8.11(c).

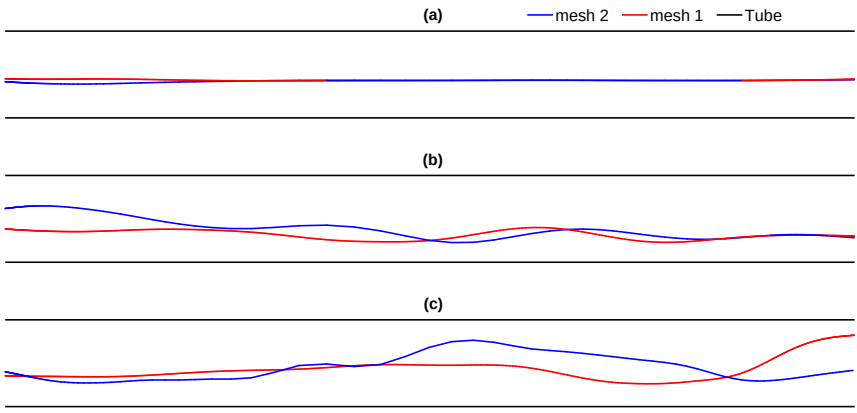

Figure 8.11: Yarn centerline positions in the xy-plane at time: (a) 7.5 ms; (b) 12.5 ms; (c) 16 ms. The domain shown is from the needle tip to the tube exit. The simulations with the two meshes (mesh 2 is finer than mesh 1) are performed with the same time step size $\Delta t = 5 \times 10^{-6} s$.

The FSI simulations with mesh 1 and mesh 2 are performed with the same time

step size which is equal to $\Delta t = 5 \times 10^{-6} s$. The total performed time steps with mesh 1 and mesh 2 is almost the same. To investigate the mesh effects as well as the time step effects it would be much better to compare the results over a longer period which is not possible due to mesh distortions. No further investigations of time step and mesh effects have been made. The results of the FSI simulations with mesh 2 and with time step $\Delta t = 5 \times 10^{-6} s$ will be analyzed and compared to the experiments.

8.5.3 Comparison with the experiments

To validate the results of the simulations, they are compared to the experiments. First, frames which are taken from video recordings during the experiment and the corresponding ones from the simulations are shown. Second, the characteristics of the deformation waves are calculated and compared.

Figure 8.12 shows the positions of the yarn in three frames. The yarn in the first frame of the simulation, Figure 8.12(a), is at the axis of the nozzle, while in the experiment, the yarn is not at the axis. The corresponding inlet pressure with this frame is less than 1 bar. The video recordings show that the position of the yarn is almost the same from the beginning of the video recordings to 5.4 ms. This means that the air flow has not deformed the position of the yarn from 0 ms to 5.4 ms, the air flow just holds the yarn in the same position. At the beginning of the simulation, the yarn is at the axis of the nozzle and after 5.4 ms the position of the yarn has not changed that much. Therefore, the response of the yarn to the air flow excitements is the same in the experiment and in the simulation during the first 5.4 ms. The difference is just in the initial position of the yarn.

The different initial position of the yarn in the simulation with regard to the experiment affects the subsequent positions. However, Figure 8.12(b) shows that the deformations seen in the experiment and in the simulation belong to one deformation wave, whereas in Figure 8.12(c) the deformations belong to more than one wave. Comparing exactly the position of the yarn in Figures 8.12 (b) and (c) is not applicable as the initial position is not the same.

Figure 8.13 shows three frames of the yarn position in the second half of the tube. Figure 8.13(a) shows the position of the yarn at 5.4 ms. Also in this part of the tube, the position of the yarn has not changed from the beginning of the video recordings during the experiment to 5.4 ms. Increasing the inlet pressure of the nozzle forces the yarn to move back to the axis of the main nozzle as shown in Figure 8.13 (b). Then, the deformation waves move along the yarn as can be seen in Figure 8.13(c).

The characteristics of the waves are measured and calculated as shown in Figure 8.14. A point from a wave is chosen to be followed. That point has to be either a crest or a trough. As the wave is moving inside the tube, thus following the chosen point from a crest or a trough can be done. For example, in Figure 8.14 point A from the chosen wave is followed, the wave speed is calculated according to $c = \triangle x_A / \triangle t$ with $\Delta x_A = x_{A,\,frame2} - x_{A,\,frame1}$ and $\Delta t = t_{frame2} - t_{frame1}$. The wave length is taken directly from the frame as shown in Figure 8.14(a). In the same way, three

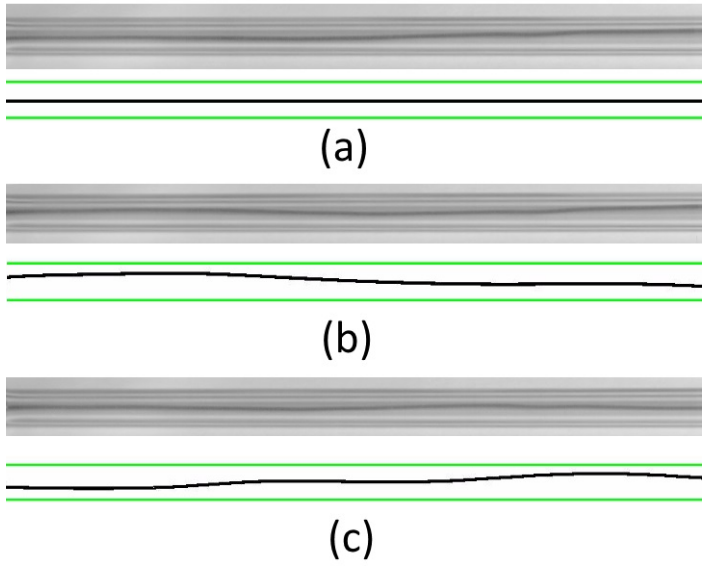

Figure 8.12: Frames of the yarn during experiments and the corresponding frames of the simulations at time: (a) 5.4 ms; (b) 13.4 ms; (c) 15.4 ms. The domain shown starts from the needle tip to 130 mm downstream.

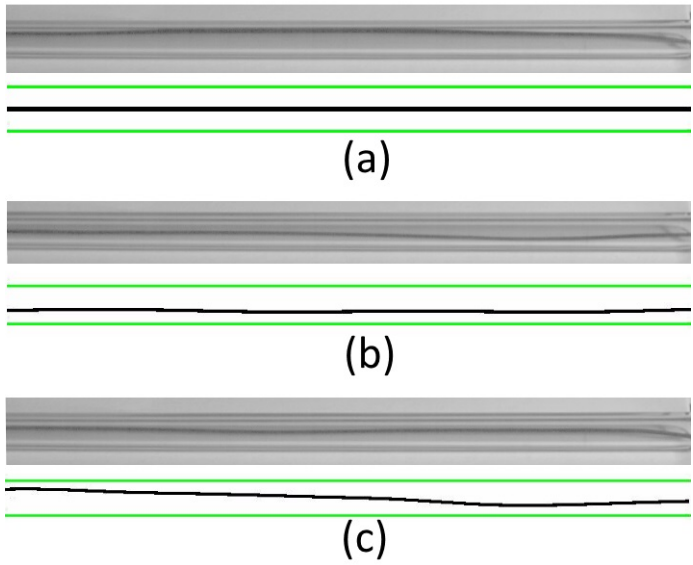

Figure 8.13: Frames of the yarn during experiments and the corresponding frames of the simulations at time: (a) 5.4 ms; (b) 11.7 ms; (c) 16.1 ms. The length of the shown domain equals 125 mm, the right hand side of the domain shown is at the tube exit.

waves are measured from the video recordings during the experiment and the results are listed in Table 8.1.

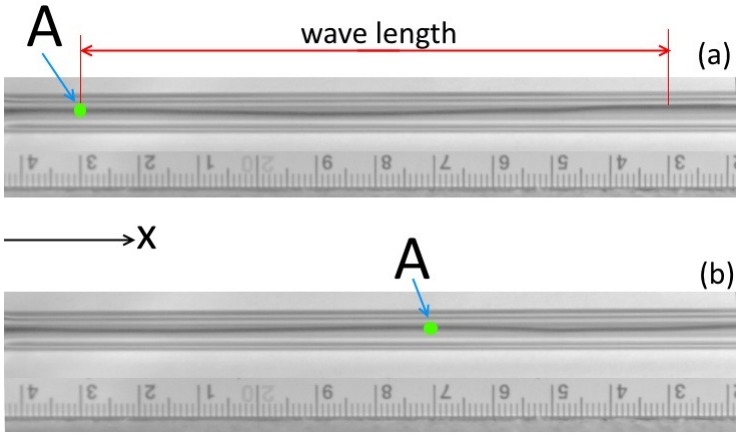

Figure 8.14: Wave characteristics and measurement. Point A from the shown wave is followed to calculate the wave speed. The two frames are taken at time: (a) 12.8 ms; (b) 14.7 ms.

Table 8.1: Measured waves from the experiment.

Wave	Frame time [ms]	c [m/s]	λ [m]	f [Hz]
1	7.8-10.4	15.38	0.07	219
2	12.8-14.7	31.57	0.10	315
3	15.4-16.6	33.33	0.08	416

Table 8.2 lists the obtained values of the wave characteristics from the simulations and the deviations from those of the experiment. The characteristics of the waves obtained from the simulation are not equal to those obtained from the experiment. With the first wave the difference is big, but with the second and the third wave the differences decrease. Moreover, measuring and calculating the waves from the video recordings is not precise.

Table 8.2: Calculated waves from the simulation. The percentage values are the deviations from the corresponding experimental values.

Wave	Frame time [ms]	c [m/s]	λ [m]	f [Hz]
1	8.5-9.9	39.5 (+61.1%)	0.048 (-45.8%)	822 (+73.4%)
2	10.6-11.8	38.3 (+17.6%)	0.091 (-9.9%)	421 (+25.2 %)
3	14.6-16.2	35.6 (+6.4%)	0.060 (-33.3%)	593 (+29.8 %)

8.5.4 Yarn motion

The overall motion of the yarn is analyzed based only on the results of the simulation. Three points from the yarn centerline are chosen. By plotting the coordinates of the three points, it can be seen how the deformations propagate along the yarn. The coordinates of the three chosen points are located in the mixing zone, at the tube center and the yarn free end. Figure 8.15 shows the y- and z-coordinates of the chosen points during the simulations.

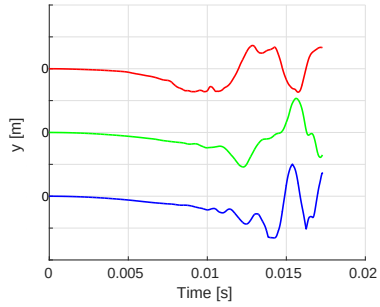

(a)

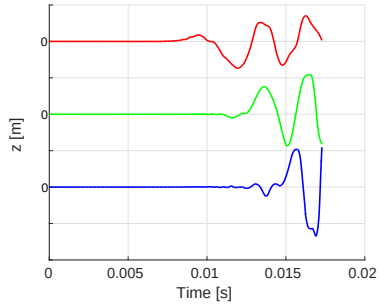

(b)

Figure 8.15: Coordinates of three points from the yarn centerline during the simulations: (a) Y-coordinates; (b) Z-coordinates. The three points are located at the mixing region (red color), tube center (green color) and yarn free end (blue color). Each division in the y- and z-axis is equal to 1 mm.

Figure 8.15(a) shows that, at the first 7 ms of the simulation, the yarn falls towards the tube bottom due to gravity. Moreover, Figure 8.15 indicates that, for example, at 5 ms, the y-coordinates of the three points are almost the same as well as the z-coordinates. However, Figure 8.16 shows frames of the yarn centerline in the xy- and xz-plane. The scale in Figure 8.16 is smaller than the scale in Figure 8.15. In Figure 8.16(a) it is seen that the yarn falls due to gravity but deformation waves with low amplitudes are also seen. When the yarn falls, the flow is not symmetric around it, thus normal forces are generated due to pressure differences. All deformations start in the mixing zone and propagate downstream.

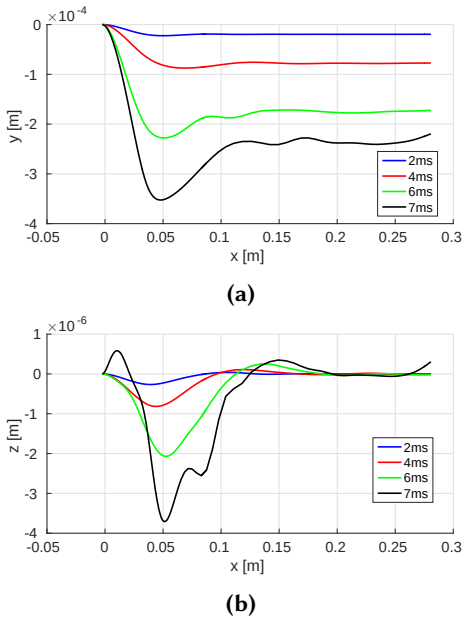

Figure 8.16: Frames of yarn centerline: (a) Y-coordinates; (b) Z-coordinates.

After 10 ms of the simulation time, the amplitudes of the waves increase along z and y as seen in Figure 8.15. The wave amplitudes increase due to an increase of the inlet pressure (see Figure 8.2) which increases the aerodynamic forces on the yarn wall. Figure 8.17 shows contours of static pressure in the yz-plane at an axial coordinate equal to the coordinate of the point in the mixing region (red color line in Figure 8.15), where the origin of the x-coordinate is at the yarn inlet (see Figure 8.4). The static pressure around the yarn in Figure 8.17 can be divided in two regions: a region with high values of static pressure and another with low values. The yarn is pushed towards the region of low pressure.

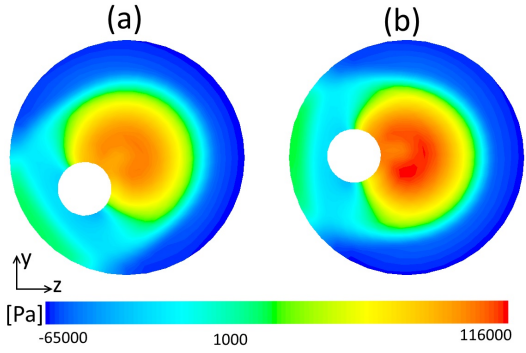

Figure 8.17: Contours of static pressure in the yz-plane where x=37 mm, in the mixing region, at time: (a) 11.5 ms; (b) 12 ms.

Figure 8.18 shows four frames of the yarn centerline. It can be seen that the amplitudes of these waves are higher than the ones in Figure 8.16. The numbers which are highlighted in Figure 8.18 show the same crest of a wave. This wave or crest propagates inside the tube. Therefore, the speed of the wave can be calculated based on this crest. The calculated wave speeds are listed in Table 8.3 in which it can be seen that the wave speed changes inside the nozzle.

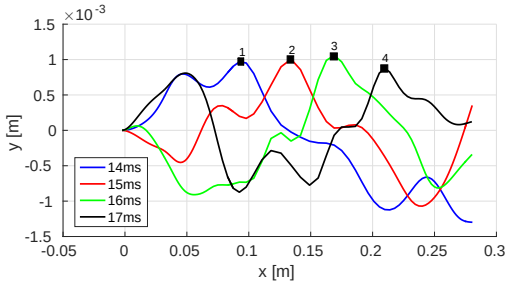

(a)

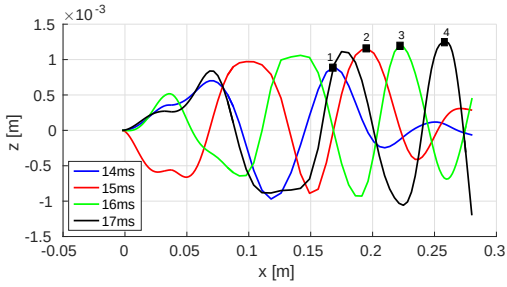

(b)

Figure 8.18: Frames of yarn centerline in the xy and xz planes. The highlighted numbers show the location of the same crest of a wave in the four frames.

Table 8.3: Speed of the waves shown in Figure 8.18 [m/s].

	c_{12}	c_{23}	c_{34}
y_wave	41.63	34.9	40.7
z_wave	22.3	30	36.5

The analytical solution for this case was calculated and studied in [146]. However, the results of the FSI simulation indicate that the deformation waves start from the mixing region where the shocks are located and the yarn is subjected to strong normal forces if it is not located at the centerline which happens due to the gravity. The effects of the shocks are not taken into account in the analytical solution, thus different results will be obtained.

Figure 8.19 shows two frames of the yarn positions and the associated y-components of viscous and pressure forces. Figure 8.19(b) shows that the contributions of the viscous force in the vertical direction are small. The y-component of the force depends mainly on the pressure. The y-component of the pressure force is shown in Figure 8.19(c) along the yarn centerline. It can be seen that there are large contributions in the mixing region where the shocks are present.

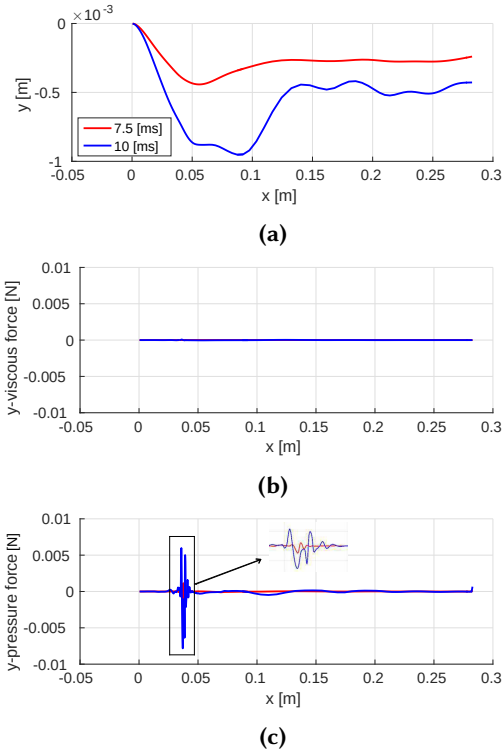

Figure 8.19: (a) Yarn centerline position in the xy-plane; (b) Y-component of viscous force along the yarn centerline; (c) Y-component of pressure force along the yarn centerline.

Other two frames and y-components of the pressure force are shown in Figure 8.20 at time 13 ms and 13.1 ms. These two frames confirm that the highest normal force are due to shock effects. Therefore, it can be said that the location of the shock can be considered as an excitation point. The deformation waves can be linked to the pressure force in this excitation point. Stronger shocks result in higher pressure forces which result in higher deformations. However, if no shocks occur in the mixing region, this does not mean that no waves will be seen. The flow reaches a high velocity inside the main nozzle, thus deformations would be induced by the effects of high speed axial flow. Therefore, in the main nozzle, the vibrations which are induced by shocks start before those which are induced by high speed axial flow.

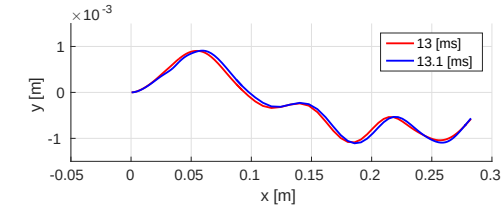

(a)

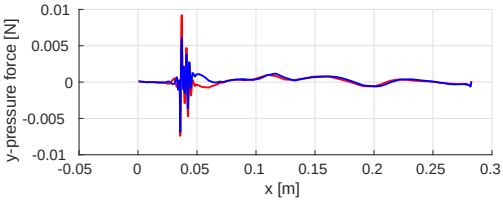

(b)

Figure 8.20: (a) Yarn centerline position in the xy-plane; (b) Y-component of pressure force along the yarn centerline.

The tensile forces also affect the yarn position. Unfortunately, in the simulation setup, the tensile forces have not been selected to be written and they cannot be extracted or calculated after the simulation has been performed. However, the aerodynamic forces can be calculated and the stress can be extracted from the simulation. Figure 8.21 shows the y-coordinate of three chosen segments from the yarn, the y-component of the aerodynamic force and the y-component of the normal stress over the three segments during the simulation time. The gravitational force is in the order of $10^{-5}N$, it affects the position of the yarn only at the beginning of the simulation. The highlighted numbers in each subfigure indicate the moment when the yarn switches direction upwards or downwards.

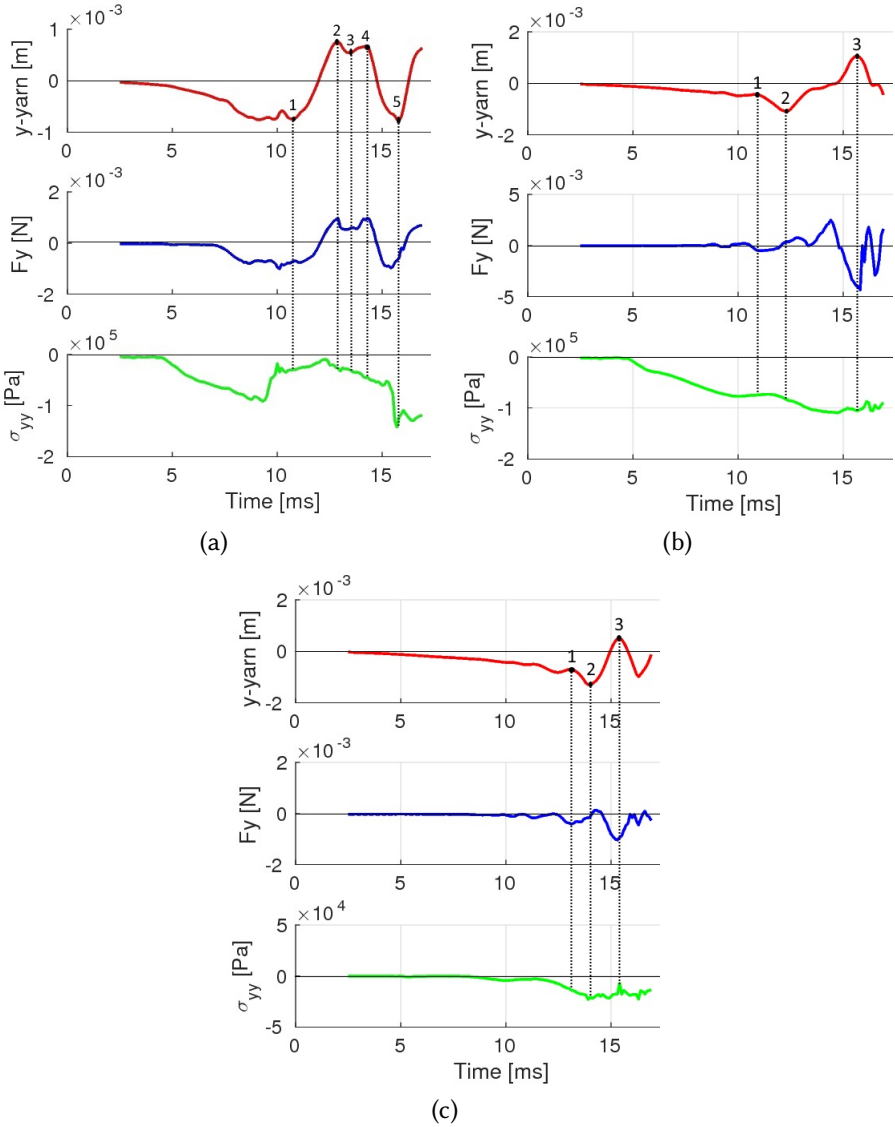

Figure 8.21: Y-coordinate, y-aerodynamic force and the normal stress along y: (a) Segment in the mixing zone; (b) Segment in the middle of the tube; (c) Segment before the end of the yarn.

The y-component of the aerodynamic force over the three chosen segments changes positively and negatively during the simulation. In the mixing zone, the yarn position in point 2, 3 and 4 switches direction according to the aerodynamic force, while in point 5 the aerodynamic force is small and it does not affect the yarn position. For the segment in the middle of the tube, the yarn position in point 1 and 2 is affected by the aerodynamic force and the same is seen in point 2 for the segment

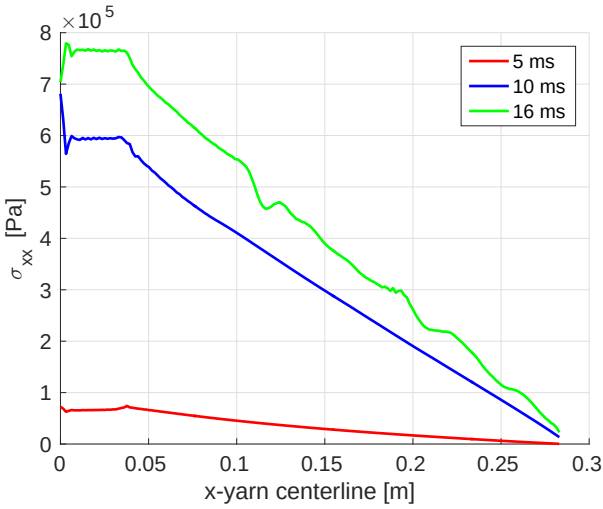

Figure 8.22: Axial stress along the yarn centerline.

before the end of the yarn. However, a clear conclusion about the effects of the forces implies calculating all forces. Moreover, the yarn position is also affected by the axial force and tension. Figure 8.22 shows that the axial stress along the yarn centerline increases with time.

8.6 Conclusion

In this chapter, the fluid-structure interaction simulations of air flow-yarn with dynamic mesh have been presented. The yarn is clamped at one side and it is free at the other side and it is represented as a cylinder in the simulations. The deformation waves which run along the yarn have been obtained and analyzed.

The results of the simulation have been compared with video recordings of the yarn motion during the experiments. The initial position of the yarn is not the same in the simulation and the experiment. Therefore, large differences between the simulation and experiment have been found in the first 10 ms after which the differences are smaller.

The global motion of the yarn has been investigated and it has been found that the deformation waves start from the mixing region which can be considered as an excitation point. These deformations are due to the effects of the shocks which cause a force away from the centerline once the yarn is not on the centerline of the nozzle.

Employing the dynamic mesh technique to perform fluid-structure interaction simulations with a flexible yarn is complex due to the high amplitudes of the deformation waves and the sharp edge of the free end. Fluid mesh distortions could not be avoided by reducing the time step size or by using a coarse mesh. Therefore, in a future work, a more effective method has to be used to handle the dynamic mesh.

In the previous chapter, a different procedure has been suggested to carry out FSI simulations of air flow-yarn. The computational cost of that procedure is about 10 times smaller than the procedure presented in this chapter. Moreover, employing the added source term eliminates the problems of the dynamic mesh and allows modeling the axial motion of the yarn. However, a fair comparison between the results of the two procedures cannot be done without comparing the complete motion of the yarn during one insertion.

Chapter 9

Overall conclusion and future perspectives

9.1 Conclusion

The principal objective of this thesis was to study and analyze the fluid-structure interaction of a yarn in air flow. This interaction has been studied in two applications: yarn splicing and weaving. For the first application, fluid-structure interaction simulations could not be performed due to the complexity of the process. Therefore, yarn splicing has been studied based on air flow simulations. For the second application which belongs to the yarn weaving process, a single yarn is transported by means of air flow, thus, by representing the yarn as a cylinder, different types of fluid-structure interaction simulations have been performed. Moreover, the analytical equations of motion for a cylinder in an axial confined flow have been employed to calculate the critical flow velocities at which a yarn is statically or dynamically unstable inside a main nozzle.

After a brief theoretical introduction, the flow field of a highly underexpanded jet flow has been investigated. Then, the yarn splicing process has been studied based on air flow simulations and experiments. Next, an optimization procedure for the geometry of the main nozzle of an air jet weaving machine has been proposed. Moreover, the instability of a yarn as a cylinder inside a main nozzle has been analyzed based on the analytical equations of motion. Subsequently, numerical models have been developed and employed to model the motion of the weft yarn inside the main nozzle. One-way and two-way FSI simulations of air flow-yarn have been performed inside two main nozzles. In the two-way FSI simulation, the fluid mesh is static and the effects of the yarn motion on the air flow has been added by a source term. Finally, FSI simulations with dynamic mesh have been performed for a clamped-free yarn.

The general pattern of the highly underexpanded jet flow has been captured by LES and RANS. This general pattern can be distinguished by the appearance of the Mach disk which is a normal shock. The position and the diameter of the Mach disk have

been obtained with accepted accuracy in comparison to empirical values. However, the core of the jet flow has been shorter with LES than with RANS. The far-field zone of the jet flow has been evaluated based on comparing the numerical results of the total pressure to experimental measured values. First, it has been shown that neither LES nor RANS simulations have given accurate results of the total pressure in comparison to the experimental ones. Second, other turbulence models have been used with LES (the dynamic model) and with RANS (k-ϵ RNG) and no better results have been obtained. The apparent discrepancies between the numerical and the experimental values have been explained or related to the effects of compressibility. Although the Smagorinsky-Lilly dynamic model takes these effects into account, the LES results, with the basic and the dynamic Smagorinsky-Lilly model, have not been in good agreement with the experiment. It seems that the grid which has been employed with LES has been too coarse to obtain good results, so the grid has to be refined. In the turbulence models of RANS, for example k-ω SST and k-ϵ RNG, correction functions had been suggested to take the compressibility effects into account. The correction functions depend on what is called the initial turbulent Mach number (M_{to}). Based on a recommended value of M_{to} to be used with jet flows and by using the k-ω SST model, the results of the RANS simulations have been improved significantly and good agreement has been found between the RANS results and the experimental ones. By analyzing the flow field it has been shown that the compressibility correction function has not affected the first shock cell of the jet flow or the position of the Mach disk. Without the compressibility correction function, the obtained jet flow dissipates earlier than with it.

Fluid-structure interaction simulations of air flow-yarn inside splicing chambers have not been performed due to the complexity of the splicing process. Pneumatic yarn splicing has instead been analyzed based on air flow simulations. The goal was to find links between the air flow simulations and experiments. The effects of two inlet pressures and the effects of four different splicing chamber geometries have been investigated. The vortices have been found to affect largely the splicing process in such way that if they are not formed inside a chamber, that chamber will not splice the yarn ends. Moreover, the formation of two big and strong vortices is an important flow feature to obtain splices. Increasing the inlet pressure with the studied chambers has only effects on the aerodynamic forces which should be higher with a higher inlet pressure. The geometrical characteristics which have been found to affect the splicing process are the volume of the splicing chamber and the location of the vent hole. The volume of the splicing chamber should be sufficient for flow expansions and for yarn ends interminglement. Increasing the splicing length can be done in two ways: shifting the vent hole location and extending the cutting position of the yarn ends. The experiment indicates that shifting the vent hole location is better and the reason which has been extracted from the CFD results is that, in this case, the flow is completely expanded inside the chamber. The unsteadiness of the flow inside the studied splicing chambers has been evaluated based on the values of the root mean square (RMS) of the velocities. The best splicing chamber geometry, which gives the best splicing strength, generates the highest values of RMS. Therefore, the RMS represents a flow feature which can be used to predict the performance of splicing chambers, but high values of RMS cannot be considered as a good or bad flow feature without powerful vortices which are able to untwist the

yarn ends and splice them.

An optimization procedure for the geometry of the main nozzle of a weaving machine has been proposed. In this procedure, the geometry of the main nozzle is described with parameters. Based on the values of these parameters, several point coordinates are calculated and lines or arcs are drawn in between them. 2D axisymmetric numerical simulations of the air flow inside the nozzle can be performed with the weft yarn as a smooth cylinder on the axis of the main nozzle moving at a specific speed. By means of a gradient-based optimization solver, the optimization has been carried out targeting the geometry of the nozzle that gives the highest axial force. The optimization has been performed for two yarn diameters and for two types of main nozzle geometry which are a threadable and a non-threadable geometry. The threading property for the main nozzle geometry is used when the weaving machine is not working to suck a yarn inside it. Many steps have been performed to check that the obtained results are global minimums and not local. The forces of the obtained optimum geometries have been improved in comparison to reference values. Including the threading constraint has decreased the optimum force. The results of the optimization indicates that a progressive expansion of the air flow inside a main nozzle is better to have higher axial force.

Inside the main nozzle, the flow is aligned mainly with the yarn. The axial flow with a high velocity induces vibrations on the structure. Therefore, the air flow critical velocities at which the weft yarn becomes unstable have been obtained by using the analytical equations of motion for a cylinder in confined flow. It has been found that the weft yarn vibrates during the working conditions of weaving machines (the inlet pressure of 5 bar) but not necessarily during the holding flow conditions (the inlet pressure < 1 bar) depending on the weft yarn diameter and length.

The motion of a cotton yarn which is moving axially and radially inside two main nozzles has been modeled and analyzed for one insertion. Numerical models have been developed and employed to perform the FSI simulations of air flow-yarn. A three-dimensional structure model of the flexible weft yarn, consisting of a chain of line segments has been employed to calculate deformations of the weft yarn as a flexible body. The fluid model is two-dimensional axisymmetric. To avoid mesh distortions, the arbitrary Lagrangian-Eulerian technique has not been used. This means that the fluid grid is fixed during the simulations. Therefore, the effects of the yarn motion on the air flow has been added by a source term. The aerodynamic force coefficients have been tuned in such a way that roughness of the yarn surface is included. The results of the simulations have been compared to experimental data and recorded videos. It has been found that the results of two-way FSI simulations are closer to the experiments than the results of the one-way (without the source term).

Fluid-structure interaction simulations with dynamic mesh have been carried out for a clamped-free nylon yarn. In this type of simulation, the effects of the yarn motion on the air flow are taken into account by moving the fluid-structure interface in the fluid domain. This means that the flow equations are solved in the arbitrary Lagrangian-Eulerian (ALE) formulation. The results of the FSI simulations have been compared to experiments. Due to a different initial yarn position, there have been high differences between the simulations and the experiment at the beginning.

However, the differences have decreased with time (simulation or experiment time). It has been found that all deformation waves start due to shocks effects. Employing the dynamic mesh with a flexible body like yarn is complex due to mesh distortions which are caused by the high wave amplitudes and by the sharp edge of the free end.

9.2 Recommendations for future work

In this section, some recommendations for future work are suggested. It would be interesting to investigate further the studied highly underexpenaded jet flow by large-eddy simulations. The results of the performed simulations with LES have not been in good agreement with the experiment. The basic Smagorinsky-Lilly subgrid-scale model does not include the compressibility effects, whereas these effects are included in the dynamic model. Therefore, the dynamic model has to be used with LES. The dynamic model has been tested in this work, but the grid which has been used seems to be too coarse. Moreover, as the comparison between the numerical and experimental results has to be done in the far-field zone ($x/D > 35$), the grid resolution has to be fine in the near-field as well as in the far-field. Refining the mesh is not a problem, but the problem is with the computing resource. Moreover, the scale-selective discretization (SSD) scheme which was suggested by Vuorinen et al. [35] to decrease the numerical dissipation can be adapted and tested.

The splicing process has been studied based on air flow simulations. Additional air flow features which affect the splicing process should be investigated with other types of chamber which generate different air flow patterns. This can ensure that the links which have been found are common or they are associated with the studied type of chamber. Moreover, the cover of the splicing chamber which has been used in the simulations is flat. Therefore, different shapes of the chamber cover would change the air flow pattern and this may affect the splicing.

The effectiveness of the proposed procedure to optimize the geometry of the main nozzle has been proven. Therefore, it can be employed to investigate other geometrical effects. For example, instead of considering the tube as a whole, as in the performed optimization, it can be divided in multiple parts. This can be adapted and tested in the proposed procedure. Moreover, the throat section location has not been controlled during the optimization. The throat section location affects the expansion of the flow after it, thus the shocks which affect the aerodynamic force and the motion of the yarn. Controlling the throat section location during the optimization is not simple, but it can be achieved by fixing the variables which change it.

The instability of the weft yarn inside the main nozzle has been analyzed based on the linear equations of motion. The nonlinear equations of motion for a cylinder in confined axial flow had been derived in [106]. The main difference which is taken into account in the derivation of the nonlinear equations is the aerodynamic forces for which the nonlinear forms had been derived. Therefore, by using the nonlinear equations of motion, the nonlinear dynamics should be investigated.

Only the motion of a cotton yarn has been modeled by employing the proposed numerical models. Moreover, the yarn has been represented as a smooth cylin-

der along the axis of the main nozzle. This representation has been made to take into account the volume occupied by the yarn in the fluid domain. Based on the presented results, this assumption has succeeded in giving good results. However, the numerical models should be tested with other thicker or thinner yarns. For example, it may be possible that for a thinner yarn there is no need to represent it as a cylinder in the fluid domain. If this point is tested, experiments have to be carried out with such a yarn to compare the numerical results with them. The effects of yarn twisting should also be added to the structure model. It has been mentioned that the proposed numerical models can be employed to optimize the geometry of the main nozzle. Testing a new main nozzle design is straightforward as the yarn tip position and the speed of the yarn can be easily obtained, but coupling the numerical models with an optimization solver is not applicable because it takes almost one day to perform one FSI simulation. The duration of one FSI simulation can be reduced by increasing the convergence tolerance of the equilibrium conditions on the fluid-structure interface. This may reduce the number of iterations which have to be performed at each time step to satisfy the equilibrium conditions. Reducing the duration of the FSI simulation can also be done by increasing the time step of the simulation. This decreases the total number of time steps which has to be performed for one insertion. In both cases, the accuracy of the FSI simulation should be tested.

The fluid-structure interaction simulations of air flow-yarn with dynamic mesh have been performed with a yarn as a smooth cylinder. However, the hairiness of the yarn can be included in the simulations by the cylinder roughness. This point should be investigated, but experiments have to be performed to measure the aerodynamic forces, thus the cylinder roughness can be tuned according to the measured forces. The main issue with this type of simulations is the dynamic mesh. Mesh distortions could not be avoided by reducing the time step or changing the fluid mesh and so a different method has to be employed to handle the dynamic mesh.

List of Figures

List of Tables

Bibliography

[1] D. C. Wilcox. *Turbulence Modeling for CFD*. La Cañada (Calif.): DCW industries, 1993.

[2] E. Franquet, V. Perrier, and S. Gibout et al. Free underexpanded jets in a quiescent medium: A review. *Progress in Aerospace Sciences*, 77:25–53, 2015.

[3] G. A. Blaisdell and O. Zeman. Investigation of the dilatational dissipation in compressible homogeneous shear flow. *Center for Turbulence Research*, Proceedings of the Summer Program 1992:231–245, 1995.

[4] R. H. Ricketts. Experimental aeroelasticity history, status and future in brief. *NASA technical memorandum 102651*, 1990.

[5] L. Szabó and L. Szabó. Weft insertion through open profile reed in air jet looms. *Annals of faculty engineering Hunedoara, Internationl journal of engineering*, ISSN(1584-2665):211–218, 2012.

[6] M. P. Païdoussis. *Fluid-structure interactions: Slender structure and axial flow*, volume 1. Academic Press, 1998.

[7] M. P. Païdoussis. *Fluid-structure interactions: Slender structure and axial flow*, volume 2. Academic Press, 2004.

[8] A. Osman, S. De Meulemeester, B. Malengier, J. Degroote, and J. Vierendeels. Numerical prediction and experimental analysis of ends-together yarn splicing. *Textile Research Journal*, page 0040517516654109, . doi:10.1177/0040517516654109.

[9] A. Osman, B. Malengier, S. De Meulemeester, J. Peeters, J. Vierendeels, and J. Degroote. Simulation of air flow-yarn interaction inside the main nozzle of an air jet loom. *Textile Research Journal*, page 0040517517697646, . doi:10.1177/0040517517697646.

[10] H. Versteeg and W. Malalaskra. *An introduction to computational fluid dynamics*. Pearson, 2nd edition, 2007.

[11] J. Fröhlich and D. V. Terzi. Hybrid LES/RANS methods for the simulation of turbulent flows. *Progress in Aerospace Sciences*, 44:349–377, 2008.

[12] P. R. Spalart and S. R. Allmaras. A one-equation turbulence model for aerodynamic flows. *The American Institute of Aeronautics and Astronautics*, Paper 92-0439, 1994.

[13] F. R. Menter. 2-equation eddy-viscosity turbulence models for engineering applications. *The American Institute of Aeronautics and Astronautics*, 32(8): 1598–1605, 1994.

[14] J. Smagorinsky. General circulation experiments with the primitive equations, I. the basic experiment. *Monthly Weather Review*, 91:99–164, 1963.

[15] J. Degroote. *Development of algorithms for the partitioned simulation of strongly coupled fluid-structure interaction problems*. PhD thesis, Ghent University, 2010.

[16] N. Ruangtrakoon, T. Thongtip, and S. Aphornratana et al. CFD simulation on the effect of primary nozzle geometries for a steam ejector in refrigeration cycle. *International Journal of Thermal Sciences*, 63:133–145, 2013.

[17] V. Vuorinen, J. Yu, and S. Tirunagari et al. Large-eddy simulation of hihgly underexpanded transient. *Physics of Fluids*, 25(016101), 2013.

[18] J. Yu, V. Vuorinen, and O. Kaario et al. Visualization and analysis of the characteristics of transitional underexpanded jets. *International Journal of Heat and Fluid Flow*, 44:140–154, 2013.

[19] J. M. Eggers. Velocity profiles and eddy viscosity distributions downstream of a Mach 2.22 nozzle exhausting to quiescent air. *NASA technical Note*, (TN D-3601), 1966.

[20] P. E. Dimotakis, R. C. Miake-Lye, and D. A. Papantoniou. Structure and dynamics of round turbulent jets. *Physics of Fluids*, 26(11):3185–3192, 1983.

[21] A. W. K. Law and Herlina. An experimental study on turbulent circular wall jets. *Journal of Hydraulic Engineering*, 128(2):161–174, 2002.

[22] J. A. Inman, P. M. Danehy, R. J. Nowak, and D. W. Alderfer. Identification of instability modes of transition in underexpanded jets. 28th Fluid Dynamics Conference and Exhibit, Washington, USA, June 2008. The American Institute of Aeronautics and Astronautics 2008-4389.

[23] Y. S. Tsai, J. C. R. Hunt, and F. T. M. Nieuwstadt et al. Effect of strong external turbulence on a wall jet boundary layer. *Flow, Turbulence and Combustion*, 79: 155–174, 2007.

[24] B. J. Boersma and S. K. Lele. Large eddy simulation of compressible turbulent jets. *Center for Turbulence Research, Annual Research Briefs*, 1999.

[25] P. E. Dimotakis. The mixing transition in turbulent flows. *Journal of Fluid Mechanics*, 409:69–98, 2000.

[26] D. Munday, E. Gutmark, and J. Liu et al. Flow structure of supersonic jets from conical c-d nozzles. volume 39th AIAA FLuid Dynamics Conference, Texas, USA, June 2009.

[27] A. C. Bayeh. Analysis of Mach disks from an underexpanded nozzle using experimental and computational methods. 47th AIAA Aerospace Sciences Meeting, Florida, USA, January 2009. The American Institute of Aeronautics and Astronautics 2009-217.

[28] T. N. Aziz, J. P. Raiford, and A. A. Khan. Numerical simulation of turbulent jets. *Engineering Applications of Computational Fluid Mechanics*, 2(2):234–243, 2008.

[29] C. Heschl, K. Inthavong, and W. Sanz et al. Evaluation and improvements of RANS turbulence models for linear diffuser flows. *Computers and Fluids*, 71: 272–282, 2013.

[30] S. A. Karabasov, M. Z. Afsar, and T. P. Hynes et at. Jet noise: Acoustic analogy informed by large eddy simulation. *The American Institute of Aeronautics and Astronautics*, 48(7):1312–1325, 2010.

[31] G. A. Faranosov, V. M. Goloviznin, and S. A. Karabasov et al. Cabaret method on unstructured hexahedral grids for jet noise computation. *Computers and Fluids*, 88:165–179, 2013.

[32] A. Velikorodny and S. Kudriakov. Numerical study of the near-field of highly underexpanded turbulent gas jets. *International Journal of Hydrogen Energy*, 37:17390–17399, 2012.

[33] X. Li, K. Wu, and W. Yao et al. A comparative study of highly underexpanded nitrogen and hydrogen jet using large eddy simulation. *International Journal of Hydrogen Energy*, 41:5151–5161, 2016.

[34] A. Hamzehloo and P. G. Aleiferis. Large eddy simulation of highly turbulent underexpanded hydrogen and methane jets for gaseous-fuelled internal combustion engines. *International Journal of Hydrogen Energy*, 39:21275–21296, 2014.

[35] V. Vuorinen, M. Larmi, and P. Schlatter et al. A low-dissipative, scale-selective discretization scheme for the navier-stokes equations. *Computers and Fluids*, 70(195-205), 2012.

[36] D. D. Joseph and J. C. Saut. Short-wave instabilities and ill-posed initial-value problems. *Theoretical and Computational Fluid Dynamics*, 1:191–227, 1990.

[37] G. Tryggvason. Numerical simulations of the Rayleigh-Taylor instability. *Journal of Computational Physics*, 75:253–282, 1988.

[38] V. Todde, P. F. Spazzini, and M. Sandberg. Experimental analysis of low-Reynolds number free jets, evolution along the jet centerline and Reynolds number effects. *Experiments in Fluids*, 47:279–294, 2009.

[39] Y. Zaouali, T. Filali, and H. B. Aissia et al. Flow structure generated from an axisymmetric natural air jet at moderate reynolds number. *Fluid Dynamics Research*, 43(3):035502(13), 2011.

[40] S. Lardeau, E. Collin, and E. Lamballais et al. Analysis of a jet-mixing layer interaction. *International Journal of Heat and Fluid Flow*, 24:520–528, 2003.

[41] R. F. Davey and A. Roshko. The effect of a density difference on shear-layer instability. *Journal of Fluid Mechanics*, 53(3):523–543, 1972.

[42] G. L. Brown and A. Roshko. On density effects and large structures in turbulent mixing layers. *Journal of Fluid Mechanics*, 64:775–781, 1974.

[43] D. Papamoschou and A. Roshko. The compressible turbulent shear layer: an experimental study. *Journal of Fluid Mechanics*, 197:453–477, 1988.

[44] D. W. Bogdonoff. Compressibility eeffect in turbulent shear layers. *The American Institute of Aeronautics and Astronautics*, 21(6):926–927, 1983.

[45] W. Shyy and V. S. Krishnamurty. Compressibility effects in modeling complex turbulent flows. *Progress in Aerospace Sciences*, 33:587–645, 1997.

[46] O. Zeman. Dilatation dissipation: the concept and application in modeling compressible mixing layer. *Physics of Fluids*, 2:178–188, 1990.

[47] S. Sarkar, G. Erlebacher, M. Y. Hussaini, and et al. The analysis and modeling of dilatational terms in compressible turbulence. *Journal of Fluid Mechanics*, 227:473–493, 1991.

[48] D. Wilcox. Dilatation-dissipation corrections for advanced turbulence models. *The American Institute of Aeronautics and Astronautics*, 30:2639–2646, 1992.

[49] L. L. Zheng and K. N. Bray. Effect of dilatation dissipation on turbulent shear layer combustion in high speed flow. *Twenty-Fourth Symposium (International) on Combustion*, 24(1):405–411, 1992.

[50] S. Paul Pao and K. S. Abdol-Hamid. Numerical simulation of jet aerodynamics using the three-dimensional Navier-Stokes code PAB3Db. *NASA technical Paper 3596*, 1996.

[51] N. Gross, G. A. Blaisdell, and A. S. Lyrintzis. Analysis of modified compressibility corrections for turbulence models. Florida, USA, January 2011. 49th AIAA Aerospace Sciences Meeting including the New Horizons Forum and Aerospace Exposition.

[52] P. Birkby and G. J. Page. Numerical predictions of turbulent underexpanded sonic jets using a pressure-based methodology. *Proceedings of the Institution of Mechanical Engineers, Part G: Journal of Aerospace Engineering*, 215:165–173, 2001.

[53] B. Thurow, M. Samimy, and W. Lempert. Compressibility effects on turbulence structures of axisymmetric mixing layers. *Physics of Fluids*, 15(6):1755–1765, 2003.

[54] H. G. Sung, S. J. Kim, and H. W. Yeom et al. On the assessment of compressibility effects of two-equation turbulence models for supersonic transition flow with flow separation. *The International Journal of Aeronautical and Space Sciences*, 14(4):387–397, 2013.

[55] A. Balabel, A. M. Hegab, and M. Nasr et al. Assessment of turbulence modeling for gas flow in two-dimensional convergent–divergent rocket nozzle. *Applied Mathematical Modelling*, 35:3408–3422, 2011.

[56] Y. Bartosiewicz, Z. Adioun, and P. Desevaux et al. CFD-experiments integration in the evaluation of six turbulence models for supersonic ejector modeling. Glasgow, UK, September 2003. Integrating CFD and Experiments Conference.

[57] D. K. Lilly. The representation of small-scale turbulence in numerical simulation experiments. pages 195–210, Yorktown Heights, USA, 1967. In IBM Scientific Computing Symposium on Environmental Science.

[58] G. Erlebacher, M. Y. Hussaini, and C. G. Speziale et al. Toward the large-eddy simulation of compressible turbulent flows. *NASA Contractor Report*, (AD-A229 671), 1990.

[59] A. Dauptain, B. Cuenot, and Y. M. Gicquel. Large-eddy simulation of a stable supersonic jet impinging on flat plate. *The American Institute of Aeronautics and Astronautics*, 48(10):2325–2337, 2010.

[60] H. Ashkenas and F. Sherman. Structure and utilization of supersonic free jets in low density wind tunnels. *NASA technical Report*, (No. CR-60423), 1965.

[61] M. Germano, U. Piomelli, and P. Moin et al. A dynamic subgrid-scale eddy-viscosity model. *Physics of Fluids A*, 3(7):1760–1765, 1991.

[62] V. Yakhot, S. A. Orszag, and S. Thangam et al. Development of turbulence models for shear flows by a double expansion technique. *Physics of Fluids A*, 4(7):1510–1520, 1992.

[63] N. J. Georgiadis, D. A. Yoder, and W. A. Engblom. Evaluation of modified two-equation turbulence models for jet flow prediction. 44th AIAA Aerospace Sciences Meeting and Exhibit, Nevada, January 2006.

[64] J. R. DeBonis. Progress toward large-eddy simulations for prediction of realistic nozzle systems. *Journal of Propulsion and Power*, 23(5):971–980, 2007.

[65] P. Moin, K. Squires, and W. Cabot et al. A dynamic subgrid-scale model for compreesible turbulence and scalar transport. *Physics of Fluids A Fluid dynamics*, 3(11):2746–2757, 1991.

[66] X. Chai and K. Mahesh. Dynamic k-equation model for large-eddy simulation of compressible flows. *Journal of Fluid Mechanics*, 699:385–413, 2012.

[67] C. J. Webb, G. T. Waters, and A. J. Thomas et al. The use of the taguchi design of experiment method in optimizing splicing conditions for a nylon 66 yarn. *The Journal of The Textile Institute*, 98(4):327–336, 2007.

[68] C. J. Webb, G. T. Waters, and G. P. Liu et al. The use of visualisation and simulation technique to model the splicing process. *The Journal of The Textile Institute*, 101(10):859–869, 2010.

[69] J. Zhou and P. Qin. Air flow in a pneumatic splicer by CFD. *Textile Research Journal*, 75(2):106–110, 2005.

[70] X. Xing and G. Ye. Numerical simulation of yarn untwisting mechanism in pneumatic splicer process. *Applied Mechanics and Materials*, 229-231:1721–1724, 2012.

[71] Z. Wu, P. Shi, and S. Chen et al. Study on effects of structural parameters on untwisting performance in pneumatic yarn splicing. *Textile Research Journal*, 85(17):1776–1788, 2015.

[72] C. Degong, L. Dengchen, and L. Songmei et al. Research on the impact of vent pressure on the yarn splicing based on ansys. *Key Engineering Materials*, 584: 50–53, 2014.

[73] J.Z. Wang, G.Z. Zhou, and L. Ll et al. Air dynamics characteristics analysis of air splicer. *Key Engineering Materials*, 561:483–489, 2013.

[74] Z. Wu, P. Shi, and S. Chen et al. Study on the effects of the characteristics of a vortex on splice strength in pneumatic yarn splicing. *Textile Research Journal*, 86(3):264–274, 2016.

[75] C. J. Webb, G. T. Waters, and A. J. Thomas et al. Optimising splicing parameters for splice aesthetics for a continuous filament synthetic yarn. *The Journal of The Textile Institute*, 100(2):141–151, 2009.

[76] S. De Meulemeester, B. Malengier, and L. Van Langenhove. Experimental investigation and optimization of ends-together pneumatic splice chambers. *Textile Research Journal*, 86(17):1803–1815, 2016.

[77] J. Fröhlich, H. Kuerten, and B. J. Geurts. *Direct and Large-Eddy Simulation IX*. ERCOFTAC series. Springer, 2015.

[78] C. J. Webb, G. T. Waters, and G. P. Liu et al. The influence of yarn count on the splicing of simple continuous filament synthetic yarns. *Textile Research Journal*, 79(3):195–204, 2009.

[79] ö. Göktepe and O. Bozkan. Study on reduction of air consumption on air-jet weaving machines. *Textile Research Journal*, 78(9):816–824, 2008.

[80] H. Nosraty, A.A.A. Jeddi, and M. Kabganian et al. Influence of controlled weft yarn tension of a single nozzle air-jet loom on the physical properties of the fabric. *Textile Research Journal*, 76(8):637–645, 2006.

[81] M. Uno, K. Yamawaki, and T. Ishida et al. A study on air-jet looms. *Journal of the Textile Machinery Society of Japan*, 7(1):28–36, 1961.

[82] M. Uno. A study on an air-jet loom with substreams added, part 3: Synthesis of substreams. *Journal of the Textile Machinery Society of Japan*, 18(4):106–113, 1972.

[83] M. Uno. A study on an air-jet loom with substreams added, part 4: Length of main nozzle. *Journal of the Textile Machinery Society of Japan*, 18(4):114–119, 1972.

[84] M. Uno. A study on an air-jet loom with substreams added, part 5: Analogous experiment of flow. *Journal of the Textile Machinery Society of Japan*, 18(5-6): 135–140, 1972.

[85] M. H. Mohamed and M. Salama. Mechanics of a single nozzle air-jet filling insertion system, part i: Nozzle design and performanc. *Textile Research Journal*, 57(1):44–54, 1987.

[86] M. Ishida and A. Okajima. Flow characteristics of the main nozzle in an air-jet loom, part i: Measuring flow in the main nozzle. *Textile Research Journal*, 64 (1):10–20, 1994.

[87] M. Ishida and A. Okajima. Flow characteristics of the main nozzle in an air-jet loom, part ii: Measuring high speed jet flows from the main nozzle and weft drag forces. *Textile Research Journal*, 64(2):88–100, 1994.

[88] T. H. Oh, S. D. Kim, and D. J. Song. A numerical analysis of transonic/supersonic flows in the axisymmetric main nozzle of an air-jet loom. *Textile Research Journal*, 71(9):783–790, 2001.

[89] C. Prabkeao and K. Aoki. Flow characteristics and pattern of main nozzle of air jet loom. *Proceedings of the School of Engineering, Tokai University, Series E*, 30:7–14, 2005.

[90] S. Adanur and M. H. Mohamed. Analysis of air flow in air-jet filling insertion. *Textile Research Journal*, 61(5):253–258, 1991.

[91] G. M. Ye and D. F. Shen. Study on pneumatic weft insertion behaviour in main nozzle. *Fibres and Textiles in Eastern Europe*, 15(4):68–72, 2007.

[92] H. D. Kim, C. M. Lim, and H. J. Lee et al. A study of the gas flow through air jet loom. *Journal of Thermal Science*, 16(2):159–163, 2007.

[93] G. Belforte, G. Mattiazzo, and V. Viktorov et al. Numerical model of an air-jet loom main nozzle for drag forces evaluation. *Textile Research Journal*, 79(18): 1664–1669, 2009.

[94] L. Chen, Z. H. Feng, and T. Z. Dong et al. Numerical simulation of the internal flow field of a new main nozzle in an air-jet loom based on fluent. *Textile Research Journal*, 85(15):1590–1601, 2015.

[95] Y. Jin, J. Cui, and L. Zhu et al. An investigation of some parameter effects on the internal flow characteristics in the main nozzle. *Textile Research Journal*, 87(1):91–101, 2017.

[96] A. Forsgren, P. E. Gill, and M. H. Wright. Interior methods for nonlinear optimization. *Society for Industrial and Applied Mathematics*, 44(4):525–597, 2002.

[97] M. P. Païdoussis. Dynamics of cylindrical structures subjected to axial flow. *Journal of Sound and Vibration*, 29(3):365–385, 1973.

[98] M. P. Païdoussis, E. Grinevich, and D. Adamovic et al. Linear and nonlinear dynamics of cantilevered cylinders in axial flow. part 1: Physical dynamics. *Journal of Fluids and Structures*, 16(6):691–713, 2002.

[99] S. Rinaldi and M. P. Païdoussis. Theory and experiments on the dynamics of a free-clamped cylinder in confined axial-flow. *Journal of Fluids and Structures*, 28(3):167–179, 2012.

[100] L. Wang and Q. Ni. Vibration of slender strcuture subjected to axial flow or axially towed in quiescent fluid. *Advances in Acoustics and vibration*, vol. 2009: Article ID 432340. 19 Pages, 2009.

[101] Y. Modarres-Sadeghi, M. P. Païdoussis, and C semler. Nonlinear behaviour of a slender flexible cylinder pinned or clamped at both ends and subjected to axial flow. *Computers and Structures*, 85:1121–1133, 2007.

[102] J. De Ridder, J. Degroote, and K. Van T et al. Modal characteristics of a flexible cylinder in turbulent axial flow from numerical simulations. *Journal of Fluids and Structures*, 43:110–123, 2013.

[103] J. De Ridder, O. Doaré, and J. Degroote et al. Simulating the fluid forces and fluid-elastic instabilities of a clamped-clamped cylinder in turbulent axial flow. *Journal of Fluids and Structures*, 55:139–154, 2015.

[104] J. De Ridder. *Computational analysis of flow-induced vibrations in fuel rod bundles of next generation nuclear reactors*. PhD thesis, Ghent University, 2016.

[105] J. L. Lopes, M. P. Païdoussis, and C. Semler. Linear and nonlinear dynamics of cantilevered cylinders in axial flow. part 2: the equations of motion. *Journal of Fluids and Structures*, 16(6):715–737, 2002.

[106] J. L. Lopes, M. P. Païdoussis, and C. Semler. Nonlinear equations of a cylinder in steaady axial flow. *Department of Mechanical Engineering, McGill University, Montreal, Québec, Canada*, Report MERL(99-1), 1999a.

[107] J. L. Lopes, M. P. Païdoussis, and C. Semler. Nonlinear dynamics of a cylinder in steady axial flow. *Department of Mechanical Engineering, McGill University, Montreal, Québec, Canada*, Report MERL(99-2), 1999b.

[108] C. Semler and J. L. Lopes. Augu et al. Linear and nonlinear dynamics of cantilevered cylinders in axial flow, part 3: Nonlinear dynamics. *Journal of Fluids and Structures*, 16(6):739–759, 2002.

[109] M. J. Lighthill. Note on the swimming of slender fish. *Journal of Fluid Mechanics*, 9:305–317, 1960.

[110] G. Taylor. Analysis of the swimming of long and narrow animals. *Proceedings of the Royal Society of London A*, 214(1117):158–183, 1952.

[111] S. F. Hoerner. *Fluid-dynamic drag: practical information on aerodynamic drag and hydrodynamic resistance.* Hoerner Fluid Dynamics, 1965.

[112] W. L. Keith, K. M. Cipolla, and D. R. Hart et al. Drag measurements on long, thin cylinders at small angles and high reynolds numbers. *Naval Undersea Warfare Center Division*, Technical Report 11555(20040920 130), 2004.

[113] K. M. Cipolla and W. L. Keith. High reynolds number thick axisymmetric turbulent boundary layer measurements. *Experiments in Fluids*, 35:477–485, 2003.

[114] O. R. Tutty and W. G. Price. Boundary layer flow on a long thin cylinder. *Physics of Fluids*, 14(2):628–637, 2002.

[115] K. M. Cipolla and W. L. Keith. Momentum thickness measurements for thick axisymmetric turbulent boundary layers. *Journal of Fluids Engineering*, 125: 569–575, 2003.

[116] O. R. Tutty. Flow along a long thin cylinder. *Journal of Fluid Mechanics*, 602: 1–37, 2008.

[117] F. M. White. The axisymmetric turbulent boundary layer on a extremely long cylinder. *Navy Underwater Sound Laboratory*, Report No. 1058(AD700246), 1969.

[118] R. L. Richmond. *Experimental Investigation of thick, axaxial symmetric boundary layers on cylinders at subsonic and hypersonic speeds.* Phd thesis, California Institute of Technology, 1957.

[119] S. Ersdal and O. M. Faltinsen. Normal forces on cylinders in near-axial flow. *Journal of Fluids and Structures*, 22:1057–1077, 2006.

[120] L. Divaret, O. Cadot, and P. Moussou et al. Normal forces exerted upon a long cylinder oscillating in an axial flow. *Journal of Fluid Mechanics*, 752:649–669, 2014.

[121] M. Kheiri, M. P. Païdoussis, and M. Amabili. An experimental study of dynamics of twoed flexible cylinders. *Journal of Sound and Vibration*, 348: 149–166, 2015.

[122] E. De. Langre, M. P. Païdoussis, and O. Doaré et al. Flutter of long flexible cylinders in axial flow. *Journal of Fluid Mechanics*, 571:371–389, 2007.

[123] C. Lemaitre, P. Hémon, and E. de Langre. Instability of a long ribbon hanging in axial air flow. *Journal of Fluids and Structures*, 20:913–925, 2005.

[124] M. Uno. A study on an air-jet loom with substreams added, part 1: Deriving the equation of motion for weft. *Journal of the Textile Machinery Society of Japan*, 18(2):37–44, 1972.

[125] M. Uno, A. Shiomi, and H. Kise. A study on an air-jet loom with sub-streams added, part 2: Analysis of various weaving factors by the equation of motion of weft. *Journal of the Textile Machinery Society of Japan*, 18(3):86–92, 1972.

[126] S. Adanur and M. H. Mohamed. Analysis of air flow in air-jet filling insertion. *Textile Research Journal*, 61(5):259–266, 1991.

[127] S. Adanur and M. H. Mohamed. Analysis of yarn motion in single-nozzle air-jet filling insertion, part i: Theoretical models for yarn motion. *The Journal of The Textile Institute*, 83(1):45–55, 1992.

[128] T. Turel, S. Bakhtiyarov, and S. Adanur. Effect of air and yarn characteristics in air-jet filling insertion, part i: Air velocity and air pressure measurements. *Textile Research Journal*, 74(7):592–597, 2004.

[129] S. Adanur and T. Turel. Effects of air and yarn characteristics in air-jet filling insertion, part ii: Yarn velocity measurements with profiled reed. *Textile Research Journal*, 74(8):657–661, 2004.

[130] N. Celik, O. Babaarslan, and M. P. U. Bandara. A mathematical model for numerical simulation of weft insertion on an air-jet weaving machine. *Textile Research Journal*, 74(3):236–240, 2004.

[131] H. Nosraty, A. A. A. Jeddi, and Y. Mousaloo. Simulation analysis of weft yarn motion in single nozzle air-jet loom to study the effective parameters. *Indian Journal of Fibre and Textile Research*, 33:45–51, 2008.

[132] I. Patkó. Material transport with air jet. *Acta Polytechnica Hungarica, Journal of Applied Sciences*, 2(2):53–65, 2005.

[133] L. Szabó, I. Patkó, and G. Oroszlány. The dynamic study of the weft insertion of air jet weaving machines. *Acta Polytechnica Hungarica, Journal of Applied Sciences*, 7(3):93–107, 2010.

[134] L. Vangheluwe, B. Sleeckx, and P. Kiekens. Numerical simulation model for optimisation of weft insertion on projectile and rapier looms. *Mechatronics*, 5 (2):183–195, 1995.

[135] S. De Meulemeester, J. Githaiga, and L. Van Langenhove et al. Simulation of the dynamic yarn behavior on airjet looms. *Textile Research Journal*, 75(10): 724–730, 2005.

[136] S. De Meulemeester, P. Puissant, and L. Van Langenhove. Three-dimensional simulation of the dynamic yarn behavior on air-jet looms. *Textile Research Journal*, 79(18):1706–1714, 2009.

[137] Y. Cai and W. Oxenham. Computer modeling of fiber movements in high-speed airflow. *Research Journal of Textile and Apparel*, 9(4):77–85, 2005.

[138] W. Tang and S. G. Advani. Dynamic simulation of long flexible fibers in shear flow. *Computer Modeling in Engineering and Sciences*, 8(2):165–176, 2005.

[139] G. Kondora and D. Asendrych. Modelling the dynamics of flexibles and rigid fibres. *Chemical and Process Engineering*, 34(1):87–100, 2013.

[140] Z. Pei and C. Yu. Numerical study on the effect of nozzle pressure and yarn delivery speed on the fiber motion in the nozzle of murata vortex spinning. *Journal of FLuids and Structures*, 27:121–133, 2011.

[141] Z. Pei and C. Yu. Investigation on the dynamic behavior of the fiber in the vortex spinning nozzle and effects of some nozzle structure parameters. *Journal of Engineered Fibers and Fabrics*, 6(2):16–29, 2011.

[142] Z. Wu, S. Chen, and Y. Liu et al. Air-flow characteristics and yarn whipping during start-up stage of air-jet weft insertion. *Textile Research Journal*, 86(18): 1988–1999, 2016.

[143] Y. Jin, J. Li, and L. Zhu et al. Three-dimensional numerical simulation of the movement of the flexible body under different constraints. *Journal of Thermal Science*, 23(6):593–599, 2014.

[144] D. Baraff and A. Witkin. Large steps in cloth simulation. In *Proceedings of the 25th Annual Conference on Computer Graphics and Interactive Techniques*, SIGGRAPH '98, pages 43–54, New York, NY, USA, 1998. ACM. ISBN 0-89791-999-8.

[145] J. Degroote, S. Annerel, and J. Vierendeels. Stability analysis of gauss-siedel iterations in a partitioned simulation of fluid-structure interaction. *Computers and Structures*, 88:263–271, 2010.

[146] I. Hertens. Numerical analysis of the fluid-structure interaction in the main nozzle of an air-jet loom. Master's thesis, Ghent university, 2014.

[147] R. A. K. Sanches and H. B. Coda. On fluid–shell coupling using an arbitrary lagrangian–eulerian fluid solver coupled to a positional lagrangian shell solver. *Applied Mathematical Modelling*, 38:3401–3418, 2014.

[148] J. Donea, S. Giuliani, and J.P. Halleux. An arbitrary lagrangian-eulerian finite element method for transient dynamic fluid-structure interactions. *Computer Methods in Applied Mechanics and Engineering*, 33(1):689 – 723, 1982. ISSN 0045-7825.

[149] J. Degroote. Partitioned simulation of fluid-structure interaction. *Archives of Computational Methods in Engineering*, 20(3):185–238, 2013.

[150] J. Degroote, K-J. Bathe, and J. Vierendeels. Performance of a new partitioned procedure versus a monolithic procedure in fluid–structure interaction. *Computers and Structures*, 87(11-12):793–801, 2009.